ALLSENSORS 2024

The Ninth International Conference on Advances in Sensors, Actuators, Metering and Sensing

ISBN: 978-1-68558-164-0

May 26 - 30, 2024

Barcelona, Spain

ALLSENSORS 2024 Editors

Paulo E. Cruvinel, Embrapa Instrumentation, Brazil

Sandra Sendra Compte, Polytechnic University of Valencia, Spain

ALLSENSORS 2024

Forward

The Ninth International Conference on Advances in Sensors, Actuators, Metering, and Sensing (ALLSENSORS 2024), held between May 26th and May 30th, 2024, in Barcelona, Spain, continued a series of events covering related topics on theory, practice, and applications of sensor devices, techniques, data acquisition and processing, and on wired and wireless sensors and sensor networks.

Sensors and sensor networks have a great potential of providing diverse services to broad range of applications, not only on science and engineering, but equally importantly on issues related to critical infrastructure protection and security, healthcare, the environment, energy, food safety, and the potential impact on the quality of all areas of life.

Sensor networks and sensor-based systems support many applications today above ground. Underwater operations and applications are quite limited by comparison. Most applications refer to remotely controlled submersibles and wide-area data collection systems at a coarse granularity. Other remote sensing domains and applications are using special sensing devices and services. Transducers and actuators complement the monitoring and control and constitute an area of interest related to sensors. They make use of specific sensor-based measurements and convey appropriate control actions.

We take here the opportunity to warmly thank all the members of the ALLSENSORS 2024 technical program committee, as well as all the reviewers. The creation of such a high-quality conference program would not have been possible without their involvement. We also kindly thank all the authors who dedicated much of their time and effort to contribute to ALLSENSORS 2024. We truly believe that, thanks to all these efforts, the final conference program consisted of top-quality contributions. We also thank the members of the ALLSENSORS 2024 organizing committee for their help in handling the logistics of this event.

We hope that ALLSENSORS 2024 was a successful international forum for the exchange of ideas and results between academia and industry and for the promotion of progress in the field of sensors, actuators, metering, and sensing.

ALLSENSORS 2024 Chairs

ALLSENSORS 2024 Steering Committee
Michael Niedermayer, Berliner Hochschule für Technik, Germany
Paulo E. Cruvinel, Embrapa Instrumentation, Brazil
Matteo Tonezzer, CNR-IMEM, Trento, Italy
Sandrine Bernardini, Aix Marseille University, France
Almudena Rivadeneyra, Universidad de Granada, Spain

ALLSENSORS 2024 Publicity Chairs
Sandra Viciano Tudela, Universitat Politecnica de Valencia, Spain
Laura Garcia, Universidad Politécnica de Cartagena, Spain

ALLSENSORS 2024
Committee

ALLSENSORS 2024 Steering Committee

Michael Niedermayer, Berliner Hochschule für Technik, Germany
Paulo E. Cruvinel, Embrapa Instrumentation, Brazil
Matteo Tonezzer, CNR-IMEM, Trento, Italy
Sandrine Bernardini, Aix Marseille University, France
Almudena Rivadeneyra, Universidad de Granada, Spain

ALLSENSORS 2024 Publicity Chairs

Sandra Viciano Tudela, Universitat Politecnica de Valencia, Spain
Laura Garcia, Universidad Politécnica de Cartagena, Spain

ALLSENSORS 2024 Technical Program Committee

Francesco Aggogeri, University of Brescia, Italy
Otman Aghzout, National School of Applied Sciences of Tetouan, Morocco
Amin Al-Habaibeh, Nottingham Trent University, UK
Youssef N. Altherwy, Imperial College London, UK
Darius Andriukaitis, Kaunas University of Technology, Lithuania
Federico Aromolo, Scuola Superiore Sant'Anna, Pisa, Italy
Piotr Artiemjew, University of Warmia and Mazury, Poland
Farzad Asgarian, University of Michigan, Ann Arbor, USA
Herve Aubert, Laboratory for Analysis and Architecture of Systems (LAAS-CNRS), France
Yang Bai, University of Maryland College Park, USA
Roberto Beghi, Università degli Studi di Milano, Italy
Artur Bejger, Maritime University of Szczecin, Poland
Roc Berenguer Pérez, TECNUN - Technological Campus of the University of Navarra, Spain
Sandrine Bernardini, Aix Marseille University, France
Mourad Bezzeghoud, University of Évora, Portugal
Xavier Boddaert, Mines Saint Etienne | Centre Microélectronique de Provence (CMP), France
Muhammad Ali Butt, Warsaw University of Technology, Poland
Maria Candelaria Hernandez Goya, Universidad de La Laguna, Spain
Juan Vicente Capella Hernández, Universitat Politècnica de València, Spain
Vítor Carvalho, 2AI-EST-IPCA / Algoritmi Research Centre - UM, Portugal
Paula María Castro Castro, Universidade da Coruña, Spain
Rosario Catelli, Institute for High Performance Computing and Networking (ICAR) - National Research Council (CNR), Italy
Debashish Chakravarty, IIT Khaargpur, India
Yueqiang Cheng, NIO, USA
Nan-Fu Chiu, National Taiwan Normal University,Taiwan
Susana Costa, University of Minho, Portugal
Paulo E. Cruvinel, Embrapa Instrumentation, Brazil
Luca Davoli, University of Parma, Italy

Udhaya Kumar Dayalan, Trane Technologies, USA
Marcos Antonio de Oliveira Junior, Federal University of Pelotas, Brazil
Francesco G. Della Corte, University of Napoli Federico II, Italy
Emiliano Descrovi, Polytechnic University of Turin, Italy
Chérif Diallo, Université Gaston Berger (UGB), Senegal
Toan Dinh, University of Southern Queensland, Australia
Yvan Duroc, University Claude Bernard Lyon 1, France
Raafat Elfouly, Rhode Island College, USA
Abdelali Elmoufidi, Sultan Moulay Slimane University, Morocco
Ahmed Fakhfakh, Digital Reasearch Center of Sfax, Tunisia
Olga A. Fedorova, A. N. Nesmeyanov Institute of Organoelement Compounds, Moscow, Russia
Attilio Frangi, Politecnico di Milano, Italy
Orlando Frazão, INESC TEC, Porto, Portugal
Kelum Gamage, University of Glasgow, UK
Ivan Ganchev, University of Limerick, Ireland / University of Plovdiv / IMI-BAS, Bulgaria
Jiechao Gao, University of Virginia, USA
Félix J. García Clemente, University of Murcia, Spain
Pietro Garofalo, Turingsense EU LAB s.r.l., Italy
Dominik Roy George, Eindhoven University of Technology, The Netherlands
Mojtaba Ghodsi, University of Portsmouth, UK
Patrick Goh, Universiti Sains Malaysia, Malaysia
Sanaz Haddadian, Heinz Nixdorf Institute | University of Paderborn, Germany
Kuan He, Apple Inc., USA
Daniel Hill, Aston University, UK
Carmen Horrillo-Güemes, Grupo de Tecnología de Sensores Avanzados (SENSAVAN) | ITEFI-CSIC, Madrid, Spain
Pengpeng Hu, Vrije Universiteit Brussel, Belgium
Rui Igreja, Universidade NOVA de Lisboa, Portugal
Dimosthenis Ioannidis, CERTH/ITI, Thessaloniki, Greece
Ahmed Abu Ismaiel, Municipality of Abasan Al-Kabira, Gaza, Palestine
Nikos Kalatzis, Neuropublic S.A. / National Technical University of Athens, Greece
Grigoris Kaltsas, University of West Attica, Greece
Liuwang Kang, University of Virginia, USA
M-Tahar Kechadi, University College Dublin (UCD), Ireland
Anwesha Khasnobish, TCS Research, Kolkata, India
Jan Kubicek, VSB - Technical University of Ostrava, Czech Republic
Kai Lin, eBay Inc., USA
Paula Louro, ISEL/IPL & CTS/UNINOVA, Portugal
Vladimir Lukin, National Aerospace University, Kharkov, Ukraine
Dandan Ma, Northwestern Polytechnical University, China
Wei Ma, The Hong Kong Polytechnic University, Hong Kong
Stephane Maag, Télécom SudParis, France
Adnan Mahmood, Macquarie University, Australia
Marco Manso, PARTICLE Summary, Portugal
Jan Mareš, University of Chemistry and Technology, Prague, Czech Republic
Vincenzo Marletta, ST Microelectronics - Catania site, Italy
Nader Mbarek, University of Bourgogne Franche-Comté, France
Javier Medina Quero, University of Jaén, Spain

Massimo Merenda, CNIT - Consorzio Nazionale Interuniversitario per le Telecomunicazioni / University Mediterranea of Reggio Calabria, Italy
Lyudmila Mihaylova, University of Sheffield, UK
Carolina Miozzi, University of Rome Tor Vergata / RADIO6ENSE srl, Italy
Igor Nazareno Soares, University of São Paulo, Brazil
Michael Niedermayer, Berliner Hochschule für Technik (BHT), Germany
Marek R. Ogiela, AGH University of Science and Technology, Krakow, Poland
Anna Ostaszewska-Liżewska, Warsaw University of Technology, Poland
Mehmet Akif Özdemir, Izmir Katip Celebi University, Turkey
Lorenzo Palazzetti, University of Perugia, Italy
Udayan Sunil Patankar, TalTech University of Technology, Tallinn, Estonia
D. R. Patil, Rani Laxmibai Mahavidyalaya Parola | North Maharashtra University, Jalgaon, India
Pablo Pérez García, Instituto de Microelectrónica de Sevilla, Spain
Vengadesh Periasamy, Low Dimensional Materials Research Centre (LDMRC) | Institute of Ocean, Earth and Sciences (IOES) | University of Malaya, Malaysia
Patrick Pons, CNRS-LAAS, Toulouse, France
Rüdiger Pryss, University of Würzburg, Germany
Parvaneh Rahimi, Institute of Electronic - and Sensor Materials | TU Bergakademie Freiberg, Germany
Càndid Reig, University of Valencia, Spain
Almudena Rivadeneyra, University of Granada, Spain
David Rivas-Lalaleo, Universidad de las Fuerzas Armadas ESPE, Ecuador
Alexandra Rivero García, Universidad de La Laguna, Spain
Christos Riziotis, National Hellenic Research Foundation, Greece
Bahram Djafari Rouhani, Université de Lille Sciences et Technologies, France
Gonzalo Sad, CIFASIS / CONICET / FCEIA | Universidad Nacional de Rosario, Argentina
Markus Santoso, University of Florida, USA
Iván Santos González, Universidad de La Laguna, Spain
Jagannathan Sarangapani, Missouri University of Science and Technology, USA
Sudipta Saha Shubha, University of Virginia, USA
Bruno M. C. Silva, University of Beira Interior, Portugal
Jan Steckel, Universiteit Antwerpen, Belgium
Mu-Chun Su, National Central University, Taiwan
Nur Syazreen Ahmad, Universiti Sains Malaysia (USM), Malaysia
Roman Szewczyk, Warsaw University of Technology, Poland
Alessandro Tognetti, University of Pisa, Italy
Matteo Tonezzer, CNR-IMEM, Trento, Italy
Anish Chand Turlapaty, Indian Institute of Information Technology Sri City, Chittoor, India
Sumarga K. Sah Tyagi, University of South Florida, USA
Sathishkumar V E, Sunway University, Malaysia
Harsh Vardhan, Vanderbilt University, USA
Diego Vergara, Universidad Católica Santa Teresa De Jesús De Ávila, Spain
Sudip Vhaduri, Fordham University, USA
Manuel Vieira, CTS-ISEL, Portugal
Manuela Vieira, ISEL-IPL/CTS-UNINOVA, Portugal
Stefanos Vrochidis, Information Technologies Institute - CERTH, Greece
Guang Wang, Rutgers University, USA
Xianpeng Wang, Hainan University, China
Ulf Witkowski, South Westphalia University of Applied Sciences, Germany

Copyright Information

For your reference, this is the text governing the copyright release for material published by IARIA.

The copyright release is a transfer of publication rights, which allows IARIA and its partners to drive the dissemination of the published material. This allows IARIA to give articles increased visibility via distribution, inclusion in libraries, and arrangements for submission to indexes.

I, the undersigned, declare that the article is original, and that I represent the authors of this article in the copyright release matters. If this work has been done as work-for-hire, I have obtained all necessary clearances to execute a copyright release. I hereby irrevocably transfer exclusive copyright for this material to IARIA. I give IARIA permission or reproduce the work in any media format such as, but not limited to, print, digital, or electronic. I give IARIA permission to distribute the materials without restriction to any institutions or individuals. I give IARIA permission to submit the work for inclusion in article repositories as IARIA sees fit.

I, the undersigned, declare that to the best of my knowledge, the article is does not contain libelous or otherwise unlawful contents or invading the right of privacy or infringing on a proprietary right.

Following the copyright release, any circulated version of the article must bear the copyright notice and any header and footer information that IARIA applies to the published article.

IARIA grants royalty-free permission to the authors to disseminate the work, under the above provisions, for any academic, commercial, or industrial use. IARIA grants royalty-free permission to any individuals or institutions to make the article available electronically, online, or in print.

IARIA acknowledges that rights to any algorithm, process, procedure, apparatus, or articles of manufacture remain with the authors and their employers.

I, the undersigned, understand that IARIA will not be liable, in contract, tort (including, without limitation, negligence), pre-contract or other representations (other than fraudulent misrepresentations) or otherwise in connection with the publication of my work.

Exception to the above is made for work-for-hire performed while employed by the government. In that case, copyright to the material remains with the said government. The rightful owners (authors and government entity) grant unlimited and unrestricted permission to IARIA, IARIA's contractors, and IARIA's partners to further distribute the work.

Table of Contents

Using Light-Band Sensors for Stress Evaluation in Rainfed Maize Agricultural Crop

Paulo E. Cruvinel, Wilbur N. Chiuyari Veramendi
Embrapa Instrumentation, São Carlos, SP, Brazil
Post-Graduation Program in Computer Science - Federal University of São Carlos, SP, Brazil
Email: paulo.cruvinel@embrapa.br, wilbur.chiuyari@estudante.ufscar.br

***Abstract*- Sensors have become essential in farming. They have been allowing to climatically monitor not only plants, but also soil, in order to support decision making to greater yields, as well as allowing rational use of inputs. Based on sensors, it is possible to develop efficient tools for the dynamics evaluating of crops directly in situ, including real-time analyzes. In this study, based on the use of sensors for red and the near-infrared lights spectra, the stress of rainfed maize crop was evaluated as a function of both Nitrogen dose and water availability. In fact, for validation, a true crop dynamics stress was evaluated using the normalized difference vegetation index weighted by the value of the near infrared reflectance for each specific region of the agricultural field. Results have shown its relationship with both plant water and Nitrogen availability. Furthermore, positive correlation with the plant stress and the modified vegetation index has been found, i.e., leading to an adequate indicator for plant stress and yield evaluation.**

Keywords—light-band sensor; crop stress; agricultural sensor; intelligent instrumentation; yield analysis.

I. INTRODUCTION

Currently, agricultural farms make use of advanced sciences and technologies, which include orbital monitoring for land occupation planning, agricultural soil quality care, assessment of plant vigor in cultivation areas, intelligent climate monitoring, as well as safety of the rural properties.

Precision Agriculture, for example, is based on the observation, monitoring and management of all inputs, necessary to obtain an adequate relationship between costs and benefits [1]. The new technologies used in this segment came to meet demands and achieve favorable results, that is, productivity gains and building resilience in the agroecosystems, in order to reach sustainability. The breakthrough to such a new agricultural paradigm has occurred with the introduction of the Global Positioning System (GPS), which enabled the entry of other technologies such as the use of new machines guided by computers and satellites.

GPS-guided tractors for planting seeds, applying pesticides, and especially for harvesting, have been enabling performance gains and reduced downtime. The use of integrated systems was another major innovation in recent years. The possibility of accessing soil, plant and climate data in real time has brought new opportunities for improving practically all the processes involved in food, fiber and energy from biomass production. The use of technologies has been making it possible to use the minimum quantity required in each specific area, as well as, when necessary, treating each plant in a unique and differentiated way. All these innovations used in the sector make use of sensors. In fact, sensor technology involves measuring, quantifying and transmitting signals used in decision support systems [2]. In modern agricultural automation systems, sensors are present [3]. Likewise, the Internet of Things (IoT) technologies are also present and have contributed to expand the scale related to the use of sensors in agriculture, as well as occurred in industry [4].

In fact, in agriculture, there are a series of systems that involve automation, which combine different sensors, control systems and actuators to operate equipment such as spraying machines for pest control, planters, and harvesters, among others. This level of automation makes it possible to increase efficiency, to improve consistency, to increase quality, to bring gains in effectiveness and to reduce human errors [5].

Furthermore, such a context it is often associated with an increase in productivity, and consequently production rate.

Additionally, with the advancement of sensor-based technologies, embedded automation also helps to optimize the use of the agricultural inputs, as well as to minimize losses in agricultural production. In fact, there are known relations in between crop stress and the presence of both biotic and abiotic factors, like those caused respectively by the presence of pests and due the absence of water, which affects healthy crop growth [6]-[9].

Sensors help to understand the relationship between climate and agriculture within a production process in a farming area, which is fundamental for food production.

Agriculture is an essential activity for the economy of many countries. The climate and the inputs, like nutrients, are the most important factors that affect agricultural production. In this sense, climate variations, such as rainfall and temperature, and nutrients availability should be carefully observed during the crop`s management process.

Historical records, current readings and forecasts can assist the agricultural management process considering statistics and data collected directly in the field.

The monitoring with sensors that operate in the Red (RED) and Near Infra-Red (NIR) light-bands have been promising for crop monitoring, and by using these bands it is possible to calculate the Normalized Difference Vegetation Index (NDVI). This index was established in 1974 [10] and later validated in 1979 [11] through linear combinations of the RED and NIR bands to monitor biomass density.

ISBN: 978-1-68558-164-0

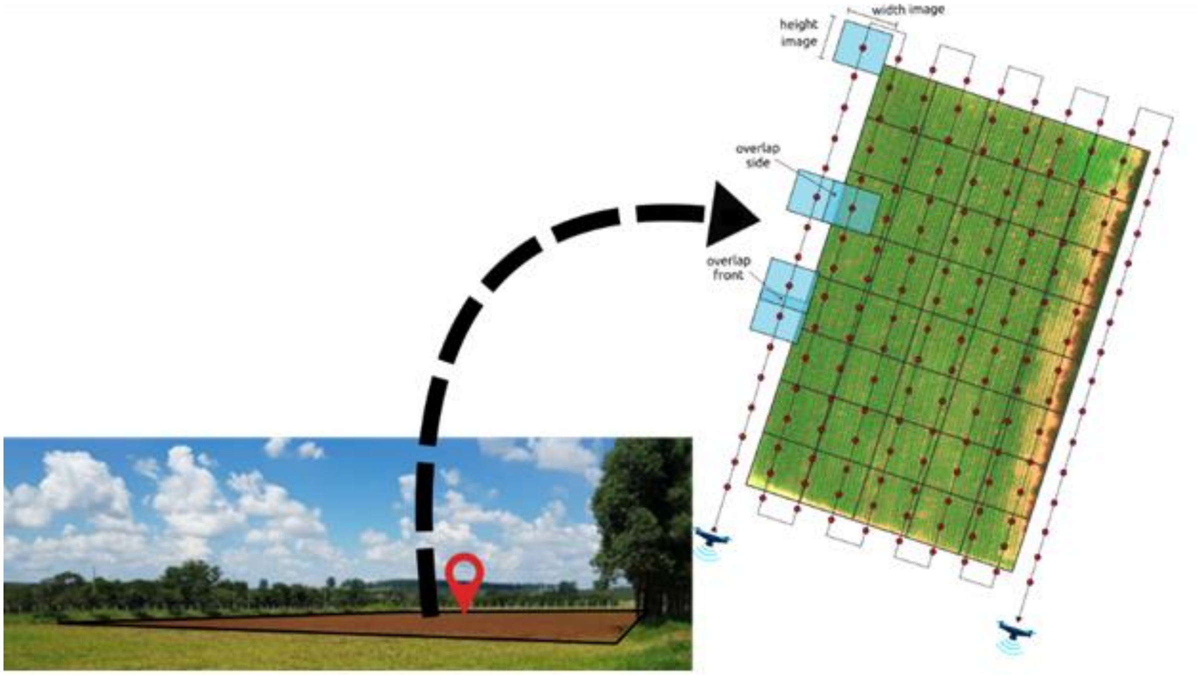

Figure 1. Experimental agricultural field`s view, having a grid for site-specific management.

NDVI has values between -1.0 and 1.0 and, in such a context, values between -1.0 and 0.0 correspond to non-plant surfaces that have RED reflectance greater than NIR. The soil has an NDVI value close to zero. With substantial reflectance in the NIR, plants have an NDVI value between 0.1 and 1.0, the higher the value, the greater the plant density. Also, the healthiest plants correspondent to a value equal to 1.0 and the least healthy plants to a value of 0.0. In fact, as a structural index, it is widely used for agricultural monitoring as it has a strong linear correlation with crop growth. However, NDVI has several limitations and challenges that need to be considered, such as sensitivity to external factors, variability among crops and cultivars, need for calibration and validation.

In addition, calibration and validation should be done using ground truth data and complementary indicators such as crop productivity.

This work presents a study to minimize the limitations when using the NDVI to evaluate stress regions in tropical agricultural crops due to lack of water and nutrients based on image sensors that respond to RED (668 nm ±10 nm) and NIR (840 nm±40 nm) wavelengths to aid the agricultural management process.

After this introduction in Section I, this paper is structured as follows. Section II presents the materials and methods, including the agricultural experiments for validation and the sensor`s system description, as well as the embedded board specifications. Section III presents the results of the validation of the use of the RED and NIR sensors and the evaluation of stress into a productive rainfed maize crop. The final conclusions are presented in Section IV.

II. MATERIAL AND METHODS

Figure 1 shows the experimental agricultural area that has been used for validation, i.e., following the study standards of Embrapa Instrumentation. It is located 860 m from the geographic coordinates: 21°57’3.9” S and 47°51’10.9” W at the National Reference Laboratory for Precision Agriculture (LANAPRE) in São Carlos, SP, Brazil.

The experiment for the evaluation of the crop stress was organized in an agricultural area with maize (*Zea mays L.*), having 4000 m^2, and sampling grid equal to 10 m × 10 m [12]. Also, Figure 1 shows such an arrangement for specific management, i.e., divided into 40 blocks (from B1 to B40).

An important point to be noted is that the respective area was divided into four plots of 1000 m^2 (20 m × 50 m) aiming to manage Nitrogen with surface and broadcast fertilization, thus being associated with fertilization of soil that was initially carried out before planting in the experimental agricultural area.

Soil chemical analyzes were carried out from composite samples collected in horizon A (root zone) at specific sites on the sampling grid. Soil fertilization occurred once and scaled applications of Nitrogen (top-dressing fertilization) were also considered, i.e., using the 0, 18, 36 and 72 kg/ha, respectively 0%, 50%, 100%, and 200% in relation to agronomic recommended dose [13].

Figure 2 illustrates the electromagnetic spectrum for the frequency`s bands that have been used in this work. In the light spectrum, it has been considered a Region Of Interest (ROI) comprised by the visible and near infrared spectra.

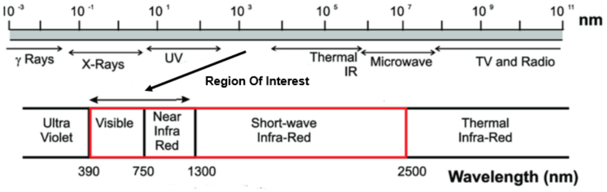

Figure 2. Electromagnetic spectrum and the ROI related to the visible and infrared bands.

In addition, eight flight missions were considered, all of them based on the use of a multirotor Unmanned Aircraft System (UAS), DJI Matrice 100 (Figure 3).

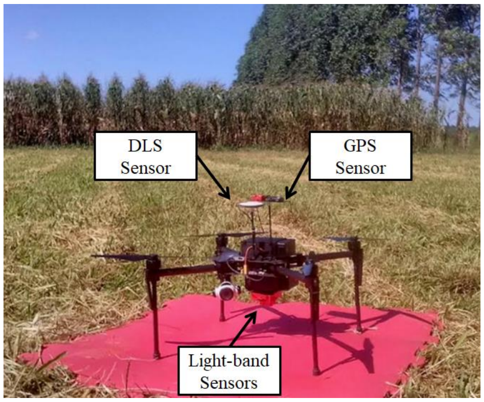

Figure 3. The UAS and hardware setup for the RGB, RED, and NIR images acquisition.

For imaging, a Micasense RedEdge-M multispectral camera was embedded, and provided onboard. The specifications of the sensors located at the Micasense camera are detailed in Table I [14].

TABLE I. TECHNICAL SPECIFICATIONS FOR MICASENCE REDEDGE-M

Parameters	Specifications
Weigth	170 g (Including DLS)
Dimensions	9.4 cm × 6.3 cm × 4.6 cm (3.7" × 2.5" × 1.8")
External Power	4.2V−15.8V, 4W nominal, 8W peak
Spectral Bands	Narrowband: Blue, Green, Red, Near-IR
Capture Rate	1 capture per second (per band), 12−bit RAW
Ground Sample Distance (GSD)	5.95 cm/pixel (per band)
Wavelength	Blue (475 nm center ± 20 nm) Green (560 nm ± 20 nm) Red (668 nm center ± 10 nm) Near-IR (840 nm ± 40 nm)

The flights missions were carried out considering the timeline related to the phenomenological state of the maize culture [15]. For the RED, GREEN, BLUE, and NIR measurements, the acquisition process used the Ground Control Points (GCP). They were collected by high-precision GPS in conjunction with a Real-Time Kinematic (RTK) receiver that recorded their geographic coordinates to an accuracy of ± 1 cm. In this way, the GCPs were used as input to control the flight missions. Additionally, the imaging equipment includes to a Downwelling Light Sensor (DLS) for measuring the influences of the sun's brightness, or changes in contrast due to superimposition of clouds in the sky, thus providing the capacity to correct global changes in light.

Aerial mapping reproduces the phenomenon of stereoscopic vision, following a flight pattern of parallel lines, along specified routes with waypoints. Likewise, in accordance with the UAS settings and the onboard light-bands sensors, eight flights were conducted within a time interval from 11 A.M. to 12 A.M., i.e., during the morning periods.

Besides, to perform the analysis of stress into the crop having maize plants, an extraction of information from each site-specific or block has been considered. In fact, for each block has been considered a ROI and collected data from the multispectral light-bands. In addition, the collected images have been filtering by means of a Gaussian filter (Equation 1). Likewise, for each ROI the rotation angle has been found by calculation, using Equation 2.

$$G_{\sigma}(x,y) = \frac{1}{2\pi\sigma^2} e^{-\frac{x^2+y^2}{2\sigma^2}} \tag{1}$$

where the Gaussian function G_{σ} (x, y) is controlled by the variance σ^2, and mean equal to zero.

$$Rotation = \begin{bmatrix} 1 & 0 & t_x \\ 0 & 1 & t_y \\ 0 & 0 & 1 \end{bmatrix} \begin{bmatrix} \cos\theta & -\sin\theta & 0 \\ \sin\theta & \cos\theta & 0 \\ 0 & 0 & 1 \end{bmatrix} \begin{bmatrix} 1 & 0 & -t_x \\ 0 & 1 & -t_y \\ 0 & 0 & 1 \end{bmatrix} \tag{2}$$

where $-t_x$, and $-t_y$ correspond to the translation of the ROI to the origin, whereas t_x, and t_y shift it back to its original position.

Furthermore, for the NDVI index (Equation 3), it has been considered adjustments based on the reuse of the NIR light-band, i.e., in order to allow information beyond the biomass evaluation and plant growth only. Such an arrangement has been considered in order to figure out plant`s stress due external abiotic factors like water and nutrients availability in the crop area (Equation 4).

$$NDVI = \left(\frac{NIR-RED}{NIR+RED}\right) \tag{3}$$

$$\widehat{NDVI} = \left(\frac{NIR-RED}{NIR+RED}\right)\overline{NIR} \tag{4}$$

where $\overline{NIR}$ correspond to the mean value of the NIR pixels values for each site-specific. The $\widehat{NDVI}$ represents the modified NDVI value, that means, taking emphasis on the plant stress into a specific crop region.

For data analysis it has been used descriptive statistics method, i.e., a boxplot, which is a type of chart often used in explanatory data analysis. Box plots visually show the distribution of numerical data and skewness by displaying the data quartiles (or percentiles) and averages. Also, it

ISBN: 978-1-68558-164-0

shows the five-number summary of a set of data: including the minimum score, first (lower) quartile, median, third (upper) quartile, and maximum score [16].

III. RESULTS AND DISCUSSION

For multispectral image acquisition, it was necessary to perform radiometric calibration to convert the metadata of the digital image to a physical scale. On the other hand, the geometry of the aerial image was established by the size of the sensor, the focal length, and height of the UAS flight, which together determine its Ground Sample Distance (GSD) (Table II). The GSD provides the corresponding measure for the pixels of the surface of the experimental area or the area covered by the image. It was necessary to establish the percentages of lateral and frontal overlapping of the aerial images, which were equal to 80% respectively.

The number of registered images for all the realized flight was equal to 300 for each spectral band, i.e., leading to a total amount of 9600 images. In such a context, the total required storage capacity was equal to 29.52 GB (gigabyte), because the surface width and height were equal to 27 m × 20 m respectively, and the distances between each front and side capture were 4 m and 5 m, respectively.

TABLE II. PARAMETERS USED FOR DATA ACQUISITION

Description	Values	Units
Flying altitude	138	m
Mission flying time	12	min
Max. speed of flying	11	m/s
Front and side overlap	80	%
Ground sample distance	5.95	cm/pixel

Figure 4 shows examples of results obtained from the second and eighth flights respectively, i.e., considering the rotation of the images and Regions Of Interest (ROI) for analysis of block 25, in terms of the RGB and NIR light-bands.

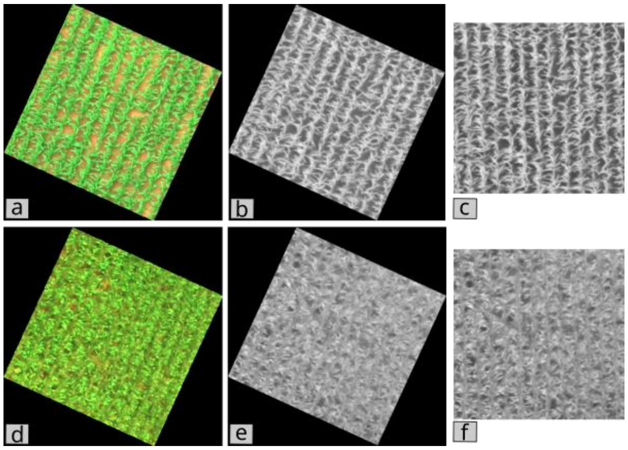

Figure 4. Sample of analysis for the block 25: from the second flight - (a) RGB, (b) NIR, and (c) ROI NIR; from the eighth flight - (d) RGB, (e) NIR and (f) ROI NIR.

Statistical analyzes for collected data were carried out for the eight flights, that is, considering the reflectance measurements for each site-specific in the culture area, i.e., based on both the RED and the NIR light-bands of the electromagnetic spectrum.

Thus, considering as an example of the obtained results, one may observe the carried-out data analysis for the eighth flight (Figure 5 and Figure 6).

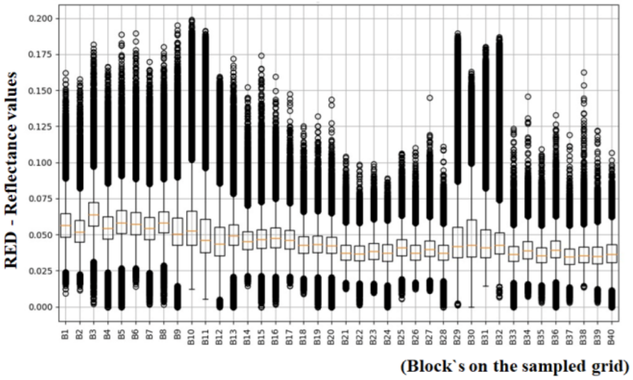

Figure 5. Statistical evaluation for the RED light-band reflectance in the specific-sites of the maize crop area, that means, considering all the experimental regions (from B1 to B40).

Such results were obtained by scanning with the RED and NIR sensors the 40 sites-specific of the maize production areas. In fact, such a UAS flight was programmed to occur during the phenological reproductive stage of the maize in the crop area, when the corn’s seeds are being structured on the cobs to reach the known physiological maturity stage.

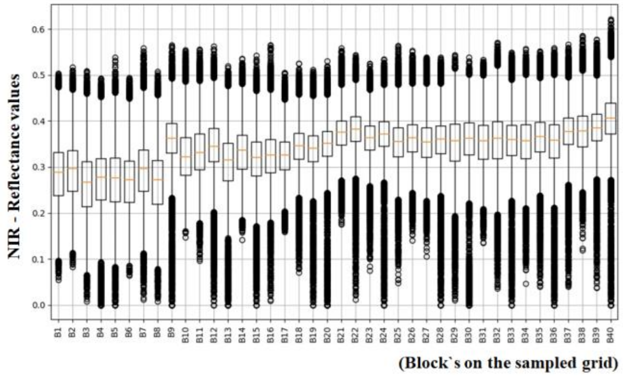

Figure 6. Statistical evaluation for the NIR light-band reflectance in the specific-sites of the maize crop area, that means, considering all the experimental regions (from B1 to B40).

The stress evaluation in this phase of the maize production is essential since water and nutrients play a very important role. How much higher the plant stress in the crop sites-specific smaller will become the productivity, i.e., loss in maize production is increased. Furthermore, we observed that for the RED light-band the median values for the reflectance were between the 3.7 % and 6.3 %, while for NIR the median values were between 26.8 % and 40.9 %.

ISBN: 978-1-68558-164-0

The lowest reflectance values indicate higher absorbance values for the RED light-band, which were produced by pigments present in corn leaves, while in the NIR light-band reflectance's resulted from the interaction of radiation with the superficial cellular structure of the maize leaves. In this context, it was possible to observe that the increase in reflectance in the NIR light-band was related to the physiological aspects of the leaf and varied with its water content in the cellular structure and the Nitrogen availability, thus being useful for characterizing the level of crop stress in all analyzed regions.

In addition, the NDVI values were calculated using Equation 3, as well as statistically evaluated (Figure 7).

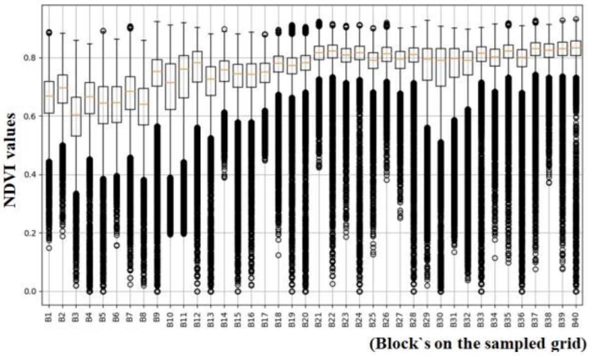

Figure 7. Statistical evaluation for the NDVI for all sites-specific of the maize crop area, that means, considering the experimental regions (from B1 to B40).

The yield (in kg) for the 40 specific sites were also evaluated. In such a result, it was possible to verify a great spatial variability in productivity.

In fact, as mentioned previously, while the NDVI can give information about the biomass density and crop growth, something else should be understand in relation to productivity. In fact, NDVI doesn't have a good sensitivity to external factors, like agricultural inputs. In fact, once soil fertilization with the application of scaled Nitrogen contents were considered for the rainfed maize crop area, it has become possible to evaluate its contribution in the crop stress.

The blocks B1 to B10, B11 to B20, B21 to B30, and B31 to B40 were evaluated in relation to Nitrogen`s application, following the percentage concentration equal to 0%, 50%, 100%, and 200% respectively. Likewise, it was possible to observe the yield values and their increments.

Then, to get such a better understanding it was considered Equation 4, to evaluate the variability occurrence due to agricultural inputs externalities, i.e., the stress response to both Nitrogen and the water from natural rains based on the correlation between productivity and the modified index.

Figure 8 shows the resultant statistical analysis for all sites-specific of the experimental maize crop area.

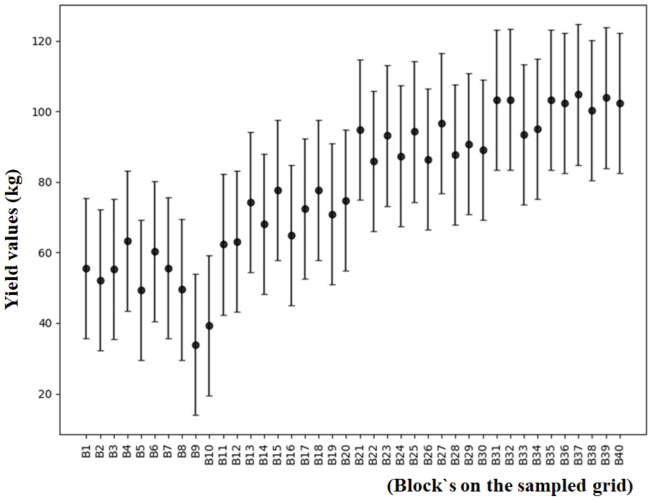

Figure 8. Productivity for each specific site from the maize crop area that means, considering the experimental regions (from B1 to B40).

In addition, based on such an analysis, it was possible to evaluate the yield variability in relation to the crop stress mainly as a function of the Nitrogen availability in each site-specific (Figure 9).

In such an analysis, since the linear correlation coefficient of determination was equal to 0.78 (Figure 10), it was possible to confirm the usefulness of the modified index to evaluate the yield dependency in relation to the crop stress.

Likewise, these results have illustrated that RED and NIR sensors-based imagery can provide information on the plants stress. Spectral measurements also reflect changes in nutritional deficiency in plants. In addition, with the advent of precision farming, there has been an interest not only in large-scale but also in small-scale application of light-band sensors for imagery acquired through UAS technologies.

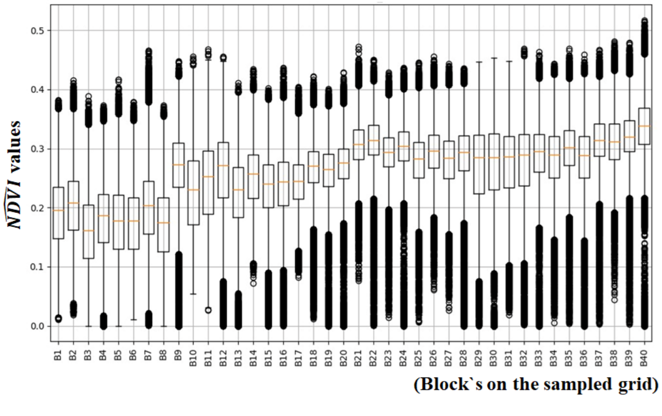

Figure 9. Statistical evaluation for the $\widehat{NDVI}$, i.e., considering all specific sites of the experimental maize crop area.

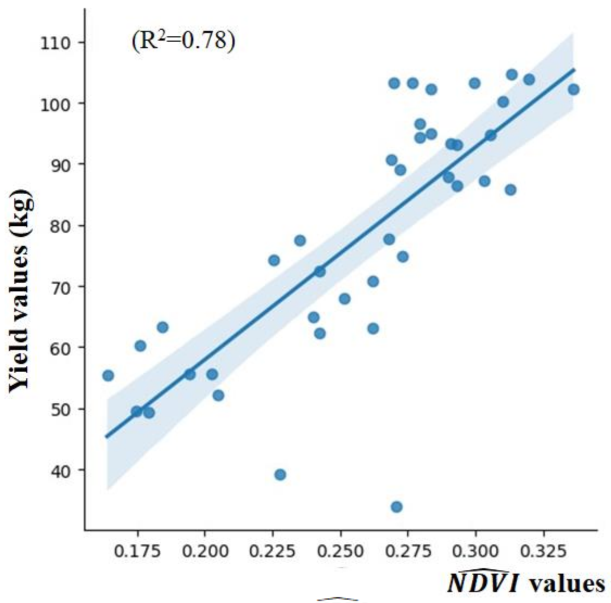

Figure 10. Correlation analysis ($\widehat{NDVI}$ and Yield), considering all sites-specific of the experimental rainfed maize crop area.

Moreover, Carbon and Hydrogen (C-H), Oxygen and Hydrogen (O-H), and Nitrogen and Hydrogen (N-H) absorbtion wavelengths fall in the NIR spectrum. NIR is suitable for use in agriculture mainly because in the living plants the organic compounds are the major components.

IV. CONCLUSION

The ability of $\widehat{NDVI}$ to evaluate crop stress based on physical and chemical externalities was studied through measurements and imaging at various phenological stages in an experimental agriculture rainfed maize crop. Besides, the information on the deficiency or excess of Nitrogen, one of the major plant nutrients, by detecting plant stress was useful to established alerts on crop production. In fact, the signature related to plants led to a new sensor-based index to support decision making related to crop stress and its relation to productivity improvement, which is an original contribution. If an analysis shows a deficiency of Nitrogen, a manager can provide timely nutritional supplements, i.e., by aggregating values in sustainability of the crop area, avoiding over-use of fertilizers, decreasing the resulting toxicity in plants, as well as decreasing the costs. Future research works will consider the development of customized agricultural sensors for smart and real-time crop stress evaluation.

ACKNOWLEDGMENT

This research was partially supported by both the São Paulo Research Foundation, Brazil (FAPESP, Process No. 17/19350-2), and the Brazilian Corporation for Agricultural Research (Embrapa).

REFERENCES

[1] S. Sharma and S. Angidi, “Precision agriculture and its future”, International Journal of Plant & Soil Science, vol. 34, issue 24, pp. 200-204, 2022.

[2] M. Yuriyama, T. Kushida, and M. Itakura, "A new model of accelerating service innovation with sensor-cloud infrastructure". In: Proceedings of the Annual SRII Global Conference, San Jose, CA, USA, pp. 308-314, 2011.

[3] A. V. Mamishev, K. Sundara-Rajan, F. Yang, Y. Du and M. Zahn, "Interdigital sensors and transducers". In: Proceedings of the IEEE, vol. 92, n. 5, pp. 808-845, 2004.

[4] S. Liberata and G. R. Sinha, “Advances in smart environment monitoring systems using IoT and sensors, Sensors, vol. 20, n. 11, pp. 3113-3130, 2020.

[5] A. Pathak et al., “IoT based smart system to support agricultural parameters: a case study”, Procedia Computer Science, vol. 155, pp. 648–653, 2019.

[6] A. Nayyar and V. Puri, “Smart farming: Iot based smart sensors agriculture stick for live temperature and moisture monitoring using Arduino, cloud computing & solar technology”. In: Proceedings of the International Conference on Communication and Computing Systems (ICCCS), Gurgaon, India, pp. 673–680, 2016.

[7] M. P. P. Kulkarni, “IoT based smart agricultural system. International Journal for Research in Applied Science and Engineering Technology, vol. 7, pp. 2037–2041, 2019.

[8] M. A. Al Mamun and M. R. Yuce, “sensors and systems for wearable environmental monitoring toward IoT-enabled applications: a review”, IEEE Sensors Journal, vol. 19, pp. 7771–7788, 2019.

[9] W. N. C. Veramendi and P. E. Cruvinel, “Method for maize plants counting and crop evaluation based on multispectral images analysis”, Computers and Electronics in Agriculture, vol. 216, pp. 108470-108482, 2024.

[10] J. W. Rouse et al., “Monitoring vegetation systems in the great plains with ERTS”. In: Proceedings of the Third Earth Resources Technology Satellite-1 Symposium, National Aeronautics and Space Administration (NASA), SP-351, Washington DC, USA, pp. 309-317, 1974.

[11] C. J. Tucker, “Red and photographic infrared linear combinations for monitoring vegetation”, Remote Sensing of Environment, vol. 8, pp. 127-150, 1979.

[12] M. W. L. Carvalho et al., “Productive performance of maize crop irrigated with and without water deficit in different plant arrangements”, Brazilian Journal of Maize and Sorghum, vol. 19, pp. 1196-11208, 2020.

[13] A. P. Duarte, H. Cantarella, and J. A. Quaggio, "3.5. Maize (Zea mays)". In: Fertilization and liming recommendations for the state of São Paulo - Bulletin 100 (Organizers: H. Cantarella, J.A. Quaggio, Jr. D. Mattos R. M. Boaretto, B. van Raij), 3 edition, Instituto Agronomic de Campinas, vol . 1, pp. 199-200, 2022.

[14] MicaSense RedEdge-M™, Multispectral Camera, User Manual, vol. 1, pp. 1-47, 2017.

[15] A. Rauf, C. Hanum, and E. N. Akop, "High growth and diameter of the stem of corn plants (Zea May, S) with a different cropping pattern". In: Proceedings of MICoMS, Emerald Publishing Limited, Leeds, vol. 1, pp. 99-106, 2017.

[16] J. W. Tukey, “Mathematics and the picturing of data”. In: Proceedings of the International Congress of Mathematicians, vol. 2, pp. 523–531, 1975.

Dimensionality Reduction for CCD Sensor-Based Image to Control Fall Armyworm in Agriculture

Alex B. Bertolla[1,2], Paulo E. Cruvinel[1,2]
[1]Embrapa Instrumentation, São Carlos, SP, Brazil
[2]Post-Graduation Program in Computer Science - Federal University of São Carlos, SP, Brazil
E-mail: alex.bertolla@embrapa.br, paulo.cruvinel@embrapa.br

***Abstract*—Digital imaging sensors, such as Charge-Coupled Devices, have been used for large-scale agricultural pest control. The ability to process and analyze the amount of data generated by these sensors has become a challenge, especially due to the high dimensionality of the collected features. In the literature, it is possible to find various research on dimensionality reduction and algorithms. This article presents a study on the dimensionality reduction of features from a digital image acquired with a Charge-Coupled Devices sensor in an agricultural field, in order to choose the optimal number of principal components for reducing feature dimensionality. In this context, it has become very important to define a method for selecting the optimal number of principal components for dimensionality reduction, while retaining only the necessary information associated with the main variables that describe the object of interest (Fall armyworms - *Spodoptera frugiperda*). The results showed, for example, that by using Hu invariant moments for feature extraction, dimensionality reduction was possible for all analyzed cases, leading to 80% of the original data. In this context, it was possible to preserve the semantic characteristics collected by the sensor and prepare them for classification.**

***Keywords*—CCD sensor, digital image, feature extraction, dimensionality reduction, principal component analysis.**

I. INTRODUCTION

Charge-Coupled-Devices (CCD) are the most used imaging sensors for digital image acquisition. They have built-in frame capture systems and the analog-to-digital conversion is done in the sensor itself [1].

CCD's sensors have been used in such ways to acquire images for different purposes. In agriculture, those sensors are usually used to capture images of pests and diseases [2], [3].

Due to the complex and high dimensions of the data captured by those sensors, storing and processing the amount of data acquired has become a challenging task [4], known as the curse of dimensionality [5]. This phenomenon is related to the fact, that with a certain degree of accuracy from a function estimation, the number of variables increases as the number of samples also has to increase [6].

To solve the issue of the curse of dimensionality, different methods based on dimensionality reduction techniques have been proposed [7]. These methods transform the original high-dimensional data into a new reduced dataset, removing the redundant and non-relevant features [8]. Dimensionality reduction algorithms allow an efficient reduction of the number of variables, and if applied before machine learning models can avoid overfiting.

In the literature, it is possible to find diverse research available about dimensionality reduction techniques for different types of data, such as Principal Component Analysis (PCA) introduced in 1901 by Karl Pearson [9], and its variations [10], Linear Discriminant Analysis (LDA) [11], Singular Value Decomposition (SVD) [12] and ISOMAP [13].

PCA is a linear dimension reduction technique and is the most predominant method applied [14], and was considered to compose this work.

This paper presents a method for the dimensionality reduction optimization when using a CCD sensor-based images to control Fall armyworms in agriculture. In fact, the task of image classification allows the machine to understand what type of information is contained in an image, on the other hand, semantic segmentation methods allow the precise location of different kinds of visual information, as well as each begins and ends.

After the introduction, this document is organized as follows: Section II describes the work methodology; Section III shows the results and the discussion of the experiments; and finally, Section IV presents the conclusion of this paper.

II. MATERIALS AND METHODS

A. Digital Image Sensor and Dataset

A digital image can be defined as a bi-dimensional function $f(x, y)$, where (x, y) are the intensity positions, defined as pixel [15]. CCD's sensors can capture images in different color spaces, however, the most common color space is the Red Green, and Blue (RGB), which represents the visible spectrum [16].

Table I presents the features of the images acquired using the CCD sensor.

TABLE I
IMAGE FEATURES ACQUIRED BY CCD SENSOR

Image type	JPG / JPEG
Color space	RGB
Width	3072 pixels
Height	2048 pixels
Resolution	72 pixels per inch (ppi)
Pixel size	0,35mm

Regarding the image acquisition, a dataset was generated using a CCD sensor. This dataset is composed of the Fall armyworm images in real maize crops, where the pest was found both in leaves and cobs maize.

B. Feature Extraction

The Hu invariant moments descriptor was considered for the extraction of the geometric features of the pest. For the calculation of the seven invariant moments of Hu, it is necessary, a priori, to calculate the two-dimensional moments, that is, the central moments and normalized central moments [17]. Two-dimensional moments are understood to be the polynomial functions projected onto a 2D image, $f(x, y)$, and size $M \times N$ and order $(p + q)$.

The normalized central moments allow the central moments to be invariant to scale transformations, being defined by:

$$\eta_{pq} = \frac{\mu_{pq}}{\mu_{00}^{\gamma}} \tag{1}$$

where γ is defined as:

$$\gamma = \frac{p+q}{2} + 1 \tag{2}$$

for $p + q = 2, 3, ...,$ positive integers $\in \mathbb{Z}$.

In this way, the invariant moments can be calculated considering:

$$\phi_1 = \eta_{20} + \eta_{02} \tag{3}$$

$$\phi_2 = (\eta_{20} - \eta_{02})^2 + 4\eta_{11}^2 \tag{4}$$

$$\phi_3 = (\eta_{30} - 3\eta_{12})^2 + (3\eta_{21} - \eta_{03})^2 \tag{5}$$

$$\phi_4 = (\eta_{30} + \eta_{12})^2 + (\eta_{21} + \eta_{03})^2 \tag{6}$$

$$\begin{gathered}\phi_5 = (\eta_{30} - 3\eta_{12})(\eta_{30} + \eta_{12}) \\ [(\eta_{30} + \eta_{12})^2 - 3(\eta_{21} + \eta_{03})^2] + (3\eta_{21} - \eta_{03}) \\ (\eta_{21} + \eta_{03})[3(\eta_{30} + \eta_{12})^2 - (\eta_{21} + \eta_{03})^2]\end{gathered} \tag{7}$$

$$\begin{gathered}\phi_6 = (\eta_{20} - \eta_{02})[(\eta_{30} + \eta_{12})^2 - (\eta_{21} + \eta_{03})^2] + \\ 4\eta_{11}(\eta_{30} + \eta_{12})(\eta_{21} + \eta_{03})\end{gathered} \tag{8}$$

$$\begin{gathered}\phi_7 = (3\eta_{21} - \eta_{03})(\eta_{30} + \eta_{12}) \\ [(\eta_{30} + \eta_{12})^2 - 3(\eta_{21} + \eta_{03})^2] + \\ (3\eta_{12} - \eta_{30})(\eta_{21} + \eta_{03})[3(\eta_{30} + \eta_{12})^2 - (\eta_{21} + \eta_{03})^2]\end{gathered} \tag{9}$$

Neither of the seven Hu invariant moments is directly related to the size of an object in an image. However, the size of an object can be indirectly inferred through either the first or fourth moment [18].

After the features are extracted using the methods considered, a single feature vector is organized. Then, to reduce its dimensionality, PCA is applied [19].

C. Principal Components Analisys

PCA considers an array $\mathbf{X}$ of data with n samples representing the number of observations and m independent variables [20], that is:

$$\mathbf{X} = \begin{bmatrix} x_{11} & \cdots & x_{1m} \\ \vdots & \ddots & \vdots \\ x_{n1} & \cdots & x_{nm} \end{bmatrix} \tag{10}$$

Herein, the principal components are obtained for a set of m variables X_1, X_2, ..., X_m with means μ_1, μ_2, ..., μ_m and variance σ_1^2, σ_2^2, ..., σ_m^2, which are independent and have covariance between the n-th and m-th variable [8], in the form:

$$\mathbf{\Sigma} = \begin{bmatrix} \sigma_{11}^2 & \cdots & \sigma_{1m}^2 \\ \vdots & \ddots & \vdots \\ \sigma_{n1}^2 & \cdots & \sigma_{nm}^2 \end{bmatrix} \tag{11}$$

where $\mathbf{\Sigma}$ represents the covariance matrix. To do this, the pairs of eigenvalues and eigenvectors are found (λ_1, e_1), (λ_2, e_2), ..., (λ_m, e_m), where $\lambda_1 \geq \lambda_2 \geq ... \geq \lambda_m$ and associated with Σ [21], where the i-th principal component is defined by:

$$Z_i = e_{i1}X_1 + e_{i2}X_2 + ... + e_{im}X_m \tag{12}$$

where Z_i is the i-th principal component. The objective is to maximize the variance of Z_i, as:

$$Var(Z_i) = Var(e_i'\mathbf{X}) = e_i'Var(\mathbf{X})e_i = e_i'\mathbf{\Sigma}e_i \tag{13}$$

where i = 1, ..., m. Thus, the spectral decomposition of the matrix $\mathbf{\Sigma}$ is given by $\mathbf{\Sigma} = \mathbf{P\Lambda P'}$, where $\mathbf{P}$ is the composite matrix by the eigenvectors of $\mathbf{\Sigma}$, and $\mathbf{\Lambda}$ the diagonal matrix of eigenvalues of $\mathbf{\Sigma}$ [22]. Thus, it has to be:

$$\mathbf{\Lambda} = \begin{bmatrix} \lambda_1 & 0 & \cdots & 0 \\ 0 & \lambda_2 & \cdots & 0 \\ \vdots & \vdots & \ddots & \vdots \\ 0 & 0 & \cdots & \lambda_m \end{bmatrix} \tag{14}$$

In general, the principal component of greatest importance is defined as the one with the greatest variance which explains the maximum variability in the data vector. The second most important component is the component that has the second highest variance, and so on, up to the least important component [12].

Likewise, the normalized eigenvectors represent the main components that constitute the feature vector with reduced dimension. Besides, such reduced components are used to describe the acquired images. Additionally, the reduced features are used for the recognition of the patterns of Fall armyworm (*Spodoptera frugiperda*), i.e., useful consideration for both cases, leaf or cob maizes.

ISBN: 978-1-68558-164-0

III. RESULTS AND DISCUSSION

For this study, an image dataset composed of 2280 images acquired with CCD's sensor was used. These images represent the Fall armyworm (*Spodoptera frugperda*) acquired in a real environment of maize crop in its five different stages of growth, grouped in 456 images for each stage. Figure 1(a to e) illustrates one example of each stage of growth, also named Instar, Figure 1(f) illustrates two different Instar in the same image.

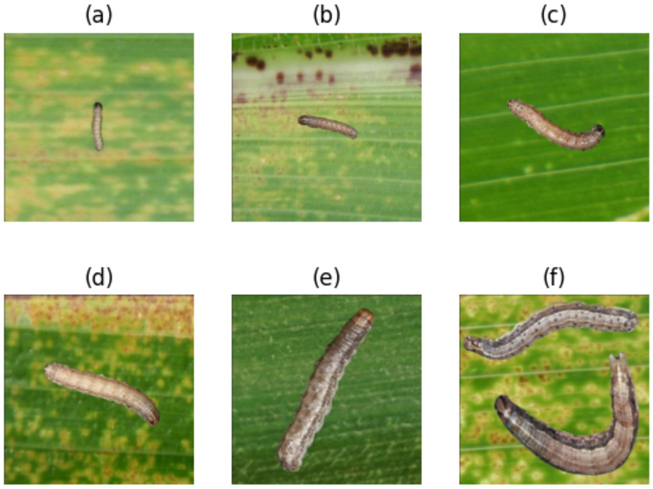

Fig. 1. Fall armyworm (*Spodoptera frugperda*) in different stages of growth.

Considering all images contain at least one specimen of the pest in different stages, in other words, different sizes, the Hu invariant moments descriptor has been considered for instance. Thus, for each image of the Fall armyworm, a feature vector was generated, containing the seven Hu invariant moments (ϕ_1, ϕ_2, ϕ_3, ϕ_4, ϕ_5, ϕ_6 and ϕ_7), which are related to the shape and geometrical features of this pest. The features contained in these vectors will allow the classification of the Fall armyworm (*Spodoptera frugperda*) in its different stages of growth.

Table II presents the seven Hu invariant moments, as examples, from three different images, which were processed using the dataset.

TABLE II
FEATURE VECTOR COMPOSED OF HU INVARIANT MOMENTS. EXAMPLE OF THREE IMAGES

Hu invariant moments	**Images**		
	Image 1	**Image 2**	**Image 3**
ϕ_1	6.692	6.6178	6.524
ϕ_2	13.581	13.424	19.102
ϕ_3	24.321	23.944	22.370
ϕ_4	25.919	26.245	23.445
ϕ_5	51.517	-52.023	46.665
ϕ_6	34.307	-33.305	-34.728
ϕ_7	-51.458	-51.556	47.656

As the values of the feature vectors were in different scales, it was necessary to normalize them. To generate a database of characteristics of the fall armyworm (*Spodoptera frugperda*), the feature vectors referring to each image were saved on disk.

Table III presents the normalized seven Hu invariant moments from three different images.

TABLE III
NORMALIZED FEATURE VECTOR. EXAMPLE OF THREE IMAGES

Hu invariant moments	**Images**		
	Image 1	**Image 2**	**Image 3**
ϕ_1	0.274	0.162	0.021
ϕ_2	-1.048	-1.121	1.496
ϕ_3	1.035	0.817	-0.092
ϕ_4	1.408	1.669	-0.575
ϕ_5	0.719	-1.607	0.610
ϕ_6	0.808	-1.289	-1.333
ϕ_7	-0.863	-0.865	1.199

To remove duplicate information and also non-significant information, this stage first proceeds to the dimensionality reduction of the feature vector through PCA. To achieve the appropriate number of principal components that explain the original data, seven principal components were measured.

Through the variance ratio metric, it was possible to measure how much each of the seven principal components was explained from the original data. Figure 2 shows the variance ratio.

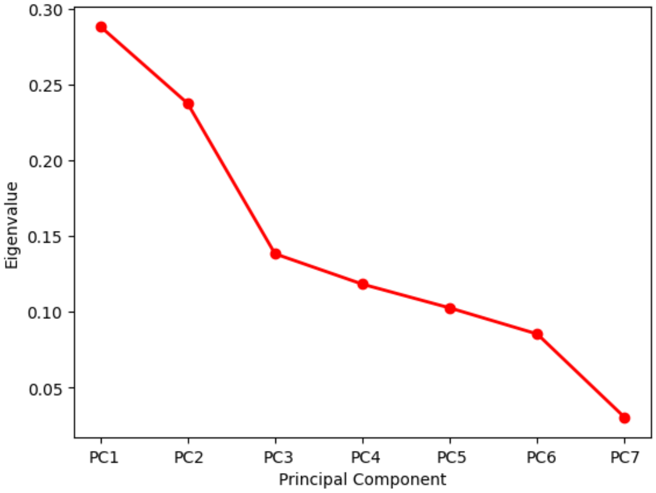

Fig. 2. Scree plot.

Analyzing the scree plot in Figure 2, it is possible to infer that by applying two to four principal components it is possible to explain almost from 55% to 80% of the variability of the original data. Considering that, the experiments were based on four principal components.

As discussed in the prior section, neither of the seven invariant moments is directly related to the size of an object. However, the first and the fourth moments can be used to infer the size of an object in an image.

Moreover, through the maximum variation ratio metric it is possible to measure the weight of each of Hu invariant moments in each principal component.

Table IV presents the maximum variance to each of the four principal components concerning the original data.

TABLE IV
MAXIMUM VARIATION OF DATA IN RELATION TO EACH PRINCIPAL COMPONENT. BASED ON FOUR PRINCIPAL COMPONENTS.

Hu invariant moments	**Principal components**			
	PC 1	**PC 2**	**PC 3**	**PC 4**
ϕ_1	-0.147	-0.630	-0.120	-0.568
ϕ_2	0.501	-0.295	0.036	0.230
ϕ_3	-0.395	-0.424	0.087	0.027
ϕ_4	-0.378	0.501	-0.158	-0.479
ϕ_5	-0.376	-0.277	-0.310	0.286
ϕ_6	-0.355	-0.011	0.865	0.127
ϕ_7	0.398	-0.078	0.325	-0.543

Even though some values presented in Table IV are negative, the weights for each principal component are considered absolute values. For example, in PC2, the first moment (ϕ_1) has the highest weight.

Figure 3 illustrates the maximum variance to each of the four principal components concerning the original data with the absolute values.

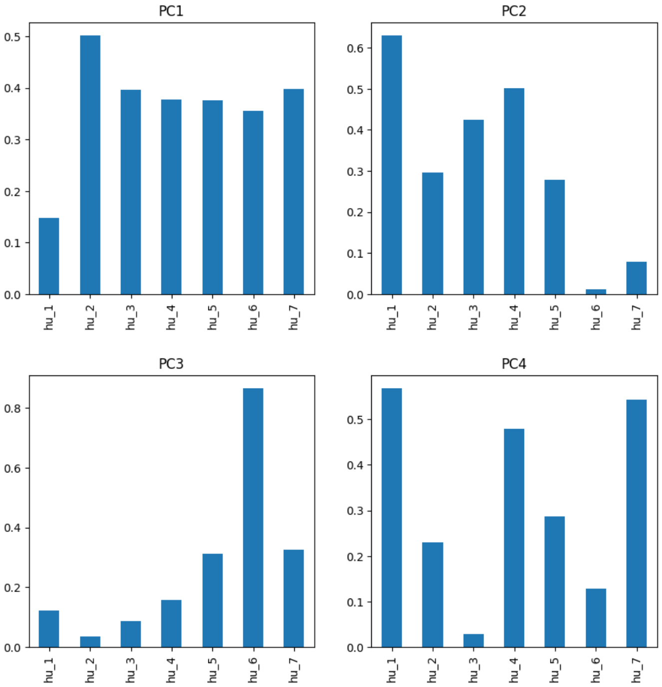

Fig. 3. Maximum variation of data in relation to each principal component, based on four principal components.

The experiment with four principal components showed that, as can be visualized in Figure 3, to have the most representative weights either from the first moment or the fourth moment, it was necessary to work with two or four principal components.

Based on prior experiments, the dimensionality reduction of the feature vector was performed. Table V presents the values of the four principal components.

TABLE V
FEATURE VECTOR COMPOSED OF FOUR PRINCIPAL COMPONENTS. EXAMPLE OF THREE IMAGES

Principal components	**Images**		
	Image 1	**Image 2**	**Image 3**
PC1	0.333	2.121	-0.742
PC2	-2.280	-1.156	1.306
PC3	0.551	-1.243	-0.528
PC4	0.181	-1.193	0.012

The distribution of the variation of the four principal component values is illustrated in Figure 4.

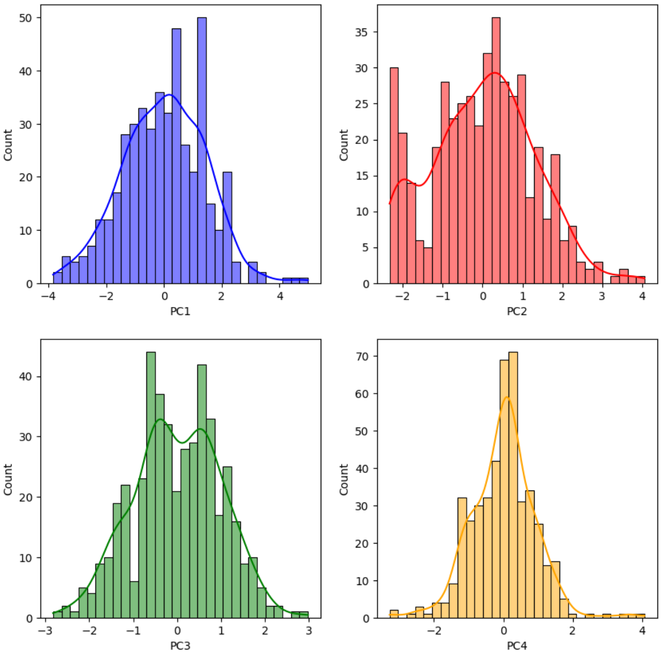

Fig. 4. Histogram of distribution of the four principal components values.

Once the values of the four principal components are obtained, it is necessary to evaluate if it is sufficient to work with two principal components, or whether it should be considered four principal components. For this purpose, it should be considered the maximum variation of each principal component to the original data, how much the principal components could explain the original data, and also the minimum error.

This information can be observed in Figure 5, which illustrates a boxplot chart of the four principal component values and their distribution.

From Figure 5, it is possible to visualize that when working with two or three principal components the error would be minimal, but with two principal components only 55% of the original data is explained, and working with three principal components the first and fourth moments are not representative.

This experiment demonstrated that working with four principal components was the ideal option. Because both the first and fourth moments are very representative, four principal

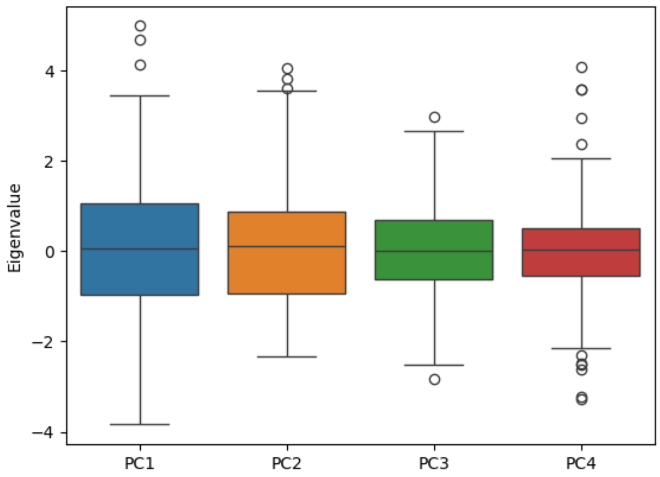

Fig. 5. Boxplot of four principal components values.

components can explain 80% of the original data, and even with a low increase in the error, it is not considerable to decrease the estimation.

IV. CONCLUSIONS

This paper presented a study of dimensionality reduction using Principal Components Analysis (PCA), considering feature vectors composed of extracted Hu invariant moments.

Before measuring the number of principal components necessary to represent the original data from the Fall armyworm digital images, the feature vectors were normalized, to obtain all the seven Hu invariant moments.

The measure of the explained variance ratio to the original data was applied to verify the quantity number of principal components necessary to explain the maximum of the original data.

In addition, the first and fourth invariant moments were used to infer the estimated size of the Fall armyworm (*Spodoptera frugperda*) in the images. Likewise, the measure of the maximum variation of each principal component, concerning to each Hu invariant moment, was performed to find how much these moments contribute to recognizing the main elements acquired with the CCD's sensor.

The measurements show that computing two to four principal components was sufficient to explain 55% to 80% of the original data, and either the first or fourth moments were contained in two and four principal components.

Finally, despite seven invariant moments being used, such analysis led to the conclusion that when using 4 principal components, one may achieve the explanation of 80% for the original data, with low error, as well as, not a significative variation.

For future works, it is suggested to extend this research to an unsupervised method to reach the selection of the number of principal components to remain with the semantic features from a recognized agricultural pest.

ACKNOWLEDGMENT

This research was partially supported by the São Paulo Research Foundation (FAPESP 17/19350-2). We thank the Brazilian Corporation for Agricultural Research (Embrapa) and the Post-Graduation Program in Computer Science from the Federal University of São Carlos (UFSCar). The Authors also recognize the helpful discussions with MSc Bruno M. Moreno to finalize the manuscript.

REFERENCES

[1] C. Zhang, H. Hu, D. Fang, and J. Duan, "The ccd sensor video acquisition system based on fpga&mcu," in *2020 IEEE 9th Joint International Information Technology and Artificial Intelligence Conference (ITAIC)*, vol. 9. IEEE, 2020, pp. 995–999.

[2] S. Sankaran, R. Ehsani, and E. Etxeberria, "Mid-infrared spectroscopy for detection of huanglongbing (greening) in citrus leaves," *Talanta*, vol. 83, no. 2, pp. 574–581, 2010.

[3] J. L. Miranda, B. D. Gerardo, and B. T. T. III, "Pest detection and extraction using image processing techniques," *International journal of computer and communication engineering*, vol. 3, no. 3, pp. 189–192, 2014.

[4] C. Ji *et al.*, "Big data processing: Big challenges and opportunities," *Journal of Interconnection Networks*, vol. 13, no. 03n04, p. 1250009, 2012.

[5] W. K. Vong, A. T. Hendrickson, D. J. Navarro, and A. Perfors, "Do additional features help or hurt category learning? the curse of dimensionality in human learners," *Cognitive science*, vol. 43, no. 3, p. e12724, 2019.

[6] A. L. M. Levada, "Parametric PCA for unsupervised metric learning," *Pattern Recognition Letters*, vol. 135, pp. 425–430, 2020.

[7] F. Anowar, S. Sadaoui, and B. Selim, "Conceptual and empirical comparison of dimensionality reduction algorithms (PCA, KPCA, LDA, MDS, SVD, LLE, ISOMAP, LE, ICA, t-SNE)," *Computer Science Review*, vol. 40, p. 100378, 2021.

[8] S. Ayesha, M. K. Hanif, and R. Talib, "Overview and comparative study of dimensionality reduction techniques for high dimensional data," *Information Fusion*, vol. 59, pp. 44–58, 2020.

[9] K. Pearson, "LIII. On lines and planes of closest fit to systems of points in space," *The London, Edinburgh, and Dublin philosophical magazine and journal of science*, vol. 2, no. 11, pp. 559–572, 1901.

[10] A. L. M. Levada, "PCA-KL: a parametric dimensionality reduction approach for unsupervised metric learning," *Advances in Data Analysis and Classification*, vol. 15, no. 4, pp. 829–868, 2021.

[11] F. Pan, G. Song, X. Gan, and Q. Gu, "Consistent feature selection and its application to face recognition," *Journal of Intelligent Information Systems*, vol. 43, pp. 307–321, 2014.

[12] S. Nanga *et al.*, "Review of dimension reduction methods," *Journal of Data Analysis and Information Processing*, vol. 9, no. 3, pp. 189–231, 2021.

[13] Z. A. Sani, A. Shalbaf, H. Behnam, and R. Shalbaf, "Automatic computation of left ventricular volume changes over a cardiac cycle from echocardiography images by nonlinear dimensionality reduction," *Journal of Digital Imaging*, vol. 28, pp. 91–98, 2015.

[14] R. M. Wu *et al.*, "A comparative analysis of the principal component analysis and entropy weight methods to establish the indexing measurement," *PLoS One*, vol. 17, no. 1, p. e0262261, 2022.

[15] R. C. Gonzalez and R. E. Woods, *Digital image processing*. Pearson Prentice Hall, 2004.

[16] G. Saravanan, G. Yamuna, and S. Nandhini, "Real time implementation of rgb to hsv/hsi/hsl and its reverse color space models," in *2016 International Conference on Communication and Signal Processing (ICCSP)*. IEEE, 2016, pp. 0462–0466.

[17] W. Zhao and J. Wang, "Study of feature extraction based visual invariance and species identification of weed seeds," in *2010 Sixth International Conference on Natural Computation*, vol. 2. IEEE, 2010, pp. 631–635.

[18] L. Zhang, F. Xiang, J. Pu, and Z. Zhang, "Application of improved hu moments in object recognition," in *2012 IEEE International Conference on Automation and Logistics*. IEEE, 2012, pp. 554–558.

ISBN: 978-1-68558-164-0

[19] K. Hongyu, V. L. M. Sandanielo, and G. J. de Oliveira Junior, “Principal analisys components: teorical summart, aplication and interpretation, (análise de componentes principais: resumo teórico, aplicação e interpretação),” *E&S Engineering and science*, vol. 5, no. 1, pp. 83–90, 2016.

[20] B. Zhao, X. Dong, Y. Guo, X. Jia, and Y. Huang, “PCA dimensionality reduction method for image classification,” *Neural Processing Letters*, pp. 1–22, 2022.

[21] M. P. Uddin, M. A. Mamun, and M. A. Hossain, “PCA-based feature reduction for hyperspectral remote sensing image classification,” *IETE Technical Review*, vol. 38, no. 4, pp. 377–396, 2021.

[22] B. M. S. Hasan and A. M. Abdulazeez, “A review of principal component analysis algorithm for dimensionality reduction,” *Journal of Soft Computing and Data Mining*, vol. 2, no. 1, pp. 20–30, 2021.

Use of Affordable Sensors to Investigate Aeration and Resistance to Plant Root Penetration for Soil Assessment

Ladislau M. Rabello[1], Paulo S. de P. Herrmann[1], Paulo E. Cruvinel[1,2]

[1] Embrapa Instrumentation (CNPDIA), [2] Post Graduation Programme in Computer Science (UFSCar)
São Carlos, SP, Brazil.
e-mails: ladislau.rabello@embrapa.br, paulo.herrmann@embrapa.br, paulo.cruvinel@embrapa.br

***Abstract*— To understand how plant roots navigate the soil environment it is required several key factors. Instrumentation plays a crucial role in measuring these factors. Mostly of them are related to oxygen diffusion rate, which affects root respiration and growth, soil redox potential that indicates the level of available oxygen in the soil, and the resistance to root penetration. By analyzing such combined measurements, scientists can gain valuable insights into root health and plant performance in different soils conditions. This paper presents a combination of three affordable sensors to perform the measurements of those key factors, in order to provide an effective solution to enhance agricultural productivity, food security, and supporting sustainable agriculture. This innovative approach with accessible sensors offers an effective way to understand and monitor soil conditions, thus promoting more productive and sustainable issue.**

Keywords- affordable sensors; agriculture; soil resistance; soil-water-plant measuring; Oxygen Diffusion Rate (ODR), redox potential, soil aeration.

I. INTRODUCTION

The applications of sensors, and more specifically the affordable sensors, are the basis for instrumentation developing, which is also related to automation, precision agriculture, and digital agriculture.

The global agricultural sensors market size was valued at USD 4.74 billion in 2021. It is expected to reach USD 16.83 billion by 2030, growing at a Compound Annual Growth Rate (CAGR) of 15.12% during the forecast period (2022–2030) [1].

In such universe of sensors, the low-cost sensors are technologies that can attend consumer and research applications. Competitive, the low-cost sensors can be useful to attend an economy-of-scale. In fact, these technologies for sensing may allow either new applications or more economical use not only for agricultural production but also environmental use [2].

Plant roots play a crucial role for the ecosystem's health, but their growth can be hindered by various soil conditions. Understanding these limitations requires investigating factors like oxygen availability, soil chemistry, and physical properties. This is where sensor-based instrumentation can provide valuable insights related to the belowground world. One of the critical factors influencing root growth is the oxygen diffusion rate within the soil. Roots require oxygen for respiration, and their limited availability can restrict root elongation and penetration in soil [3]. Instruments like microelectrode probes can measure oxygen concentration at specific depths within the soil profile. These probes consist of fine wires that react to oxygen levels, generating an electrical signal that is related to oxygen concentration. By measuring oxygen diffusion rates across different soil types and moisture conditions, researchers can identify potentially areas limiting root growth due to hypoxia (low oxygen availability) [4][5].

Another critical parameter is soil redox potential, often abbreviated as Eh. Its measurement reflects the overall tendency of the soil environment to gain or lose electrons. A positive Eh indicates a more oxidizing environment favorable for root growth, while negative values suggest a reducing environment with limited oxygen and CO_2 availability in paddy fields [6]. Instruments like redox electrodes are used to measure Eh. These electrodes generate a voltage based on the soil's electron activity, allowing researchers to assess the overall oxidative state and predict potential limitations for root development.

Finally, resistance to root penetration is other a crucial factor affecting root growth. This resistance can be caused by soil compaction, rocks or debris, and even root hairs of other plants [7]. Penetrometers are instruments used for measuring such a soil-resistances to root penetration. These devices typically consist of a metal rod with a force sensor. The rod is pushed into the soil at a controlled rate, and the force required for penetration can be measured. Such collected data may help researchers to understand roots' physical limitations as they navigate the soil matrix.

By combining data on oxygen diffusion rate, soil redox potential, and resistance to root penetration, researchers comprehensively understand the factors influencing root growth in a dynamics way [8]. Based on such information one can develop strategies for improving soil health, such as practices that enhance aeration, drainage, and organic matter content. Understanding these factors also has significant implications for agriculture, i.e., in terms of value aggregation. Optimizing soil conditions for root growth can lead to healthier plants with improved nutrient uptake, better water utilization, and increase in crop yields.

The main objective of this work is to present a sensors-based instrument for investigating aeration (Oxygen Diffusion Rate (ODR) and Redox potential (Eh)), and the resistance to root penetration in soil (SSRPM) assessment.

In Section II, a discussion is carried out regarding the systems in relation to their operation, theoretical and practical data, as well as the modeling of them.

In addition, in Section III are presented conclusions and a proposal for future works.

II. APPLICATION, EVALUATION AND EXAMPLES OF CUSTOMIZED AND AFFORDABLE ODR, EH AND SSRPM SENSORS FOR AGRICULTURE.

The system consists of three sensors: soil oxygen diffusion rate sensor, soil redox potential sensor, and soil resistance to root penetration sensor; a computational system with analog-to-digital converter and digital signal processor, responsible for reading and acquiring signals from the sensors and processing them; and a Human-Machine Interface (HMI) for graphical or text visualization of the processed signals, like a Dashboard.

Figure 1 shows in block diagram the organized structure for the accessible sensors used to investigate soil aeration and soil resistance to root penetration.

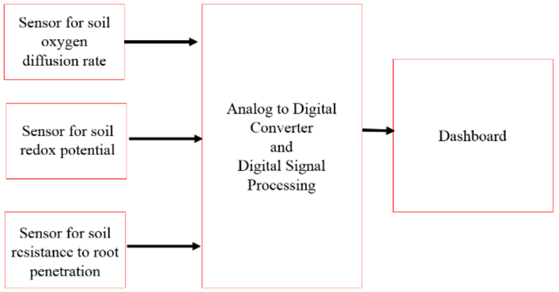

Figure 1. Block diagram for root soil information processing and related instrumentation based on the use of affordable sensors.

Related to the development and use of oxygen diffusion rate and redox potential sensors, both can be used in laboratory experiments and also in agricultural plots. In relation of these two key-factors sensors, the instrumental arrangement was prepared take into account an advanced version in relation that presented by Silveira and collaborates [9]. The main advances in this new arrangement were: the replacement of the analog reading system with a digital one, with the two readings (ODR and redox potential) being presented on a 3 1/2-digit LCD (Liquid Crystal Displays). The selection of these sensors is made by using a high-performance micro relay, activated by a thumbwheel switch instead of a wave switch.

The electrodes were constructed using electrostatic welding, a process similar to that used in the preparation of thermocouples, which fuses the platinum wire (sensor) to the copper wire (connection between the sensor and the device). The electrodes were then wrapped with acrylic resin, which provides mechanical resistance and precisely controls the length of the platinum wire exposed for measurement. The electrode length is an important parameter, since the ODR is dependent on the sensor area, given by (1) and (2). This manufacturing process simplified the construction of the sensors, compared to that proposed in [8][10], which consists of fusing a glass tube together with platinum wire and copper wire. Such a process can cause contact problems, and it is difficult to accurately control the length of the exposed platinum wire, i.e., improvement was required.

A. Oxygen Diffusion Rate (ODR)

To measure ODR, a potential of 0.65 VDC is applied between the platinum electrodes and the calomel electrode [11]. After a minimum of four minutes, the current stabilizes, and a microampmeter is ready to be read.

According to [9], the current that circulates between the two electrodes is proportional to the ODR in the soil and can be expressed by (1), which is an adaptation of Fick's diffusion law:

$$i = 10^{-6} = \eta * F * A * f \tag{1}$$

Where i is the electric current in microamperes, n is the number of electrons required to reduce an oxygen molecule, which is equal to 4, F is the Faraday's constant (approximately equal to 9.65 x 10^4 C/mol), A is the surface area of the platinum electrode (cm^2) and f is the flux or ODR to the electrode surface, in number of moles of oxygen per second per cm^2.

The ODR can be calculated in ($\mu g.cm^{-2}.min^{-1}$), using (2):

$$ODR = \frac{(i * 10^{-6}) * 60 * (32 * 10^{8})}{4 * 96.500 * A} \tag{2}$$

Where the factors 60 and 32 x 10^8 are used to convert seconds and moles to minutes and micrograms [10].

B. Redox Potential (Eh)

When measuring the redox potential, the electrode voltage is deactivated and they are connected to the input of the operational amplifier, in a non-inverting configuration (Figure 2). The output of the operational amplifier is connected to a digital voltmeter to read the electrode potential, which by definition of the “International Union of Pure and Applied Chemistry” (IUPAC), it is the availability of the electron or the electrochemical potential of the electron in equilibrium.

The electrode potential, whose adopted symbol is Eh, is related to the oxidation distribution state of the ion by the Nernst equation:

$$Eh = Eh^0 - \frac{R * T}{n * F} * ln \frac{(Red)}{(O_x) * (H^+)} \tag{3}$$

Where Eh is the cell potential in Volts, n is the number of electrons transferred in a half reaction (this is when the chemical equation related to the cell reaction can be separated into two portions) generalized from a redox couple, R is the universal gas constant 8.3145 (J.K^{-1} .mol^{-1}), Red = Ox + ne-+ aH^{+} (called half reduction), and T is the temperature in Kelvin. In (3), "Red" and "Ox" refer, respectively, to the reduction and oxidation forms of substances, and Eh° is called the standard potential for the half-reaction [12].

The choice of the 0.35 mm platinum electrode is due to two experimental aspects: 1) characterization of the ODR conditions for root thickness with the same dimension as the electrode, and 2) stiffness of the wire, to avoid its breakage when of its insertion into the soil.

The dimensions of the platinum wire alter the geometry of the solid-liquid-gaseous state of the medium around the electrode, which may not appropriately characterize the oxygen diffusion that a root requires. The correct quantification of ODR, together with other parameters, makes it possible to correlate the degree of root growth to its environment [13][14].

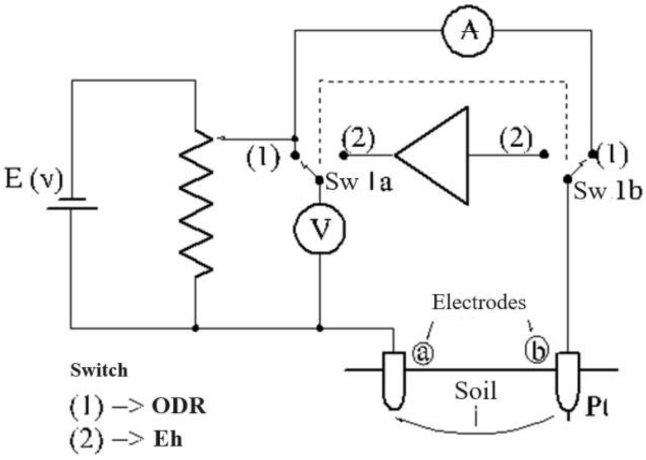

Figure 2. Schematic diagram for measurements of ODR, and Eh.

Figure 3 presents the results that show the influence of water in the water-soil system, in the attenuation of microwaves, through the relation of the attenuation of the signal in dB by the volumetric soil moisture in sandy soil (1.20 < soil density (g/cm^3) < 1.26), clayey (0.83 < soil density (g/cm^3) < 0.92)) and glass microsphere (1.13 < soil density (g/cm^3) < 1.19)). The error in sample preparation was 4.7%. All measurements were conducted under laboratory conditions (room temperature ~23.0 ± 0.5 ^{0}C and relative humidity 36%).

Figure 4 shows the correlation (R2 =0.937) between the results obtained in five measurements with the redox potential meter developed and a Digimed DM-PV. The differences between these results can be explained by the spatial variation of the redox potential that occurs in the field (point measurements), and therefore the analysis of redox potential in the field is more qualitative than quantitative. Readings with values greater than +200 mV (pH 7) denote oxidized conditions, and values lower than this demonstrate reduced conditions in the soil [15].

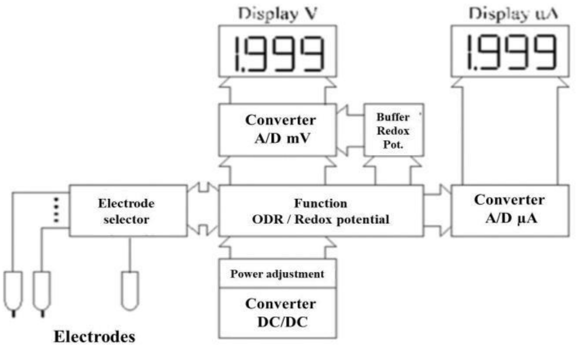

Figure 3. Block diagram of the sensor-based arrangement to obtain the oxygen diffusion rate and redox potential.

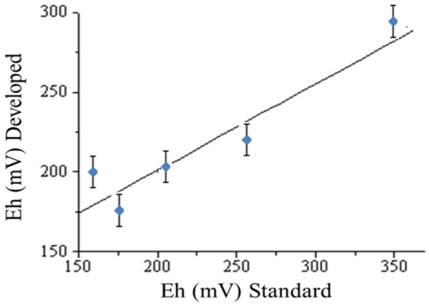

Figure 4. Correlation of data obtained in the field (R^2= 0.937) with the redox potential meter, developed and produced by Digimed equipment, being used as a comparison standard (error bar based on the standard deviation of the measurement).

Figure 5 shows the relationship between the soil matric potential and the ODR variation. This type of result, with an increase and subsequent reduction in ODR with variation in humidity, has been observed by other authors and is an artifact of the ODR technique [9][11].

As the ODR method is based on the movement of oxygen in the liquid phase of the soil, this has been explained by the rupture of the water film around the electrode, at low humidity values [8]. Therefore, only ODR measurements at high humidity levels are more appropriate.

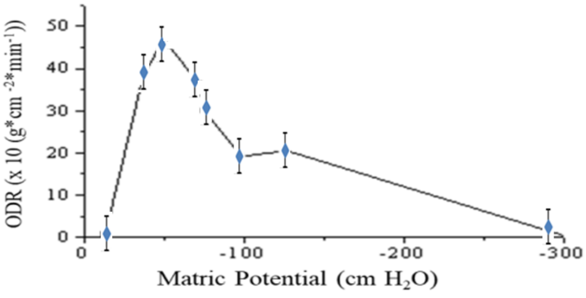

Figure 5. Variation of Oxygen Diffusion Rate (ODR) (x 10 (g*cm $^{-2}$*min^{-1})) as a function of soil water matric potential (cm H$_2$0) (error bar based on the standard deviation of the measurement).

C. Sensor for Soil Resistance to Root Penetration Measurements (SSRPM)

A sensor-based instrumentation was prepared to evaluate the spatial variability of soil resistance to root penetration, for area and profile and due to natural or artificial soil compaction processes. Many researchers have studied the formation of surface layers of soil compaction and its effects on seed emergence, water infiltration, and soil erosion. Penetrometers do not have reasonable precision for measuring the degree of compaction of compacted soil crust and for quantifying the force exerted by seed during germination to overcome this crust and root development in this region. Small probes have been used to simulate root penetration force but on a laboratory scale to characterize soil structure.

The SSRPM was developed (cone angle of 30º, base diameter of 1.6 mm, and total length of 130 mm), based on the ASAE R 313.3 standard for penetrometers [16], sensed by a load cell and electronic circuit for signal conditioning and treatment.

Results have shown that measurements of soil resistance to root penetration could be accomplished up to (49.03±0.07) kgf, with a resolution equal to 1.57 kgf.

Calculations for values of Soil Resistance to Penetration (RSP) as a function of the normal stress under the probe's metal cone (σ_n), friction (μ), tangential adhesion stress (c_a), soil Resistance to Cone Penetration (RP), soil density (ρ) and soil moisture (θ), can be given as follows [17][18].

$$RSP = g(\sigma_n, \mu, c_3, RP, \rho, \theta) \tag{4}$$

Likewise, the RSP also can be represented by the equation (5).

$$RSP = 6.98 * \rho^2 + A + B + C - D - 10.44 * 10^{-2} \tag{5}$$

where:

$$A = [-1.62 * 10^{-1} + 1.36 * 10^{-3}(A_1)] * \rho$$

$$A_1 = h_a + R_c\left(\frac{RP - \sigma_n}{(\mu * \sigma_n) + c_a}\right)$$

$$B = [1.98 * 10^{-1} - 9.20 * 10^{-3}(B_1)] * (\theta * \rho)$$

$$B_1 = h_a + R_c\left(\frac{RP - \sigma_n}{(\mu * \sigma_n) + c_a}\right)$$

$$C = 9.80 * 10^{-2}\left[h_a + R_c\left(\frac{RP - \sigma_n}{(\mu * \sigma_n) + c_a}\right)\right]$$

$$D = 2.0 * 10^{-3}\left[h_a + R_c\left(\frac{RP - \sigma_n}{(\mu * \sigma_n) + c_a}\right)\right]$$

h_a is the height of the microprobe within the soil, and R_c is the cone radius of the microprobe tip, equal to 0.08 cm.

For validation, a 13 cm probe was used, designed without the recess in the probe body and maintaining the cone tip angle equal to 30º. The test aimed to evaluate the behavior of the soil resistance to root penetration sensor is illustrated in Figure 5. In deeper measurements of soil resistance to root penetration for maize (Zea Mays), results reach approximately 20 cm deep.

For validation, an agricultural plot was used, i.e., located at coordinates 21º 57' 5.33728 S" and 47º 50' 45.9429 W", area from Embrapa Southeastern Livestock, located in the municipality of São Carlos, São Paulo state, Brazil.

The region's soil type comprises a *Dark Red Dystrophic Latosol*, which presents a clayey texture in the tropical sub deciduous savanna phase. These deep soils range from reddish-brown to dark reddish-brown. They are formed from very diverse material, which give them a specific variability in morphological characteristics and influences their chemical properties. In general, these soils have low base saturation and low aluminum saturation.

Data was collected within an area of 16 cm X 16 cm, with a variation of 1 cm distance between them. A computer program was responsible for controlling a table of coordinates XY, as well as to carry out the data acquisition [19]. The coordinates provided to the sensor-based system are indicated in Table 1.

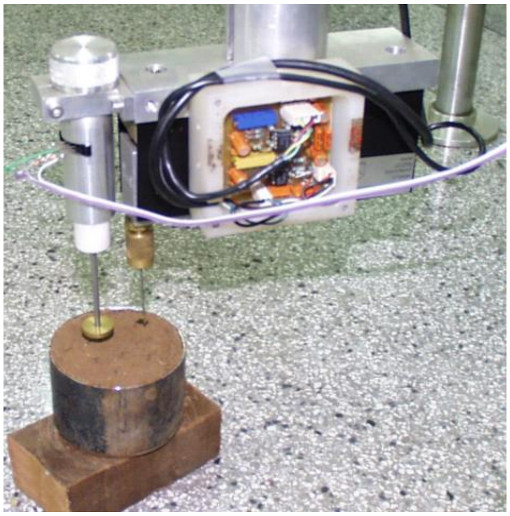

Figure 5: illustration of *SSRP arrangement* for laboratory calibration.

TABLE I. FIELD TEST FOR 13 CM PROBE - COORDINATES TO MEASURE SOIL RESISTANCE TO ROOT PENETRATION.

starting position		end position		Increment	
X(cm)	Y(cm)	X(cm)	Y(cm)	X(cm)	Y(cm)
0	0	15	15	1	1

Table II summarizes the parameters of the carried-out analysis with the 13 cm probe.

TABLE II. SOIL MOISTURE FOR TESTING WITH A 13 CM PROBE.

Container number	1.0
Sample thickness	7.2 cm
Sample length	5.5 cm
Average soil moisture in experiment area <***θ***>	11.3%
Soil type	Dark Red Dystrophic Latosol - clayey texture

With the aim of characterizing the field test, as well as due to the large amount of data, two coordinates were selected, (440,120) and (110,60), to verify the variation in soil resistance to root penetration, represented in figure 6(a) (b), as a function of depth Z, in the range of 0 to 30 mm and 0 to 130 mm respectively.

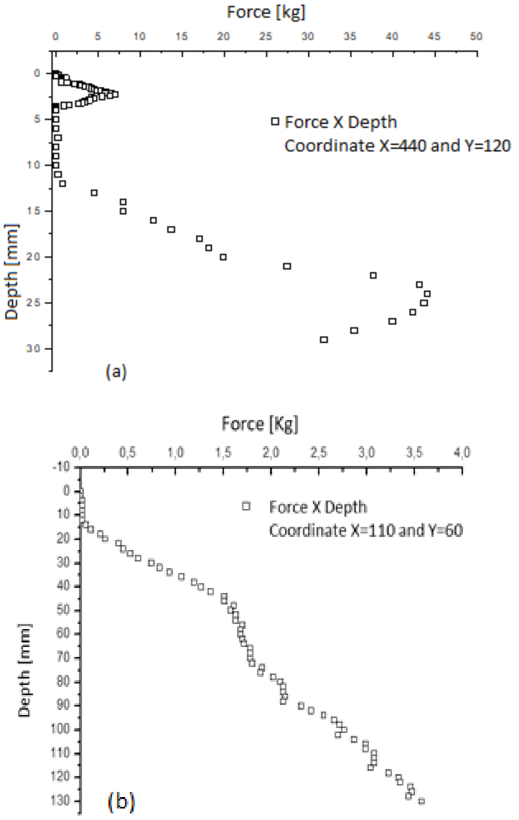

Figure 6: Variation in soil resistance to root penetration for the 3cm (a) and 13cm (b) probe as a function of depth Z, for coordinates (X=440, Y=120) and (X=110, Y=60) respectively.

The sequence of two-dimensional maps, generated from different depths is shown in Figure 7. In such evaluation, variation in resistance to the advancement of the probe was observed throughout the entire depth, which would also be the case for plant roots.

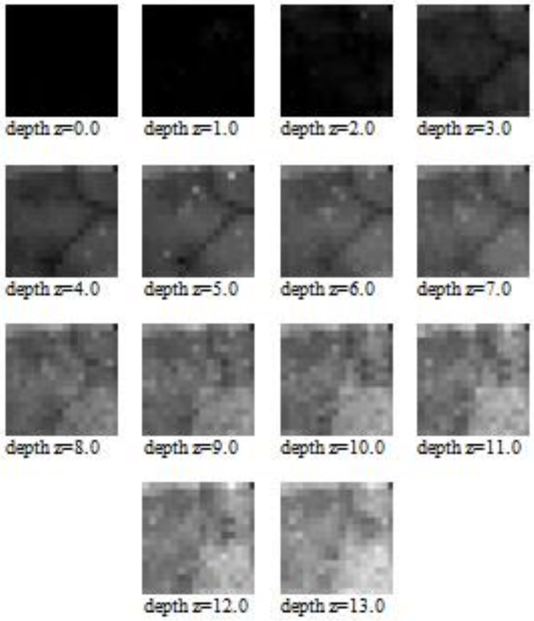

Figure 7. Sequence of two-dimensional maps of measures of soil resistance to root penetration for data collected in the field for the 13 cm, in the range from z=0.0 cm to z=13.0 cm, shades of gray: from black =0.0 kgf to white=50.0 kgf

The volumetric information on soil resistance to root penetration obtained in the field test from the two-dimensional maps for the 13 cm probe, with its transversal, coronal and sagittal sections, is seen in Figure 8.

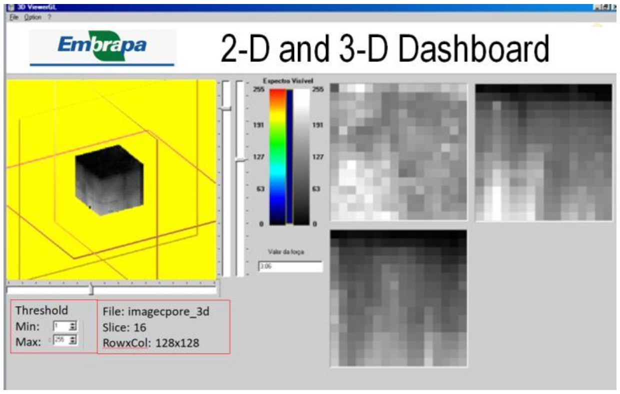

Threshold
Min: 1
Max: 255

File: imagecpore_3d
Slice: 16
RowxCol: 128x128

Figure 8: Three-dimensional map of soil resistance to root penetration, collected in an agricultural field using the 13cm probe.

The presented results related to the soil resistance to root penetration analysis made it possible to measure soil resistance to a depth of 13 cm in almost real time. In addition, after the sensor's integration in a unique instrumental platform, an embedded software was also included for spatial variability analysis.

III. CONCLUSIONS AND FUTURE WORK

In this study, three affordable sensors were introduced that have proven to be quite useful in soil science studies. These sensors can be seamlessly combined. Results have demonstrated that the sensors are capable of accurately evaluating redox potential, oxygen diffusion rate, and aeration, even in soil that is nearly saturated, as well as the soil resistance to root penetration. The reached level of precisions makes the final arrangement with the three sensors ideal for agricultural applications.

As future work, there are plans to integrate sensors into an ARM architecture (Acorn RISC Machine) and incorporate computational intelligence to aid decision making in the agricultural setting.

ACKNOWLEDGMENT

This work was supported by Embrapa Instrumentation.

REFERENCES

[1] Agricultural Sensors Market Growth, Share, Forecast to 2030. https://straitsresearch.com/report/agricutural-sensors-market#:~:text=Market%20Snapshot&text=The%20global%20agricultural%20sensors%20market,period%20(2022%E2%80%932030) 2021 (accessed in 05/06/2024).

[2] M. Kückelhaus and G. Chung, “Logistics Trend Radar, DHL Customer Solutions & Innovation”, Germany. Retrieved from www.dhl.com. 2013 (Accessed 05.06.2024).

[3] I. Ben-Noah and S. P. Friedman, “Review and evaluation of root respiration and of natural and agricultural processes of soil aeration”. Vadose Zone J. vol. 17, pp. 170119, 2018. doi:10.2136/vzj2017.06.0119

[4] S. D. Logsdon, “Within Sample Variation of Oxygen Diffusion Rate”. Soil Science, vol. 168, no. 8, pp. 531-539, August 2003. | doi: 10.1097/01.ss.0000085052.25696.c0

[5] P. S. P. Herrmann, M. G. de Andrade, L. A. Colnago, and P. M. da Silveira, “Equipment for measuring soil oxygen diffusion rate and redox potential ”. Pesquisa Agropecuária Brasileira, Brasília, vol. 32, no. 7, pp. 725- 730, 1997.

[6] J. Li et al., “Elevated CO2 increases soil redox potential by promoting root radial oxygen loss in paddy field”. Journal of Environmental Sciences, vol. 136, pp. 11-20, 2024 DOI: 10.1016/j.jes.2023.01.003

[7] A. G. Bengough and C. E. Mullins, “Penetrometer resistance, root penetration resistance and root elongation rate in two sandy loam soils”. Plant Soil. vol. 131, pp. 59–66 1991, doi.org/10.1007/BF00010420

[8] S.L. Drahorad and P. Felix-Hemingsen;. “An electronic micropenetrometer (EMP) for field measurements of biological soil crust stability”. Journal of Plant Nutrition and Soil Science, vol. 174, no. 4, pp. 519-520. https://doi.org/10.1002/jpln.2012000.

[9] P. M. da Silveira, B. Fernandes and P. H. Henriques, “Assembly of the meter and evaluation of the soil oxygen diffusion rate (SOD)”. ITEM- Irrigação e Tecnologia Moderna, Brasília, n. 29, pp. 37-39, 1987.

[10] J. Letey and L. H. Stolzy, “Measurement of oxygen diffusion rates with the platinum microelectrode: correlation of plant response to soil oxygen diffusion rate”, Hilgardia, Berkeley, vol. 35, no. 20, pp. 567-576,1964DOI:10.3733/hilg.v35n20p545

[11] C. J. Phene, “Oxygen electrode measurement”. In: methods of soil analysis. Part 1. Physical and mineralogical methods. St. Joseph: ASA JSSSA, 1986. pp. 1137-1159. (ASA. Agronomy, 9) doi.org/10.2136/sssabookser5.1.2ed.c49

[12] G. W. Ewing, “Instrumental methods of chemical analysis” ed. 4. New York: McGraw-Hill, pp. 560, 1975

[13] J. Letey and L. H. Stolzy, “Measurement of oxygen diffusion rates with the platinum microelectrode: correlation of plant response to soil oxygen diffusion rate” Hilgardia, Berkeley, vol. 35, no. 20, pp. 567-576, 1964, DOI:10.3733/hilg.v35n20p545

[14] J. Glinski, “Soil aeration and its role for plants”. Boca Raton: CRC Press, pp. 237, 1985. doi.org/10.1201/9781351076685

[15] W. H. Patrick and R. D. Delaune, “Characterization of the oxidized and reduced zones in flooded soil”. Soil Science Society of America, Proceedings, Madison, vo. 36, pp. 573-576, 1972 DOI:10.2136/sssaj1972.03615995003600040024x

[16] American society of agricultural engineers, ASAE r. 313.1, St. Joseph, MI, Agricultural Engineers Yearbook of Standards, 2p, 1978.

[17] A.G. Bengough. “Penetrometer Resistance Equation. Its Derivation and the Effect of Soil Adhesion” J. Agric. Engng Res. vol. 53, pp. 163-168, 1992.

[18] D. A. Farrel and E. L. Greacen. “Resistance to penetration of fine probes in compressible soil”. Australina Journal of Soil Research. vol. 4, pp. 1-17, 1966

[19] L. M. Rabello and P. E. Cruvinel, “Modeling for automated microprobe dedicated to measuring soil resistance to root penetration”. In: Brazilian congress of soil science, 29, 2003, Ribeirão Preto. Soil: foundation of production systems. Ribeirão Preto: UNESP, 2003. 4 f. 1 CD-ROM.

Earth-Satelite Monitoring System for Storaged Grains

Jose Dalton Cruz Pessoa
Embrapa Instrumentação
São Carlos, Brasil
email: jose.pessoa@embrapa.br

Ladislau Marcelino Rabello
Embrapa Instrumentação
São Carlos, Brasil
email: ladislau.rabello@embrapa.br

Victor Bertucci Neto
Embrapa Instrumentação
São Carlos, Brasil
email: victor.bertucci@embrapa.br

Sérgio da Silva Soares
CRIAR Space Systems
Ribeirão Preto, Brasil
email: sergio@grupocriar.com.br

***Abstract*— Despite Brazil being the fifth country in the world in area and population, it is the largest in terms of cultivated land area, becoming a global player related to food production and exportation in the last decades. At the same time, food production increases year by year as do infrastructure problems. One of the crucial problems is related to grain storage. The availability of grain storage now is lower than the total of grain produced, leading producers to promptly sell production that could not be stored. Some companies sell to farmers solutions like silo bags, or plastic bags, as a fast way to overcome this kind of problem. Grains stored in silos are susceptible to insect infestation and fungal growth, depending on initial conditions and storage conditions, which can lead to the loss of part or even the entire stock. The statistics are unclear or do not exist, but it is estimated that technology can reduce losses from 40-50% to 1-2%. This project proposes monitoring post-harvest variables to detect or even forecast potential risks to the quality of the stored product. This solution requires data transmission in areas that lack cellular network coverage. To overcome this limitation and offer a robust solution, the team chose to use a satellite to communicate between two ground stations: one that sends the measured data and the other close to the data center to receive and process the data. This demand was embraced by the company CRIAR Space Systems which is, together with Embrapa, working on solutions such as installing silo bags, monitoring physical and chemical variables in those silos to automatically produce alert signals. These signals can indicate the presence of contamination in the silos due to local fermentation, or due to the presence of high/low bulk moisture and temperature, for instance. Another CRIAR feature is the development of communication antennas for satellite signals with the purpose of further launching a private satellite dedicated to monitoring all farms covered by this service. The scope of this work in progress is to show how this is being planned and applied.**

Keywords – silo; antenna; grain; soy; corn; forage.

I. INTRODUCTION

The Brazilian Institute of Geography and Statistics (IBGE) [1] registered 47,578 farms with more than 1,000 hectares in Brazil. Part of these farms is located in the Center-West Region, composed of states with vast areas: Mato Grosso, Mato Grosso do Sul, Goiás (1,612,000 km²) and Tocantins (277,621 km2). These states are the main producers of soybeans and corn.

According to Agência Nacional de Telecomunicações (ANATEL) [2] data from December 2023, 8% of Brazil's territorial area still does not have mobile phone coverage, or 850,000 km2. This area includes remote regions, rural areas, roads, and highways. This data indicates that 12% of the rural population does not have access to cell phones. The data, however, does not specify the quality of the mobile service provided: stability, reliability, and availability [1].

Grain storage units are established in rural areas, close to producing properties. Conventional warehouses, inflatable warehouses, bulk warehouses, silos and silo bags have structural and functional characteristics that differentiate themselves, but they are all intended for storing large volumes, especially of grains.

Oxygen makes up 21% of the air, and at 2%, corn begins anaerobic respiration. Up to this limit, the seed absorbs O2 from the silo environment and releases CO2 in a ratio of 3:1. A silo with a diameter of 2.5 m and a length of 60 m has approximately 294.5 m3. If filled with corn at a density of 750 kg/m3 and 10% dead volume (occupied by air), the silo will contain 220,875 kg of corn and 29.5 m3 of air. According to the ISA [3], the density of air at 15°C at sea level is 1225 kg/m3. As the molar mass of air is approximately 28.9 g/mol, 1 m3 of air contains 42.2 mol of air. Considering the percentage (21%) of Oxygen (O), that volume contains 8.8 mol of O2, that is 284.15 gO2. Under the storage conditions described above, the dead volume of the silo would contain 261.96 molO2 or 8.38 kgO2.

The respiratory rate of corn is quite elastic, between 0.5 and 2.0 mgO2/kg.h. Considering a value of 1 mgO2/kg.h, the corn load would consume 220,875 mgO2/h (220.8 gO2/h). If the temperature was kept constant and the oxygen consumption was independent of the concentration, the time for the load to consume 98% of the available O2 (considering the simplifications of the model) would be

ISBN: 978-1-68558-164-0

approximately 37 days. After this time, the grains would begin anaerobic respiration.

This model is very simple because it does not consider the sidereal day or environmental parameter values, but it provides a rough estimate for time.

The objective of this work is to reduce the risk of damage to stored grains, considering that different storage environments have characteristics that increase different types of risk.

In silos exposed to the environment, the intergranular temperature and the relative humidity of the air inside the silo are two basic observable variables of the internal ecosystem of the silo, but they are insufficient to detect signs of deterioration in the quality of the stored grains. Several authors have sought to identify monitoring variables that could serve as indicators of grain quality [4][5][6]. In practice, however, increasing the number of sensors also increases the cost of monitoring.

One of the working hypotheses of this project is that specific variables must be added to the intragranular temperature and the relative humidity of the air inside the silo according to the characteristics of the stored product. Taher et al. [7] provides some relevant information for the development of sensors and their distribution in silos.

Monitoring storage systems would be an alternative to reduce the risk of most types of accidents. In this approach, sensors would measure the 'monitoring variables' whose signals would be processed and sent to the manager of the warehouse.

Figure 1 illustrates a probe that encapsulates one or more sensor elements with their respective electronics, one electronic for signal pre-processing and another responsible for the sensor's communication with a receiving base.

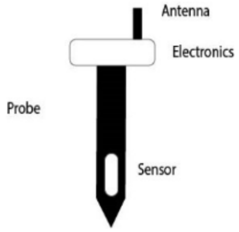

Figure 1. Probe schematic. The probe is composed of sensors, conditioning electronics, and antenna.

The probe's sensors monitor post-harvest variables to detect changes in grain quality. In their review, Bartosik et al. [6] investigate the following factors affecting grain quality within silo-bag storage systems:

Environmental Influences: Temperature, CO2, O2, and humidity levels; Temperature Fluctuations: The impact of temperature cycles on moisture migration and subsequent grain quality losses; Mycotoxin Formation: The underlying mechanisms of mycotoxin contamination; Insect Infestation: The incidence, dynamics, and impact of insect presence on grain quality. When choosing sensors, authors like Danao et al. [10] prioritize experimental objectives and cost, with cost becoming a major consideration for commercial products."

The modified atmosphere within silo-bags, with CO2 concentrations ranging from 3 to 25% and O2 concentrations from 10 to 25%, plays a crucial role in inhibiting insect presence and mold development (Bartosik, 2011)

The extension of the storage unit demands a number of sensors proportional to its size, each one sending data periodically to a data center, where it will be used to identify the type of sensor, its location, and measured values. In isolated areas, this configuration requires the solution of problems related to the power supply of the electronics, the integrity of the data packets, and the robustness of the communication.

Figure 2 illustrates the positioning of probes like the one in Figure 1 at different points of the storage unit (e.g. silo-bags) forming a network of sensors classified by type, geolocation, and organized in a database.

Figure 2. Ground communication network is formed by probes installed in the silos, a hub (data concentrator) coupled to a ground station that transmits the signal to the satellite

The probes communicate data over a wireless network to a data concentrator unit that may or may not be near an antenna. The LoRa (Long Rangejlcp) and LoRaWAN (Long Range Wide Area Network) technologies from Semtech Corporation were chosen for terrestrial communication because they offer advantages such as low power consumption (20mA) and long range (up to 15 km) [8] [9].

One alternative for accessing data from a storage unit in a remote area is satellite communication. This approach enables silo load monitoring even in areas with no cellular coverage or poor signal quality.

The data concentrator unit may or may not contain an antenna forming a ground station for signal conditioning, antenna positioning, and transmission to a low-orbit satellite. The satellite would amplify the signal and retransmit it to another ground station that would send it to a database and then to the interested parties.

The uplink and downlink communication tasks are critical to the satellite performance solution and the most susceptible to failure. Other critical points of the project include the operational quality of the antenna, its mechanical robustness and the precision of its positioning mechanisms, the dynamic positioning of the satellite and its robustness considering space conditions, the correct sizing of the electronic systems architecture and the synchronization of the communication elements to ensure that all data is properly delivered to the ground station.

This section introduced the main concepts of the project and its motivation. Section II (Working on Solutions) will present the development of ground communication solutions, contextualizing them for the project. Section III concludes the paper.

II. WORKING ON SOLUTIONS

Figure 3 presents the solution architecture for terrestrial grain monitoring. Here, the signal flows unidirectionally from the probes to the target user.

The probes contain sensor elements for measuring CO2, O2, temperature, and humidity, along with signal conditioning electronics, a battery, and a radio. The number of probes installed in the storage unit depends on the volume to be monitored and the storage conditions. The first three columns of Figure 3 represent these probes. Each probe periodically wakes up, reads the sensors, and transmits the data using a LoRa radio.

The Earth Station receives radio signals through a dedicated receiver. It comprises a radio antenna, signal conditioning and temporary storage electronics, a satellite antenna positioning system, and equipment for transmitting (uplink) data to the satellite via VHF or UHF bands. All sensing and communication elements must be encapsulated in IP65 standard for protection against atmospheric conditions and dust.

A Low Earth Orbit (LEO) satellite captures the Earth station signal. Monitoring satellites typically operate in LEO, between 200 and 2000 km from Earth's surface. This orbit offers advantages like higher revisit frequency over a particular location and lower communication latency. The satellite must receive the signal, amplify it, and retransmit it back (downlink) to the second ground station.

At the second Earth Station the data will be received and sent via the internet to the database and then to the target user. The user will receive the data in a format appropriate to their needs.

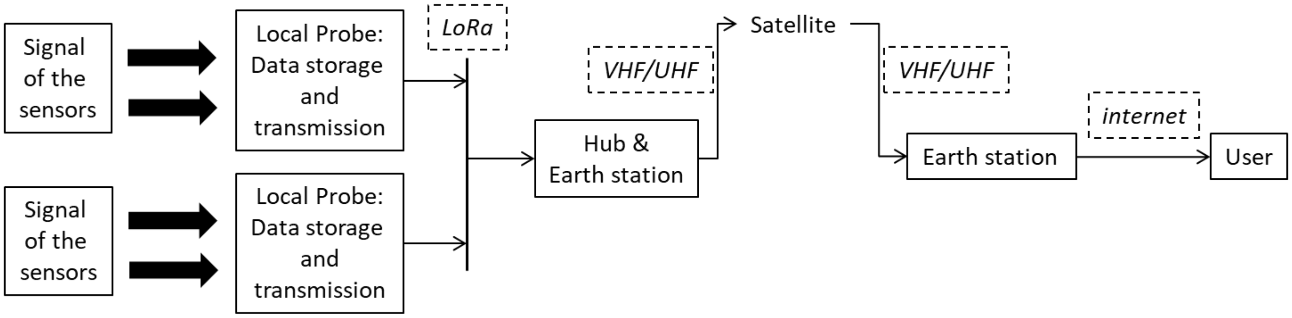

Figure 3. Data obtained by the probes are sent by radio to a first Earth Station, which then transmits it to the satellite. After amplification, the signal is retransmitted to a second Earth station and to the silo manager.

A. Sensing and ground communication

CRIAR Space Systems manufactures its own measurement devices from commercial transducers. The process includes the development of the signal conditioner and calibration.

Periodically, the probes send the reading packet of a given moment in time to a data concentrator located in a suitable location that can be several kilometers away. In general, the communication protocol (named JLCP) developed in the project includes the following general characteristics:

- The message is divided into packets.
- For each packet sent by a transmitter, a confirmation from the receiver is awaited.
- Only after confirmation does the transmitter discard the sent piece and move on to the next.
- If the receiver does not respond with a confirmation within the period defined in the timeout parameter, the transmitter performs a new send.
- After exceeding the maximum number of send attempts, both the transmitter and the receiver understand that there was a connection error, and the session is terminated.
- Data integrity is guaranteed by enabling and verifying the Cyclic Redundancy Check (CRC), which is a part of the LoRa Frame dedicated to verifying the integrity of the sent bits.
- The completeness of the packet is verified by attempting to parse the received string to a Java JsonArray object and the completeness of the message is guaranteed by a final packet check.
- The redundancy of received packets (generated by a delay in the delivery of packet copies in the middle of the distribution) is solved by means of route locking, which guarantees that the fastest route is maintained from the beginning to the end of a session, and by means of the sequential packet reception filter.
- Payload encryption is not part of the protocol itself, and it is up to the two ends to encrypt the packets and share

keys. This decision was made because block encryption algorithms significantly increase the content size.

The terrestrial communication architecture and its implementation including the communication protocol between the probe and the collector will be evaluated on two aspects: Data loss with respect to distance is shown in Figure 4. Figure 5 shows data loss for packets of 3 and 255 bytes transmitted over 3134 meters.

The tested system was capable of processing 3-byte and 255-byte data packets over distances of up to 3134 m, with a TX power of 18 db.

On the time line, the first event was a test of distance (Figure 4).

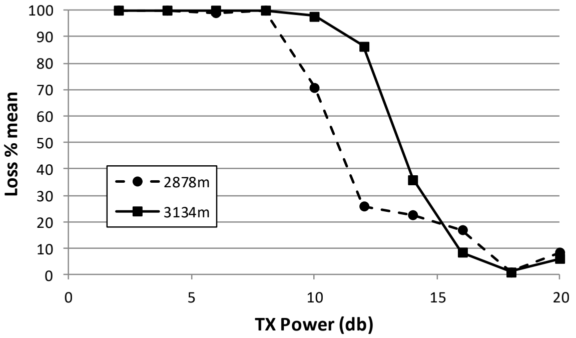

Figure 4. Payload mean loss at 2,878 meters and 3,134 meters transmission distances with different radio transmission powers

A 3-byte data packet was transmitted over different distances and radio power levels. Figure 4 shows the mean information loss across the two longest tested distances. The Figure also indicates that at a transmission power of 18 dB, there is minimal signal loss.

Following improvements, a second test was conducted to evaluate the transmission of 3-byte and 255-byte data packets over a distance of 3134 meters at various transmission powers.

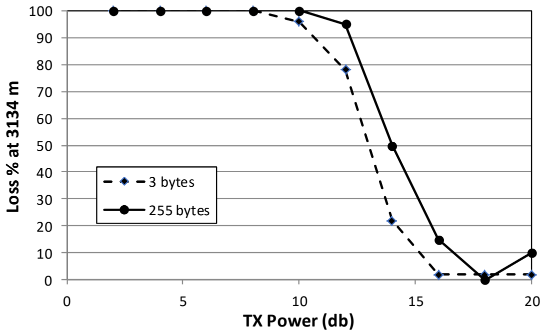

Figure 5. Percentage Packet Loss (3-Byte and 255-Byte Packets) over a 3134-Meter Transmission at Varying Radio Transmit Powers

Figure 5 shows that the minimal signal loss for a 3-byte payload was 16 dB, while the minimal loss for a 255-byte payload was 18 dB.

III. CONCLUSIONS

Under suitable conditions, it is expected that in a silo-bag, corn can be stored for up to 24 months. During this time, Oxygen will be consumed, and the grains will maintain ~~a~~ low metabolism. In inadequate humidity conditions, the cargo can be infested by fungi and bacteria, and after the consumption of oxygen the fermentation process will begin.

A 60 m and 2.5 m diameter silo can store 220 tons of corn, which at the current price corresponds to a capital stock of approximately USD 47,000. To avoid partial or total loss of cargo, the proposed alternative is cargo monitoring. The proposed solution, suitable even for remote areas, is data transmission via satellite, which includes a terrestrial transmission stage, the uplink, the downlink and another terrestrial stage.

The team is working on the low-orbit satellite design and the development of the terrestrial transmission system, which allowed the transmission of sensor measurements over a distance of more than 3 km, but it is expected to double or triple this range.

The project faces several technical challenges, including limitations of the power source, sensor and electronics robustness, and data integrity. This paper presents the latest developments in Earth Station instrumentation, specifically focusing on sensor technology and data transmission. However, the most significant challenge lies in the business aspects, where maintaining an attractive final product price is crucial.

ACKNOWLEDGMENT

The authors would like to acknowledge the support of the CRIAR group, especially CRIAR Space Systems, and Embrapa, which provided the resources to carry out this work up to the current stage.

REFERENCES

[1] IBGE, <https://www.ibge.gov.br/estatisticas/economicas/agricultura-e-pecuaria/21814-2017-censo-agropecuario.html?=&t=series-historicas>, [retrieve: may, 2024].

[2] ANATEL, <https://www.gov.br/ ANATEL/pt-br>, [retrieve: may, 2024].

[3] ISA. <https://skybrary.aero/articles/international-standard-atmosphere-isa>, [retrieve: may, 2024].

[4] P. C. Coradi, É. Lutz, N. dos S. Bilhalva, L. B. A. jaques, M. M. Leal, and L. P. R. Teodoro, Prototype wireless sensor network and internet of things platform for real-time monitoring of intergranular equilibrium moisture content and predict the quality corn stored in silos bags. Espert Systems with applications 208, 118242, 2022.

[5] W. R. Balsani, Development of intelligent instrumentation architecture for monitoring agricultural silos. Dissertação EESC/USP, 1999.

[6] R. Bartosik, H. Urcola, L. Cardoso, G. Maciel, and P. Busato, Silo-bag system for storage of grains, seeds and by-products: a review and sesearch agenda. Journal of Stored Products Research 100, 10206, 2023.

[7] H. I. Taher, H. A. Urcola, C. G. Cendoya, and R. E. Bartosik, Predicting soybean losses using carbon dioxide monitoring during storage in silo bags. Journal of Stored Produts Research 82, pp.1-8, 2019.

[8] M. F. L. Pereira and P. E. Cruvinel, Development of a LoRa wireless sensor network to estimate agicultural risk, in Proceedings of the 1t International Conference on Advances inSensors, Actuators, Metering and Sensing (ALLSENSORS'21), Nice, France, 18 to 21 Jul 2021 pp. 35-42, 2021.

[9] M. F. Lima Pereira, P. E. Cruvinel, G. M. Alves and J. M. G. Beraldo, "Parallel Computational Structure and Semantics for Soil Quality Analysis Based on LoRa and Apache Spark," 2020 IEEE 14th International Conference on Semantic Computing (ICSC), San Diego, CA, USA, 2020, pp. 332-336, doi: 10.1109/ICSC.2020.00066.

[10] M. C. Danao, R. S. Zandonadi, and R. S. Gates. Development of a grain monitoring probe to measure temperature, relative humidity, carbon dioxide levels and logistical information during handling and transportation of soybeans. Computers and Electronics in Agriculture 119 pp.74-82, 2015.

Real-time Detection and Reconfiguration of Sensors in Agricultural Sprayers Subject to Failures

Deniver R. Schutz*,†,Vilma A. Oliveira†, Paulo E. Cruvinel*

*Embrapa Instrumentation
Brazilian Agricultural Research Corporation, São Carlos, SP, Brazil
† Department of Electrical and Computer Engineering
São Carlos School of Engineering
University of São Paulo, São Carlos, SP, Brazil
Email: deniver@usp.br, voliveira@usp.br, paulo.cruvinel@embrapa.br

***Abstract*—The application of pesticides in agriculture is crucial to increase food production and pest control. However, improper application results in high costs and environmental and human health risks. Currently, the importance of innovations in technologies to improve reliability in agricultural spraying systems is recognized. This paper presents a real-time strategy for faults analyzing, when using a flow sensor during the operation of an agricultural sprayer. Additionally, a method sensor-based for reconfiguring the control loop using the fluidic resistance and pressure data is proposed. Results demonstrate the effectiveness of this arraignment considering an additional pressure sensor in the sprayer system to ensure reliability, i.e., even when the flowmeter fail. Besides, based on such strategy the agricultural spraying process is not interrupted.**

***Keywords*-Sensors in agriculture; reability; real-time processing; agricultural sprayers; support decision-making.**

I. INTRODUCTION

In general, pesticide spray application by agricultural sprayers is realized at a constant rate (l/ha), regardless of the density of pests and diseases, compromising application efficiency [1]. On the other hand, the application of pesticides using Variable Rate Application (VRA) takes into account the spatial variation of pests and its on the crop. With the assistance of data from prescription maps, sensors, and actuators, the VRA system adjusts the quantity of pesticides in liters per hectare in real time, controlling the flow rate and pressure [2].

Controlling the flow and the pressure in an agricultural sprayer system is important for several reason. A precise flow application allows to reduce the production costs, as it ensure that the correct amount in applied in the crop, while efficient pressure control aids in the quality of application. In other words, the correct flow and pressure control and the accuracy in the spray rate help to minimize loss and optimize the use of resources [3]. Therefore, it is essential to ensure proper functioning of the instrument responsible for monitoring the flow and the pressurre of the syrup (mixture of the quimical active component plus water). Any failure in these components can result in the improper application of pesticides, increasing the risk of contamination in neighboring areas and loss of product due to over-application or under-application [4]. In fact, it is crucial to prevent faults during the timing window in agricultural processes.

A fault is defined as a departure from an acceptable range of an observed variable or a calculated parameter associated with a process. Additionally, a fault can be considered as an abnormality process or symptom, such as deviations like too high pressure or even a high flow into a hydraulic system [5] [6].

Currently, the detection of abnormal events or malfunctions in agricultural machinery relies mainly on the presence of the operator. However, due to increased workload and the growing complexity in machinery, supervising these failures have become to be challenges. This can lead to operations with uncertain data, resulting in inadequate control and operations far from ideal. Therefore, an evolution in techniques and technologies for automatic fault detection and diagnosis have been required [5].

Modern agriculture sprayers use flow and pressure sensors to monitor the spray bar, allowing precision application of pesticides and other chemicals. However, there are challenges in finding note only a flow sensor but also a pressure sensor that can withstand high vibration,useful life wear, disturbance in weather and harsh chemicals, without breaking the bank to address the needs of agriculture applications. In such a context an alternative should be considered either a flow or pressure sensor fail during agricultural operation. In fact, both sensors may fail to meet required levels of flow and pressure ratings or do not have whetted materials and electrical connection options needed for agricultural applications. Of coarse, helpfully there still have some options in the market, like for instance the use of the pressure sensors E2G™ and KM15™ from Ashcroft® and the VKP-063 from Velki® and the use of flow sensors FM600-250 from BELIMO® and DN50 IP from Impac® company.

Besides, recent works have been developed to create fault-tolerant systems in hydraulic componets. In [7], is presented method for analyzing the reliability and failure of agricultural sprayers using smart sensors, a microcontroller, and a controller area network protocol. This system helps in ensuring the correct rate of pesticide application for pest control, reducing measurement errors, and minimizing the impact on the environment. Likewise, Bayesian convolutional neural networks are employed in [8] to predict the lifespan of solenoid valves,

Copyright (c) IARIA, 2024. ISBN: 978-1-68558-164-0

enhancing system reliability. In [9], an active Sensor-Fault-Tolerant Controller (SFTC) is proposed for an independent metering control system, capable of tolerating faults in input, output, and feed pressure sensors using analytic redundancy. A real-time fault diagnostic method for hydraulic systems is proposed by [10] using data from multiple sensors. It introduces a Multi-Sensor Convolutional Neural Network (MS-CNN) that incorporates feature extraction, sensor selection, and fault diagnosis into an end-to-end model.

This research work aims to develop a real-time strategy for detecting faults in the flow sensor and reconfiguring the closed-loop control system using a pressure sensor to ensure sprayer operation continuity in case of eventual failures.

In this document, after this introduction, Section II shows constituent components of the spraying module of the Agricultural Sprayer Development System (SPDA), a method for the identification of the fluidic resistance K_t, and the method for fault evaluation. Sections III and IV present discussions of the results based on both with simulation by MatLab® and real data with the SPDA, respectively. Finally, the conclusion is presented in Section V.

II. DETECTION AND RECONFIGURATION STRATEGY

The block diagram of the spraying system is presented in Figure 1, with the Fuzzy Generalized Predictive Controller (Fuzzy GPC), developed by [11] [12], used to regulate the system flow rate.

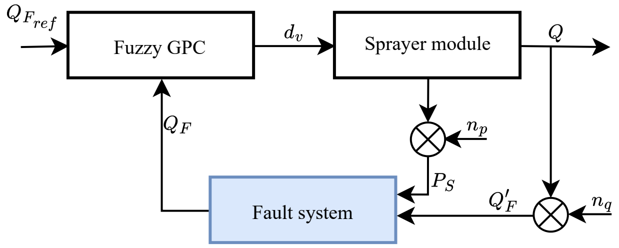

Figure 1. Block diagram of the arraignment for fault evaluation and reconfiguration system.

In Figure 1, n_p and n_q represent noises inserted in the same sequence as the signals P_S and Q'_F, with the objective of simulating reading signals closer to reality and are determined by:

$$\begin{aligned} n_q &= Q'_F \cdot 0.05 \cdot rand \\ n_p &= P_S \cdot 0.05 \cdot rand \end{aligned} \tag{1}$$

with *rand* used to generate random numbers from a continuous uniform distribution in the range [0, 1].

A. Failure assessment

The assessment of possible failure occurs by comparing the Root Mean Square Error (RMSE) index with a threshold l_f defined by the designer through a priori knowledge. If the RMSE deviation exceeds this threshold, the system identifies the occurrence of a failure. RMSE is the standard deviation of the residuals. It is a measure of the magnitude of the distance between two points. The calculation of RMSE is given by:

$$RMSE = \sqrt{(Q_{PS} - Q'_F)^2} \tag{2}$$

where Q'_F is the reading value of the flowmeter and Q_{PS} is the estimated flow valuated considering the pressure P_S and the fluidic resistance K_t:

$$Q_{PS} = \sqrt{\frac{P_S}{K_t}}. \tag{3}$$

Algorithm 1 evaluates the flow signal Q'_F from the flowmeter and adjusts the closed-loop if a fail is detected. In this case, the control variable becomes to be estimated by the flow Q_{PS}, derived from the pressure sensor signal P_S.

Algorithm 1 Evaluation of failure

```
Input: Reading from the pressure sensor ($P_S$), reading from the flowmeter ($Q'_F$), fault threshold defined by the designer ($l_f$).
Output: Flow ($Q_F$)
Initialize
$Q_{PS} \leftarrow \sqrt{\frac{P_S}{K_t}}$   (3)
$RMSE \leftarrow \sqrt{(Q_{PS} - Q'_F)^2}$   (2)
$Q_F \leftarrow Q'_F$
if $RMSE > l_f$ then
    Failure alarm for the operator.
    $Q_F \leftarrow Q_{PS}$;
end if
Return:$Q_F$
```

B. K_t identification

The hydraulic relationship for the spraying system operating under turbulent flow regime is given by:

$$\Delta P_S = Q^2 \; K_t \tag{4}$$

where K_t, P_S, and Q are, respectively, the fluid resistance, the pressure, and the flow of the spraying system. Therefore, by understanding the fluid resistance, it has become feasible to estimate the flow of the system through pressure readings, also in both directions [13].

To find the fluid resistance, an open-loop experiment was conducted on the SPDA using 2 bars with 7 MagnoJet® M063/1 CH06 nozzles on each bar. Starting from an initial condition, with the valve V_{P1} fully open ($\theta_{vp} = 0$) and with a PWM signal duty cycle $d_v = 0$ for 2 seconds, $d_v = 70$ is applied for 7 seconds, closing the return of Valve V_{P1}. Then, $d_v = 0$ is applied for 7 seconds, keeping it stationary. Finally, $d_v = -100$ is applied for 7 seconds, opening the return of V_{P1}. The results are presented in Figure 2. K_t was obtained using (4).

Based on Figure 2, one can observe that at average operating point of the proportional valve $\theta_{vp} = 80$ rad [14], the fluid resistance behaves linearly, thus it can be approximated to an average value of $K_t = 0.41$. In the highlighted segments from

0 to 6.3 s and from 21 to 22 s, since the flow was null the fluid resistances were indeterminate.

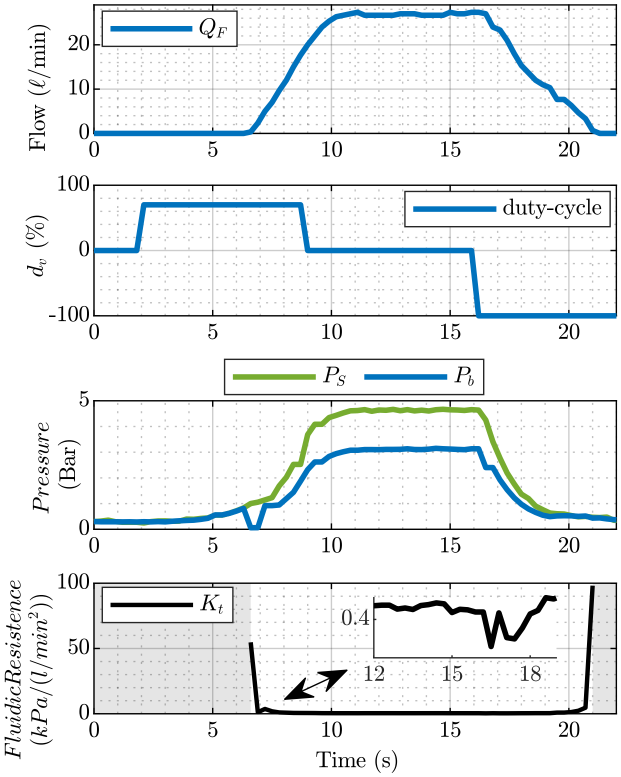

Figure 2. Open-loop experiment for obtaining the fluid resistance K_t.

III. SIMULATION RESULTS

The results were obtained with the sprayer module described in Figure 3 which, together with the actuator, was responsible for regulating the syrup application rate via liquid flow control [12] [11].

A three-phase motor, driven by a three-phase inverter, maintained a constant flow rate of the piston-type spraying pump model MB-42 Jacto®. Its purpose was to draw water from a 300 l reservoir to act as a diluent, sending it to a hydraulic system, which pumping the syrup to the nozzles bar.

A three-way proportional valve denoted as V_{P1} of the needle type, model 463022S from ARAG®, was the main actuator of the system to regulate the syrup flow. It had the capacity to control flow rates of up to 150 l/min with a maximum pressure of 2000 kPa and a response time of 7 s. Its piston is actuated by a direct current motor, coupled to an H-bridge used to control the piston position ($0 \leq \theta_{vp} \leq 94.2\,\text{rad}$) and the rotation direction (valve opening or closing) through PWM signals. Automatic return solenoid valves, denoted as V_{S1} and V_{S2} are used to direct the flow to the nozzles bars [14].

The flow rate of the solution was measured by an electromagnetic flowmeter (model 4621AA30000, ORION® company), with a measurement range between 5 to 100 l/min, capable of withstanding pressures of up to 40 bar. Two piezoelectric pressure sensors, model A-10 from WICA®, was coupled to the system; one monitors the pressure of the distribution bar and the other monitors the pressure at the end of nozzles bar. At the end of the section bars, five-way nozzle holders (model QJS, Teejet®) were attached, responsible for forming the spray droplets [15].

For simulation it has been used the MatLab® software to control a proportional valve V_{P1} in a spraying module. The procedure follows the same operating condition as the open-loop experiment presented in Section II-B. The model parameters of the spraying plant and the tuning gains of the Fuzzy GPC are defined in [11], as presented in Table I.

TABLE I
PARAMETERS OF SPRAYER MODULE [11], [14].

Parameter	Value
a_1 (V_{P1} resistance curve parameter)	2.8110^{-6}
β (V_{P1} resistance curve parameter)	6.53
K_M (Motor gain)	1.10 rad/V
T_M (Motor time constant)	5.0010^{-2}
K_{pH} (H-Bridge gain)	0.12
τ_F (pesticide transportation delay)	0.6 s
Q_B (Sprayer pump flow)	40 l/min
K_T (Fluidic resistence with CH06)	0.41 kPa/(l/min)^2
m (Number of spray bars with nozzles)	2
n (Number of nozzles per bar.)	7
λ_0 (Fuzzy GPC control gain)	1
δ_0 (Fuzzy GPC reference gain)	5
l_f (Fuzzy GPC reference gain)	1

For the simulation procedure, it is considered the following conditions:

1) The pressure sensor is operational and it is not subject to failures.
2) The sensor fail occurs at the intermediate operating point of the system, when its fluid resistance can be represented by an average value.

In the first simulation test, a total loss fault of the flowmeter signal was introduced, while in the second simulation test, random gain faults were added using the $rand$ function of MatLab®. Both faults were implemented between the intervals of 105 and 183 s. The results are observed in Figures 4 and 5, respectively.

Analyzing the results, it was observed that despite the flowmeter failures, the system successfully detected them and reconfigured itself in a closed-loop fashion using the pressure sensor. The change between sensors during the operation, after the observed fail, occurred without significative signal losses, leading to a robust operation.

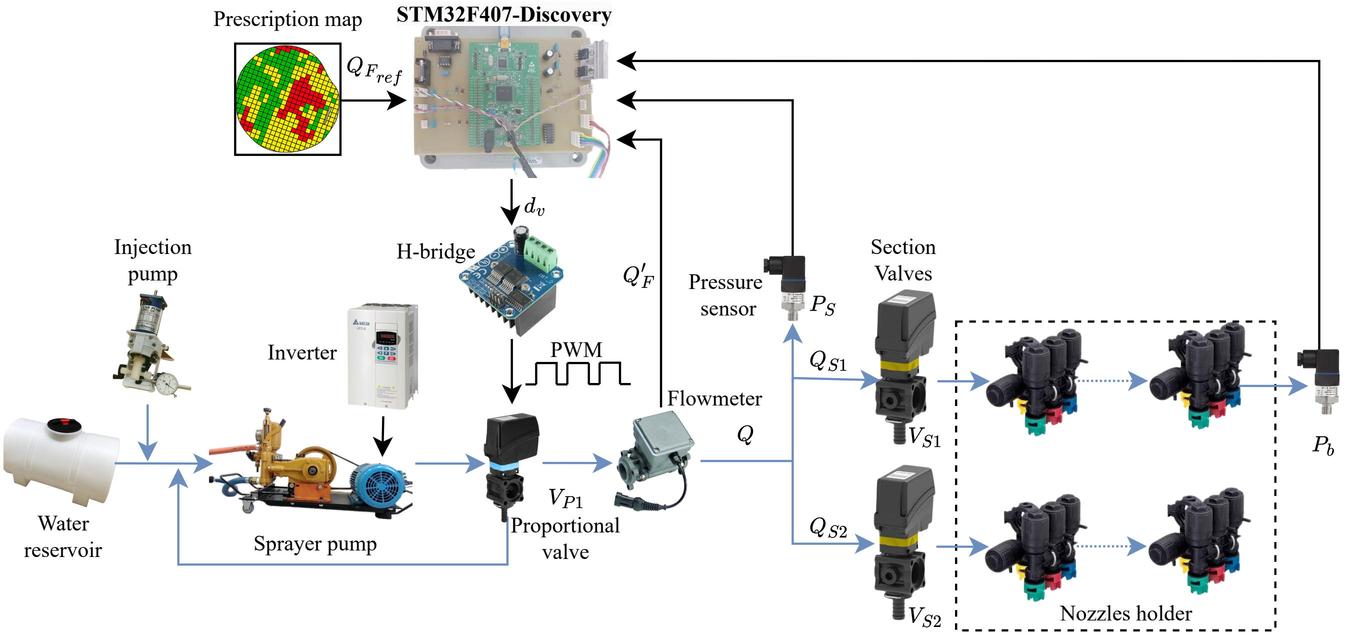

Figure 3. Sprayer module diagram of SPDA.

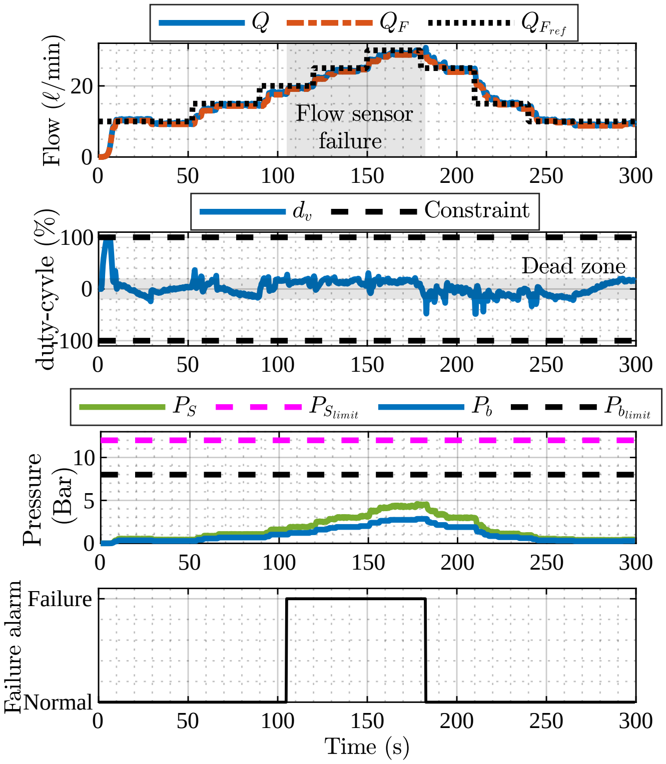

Figure 4. Simulation for total loss of flowmeter signal.

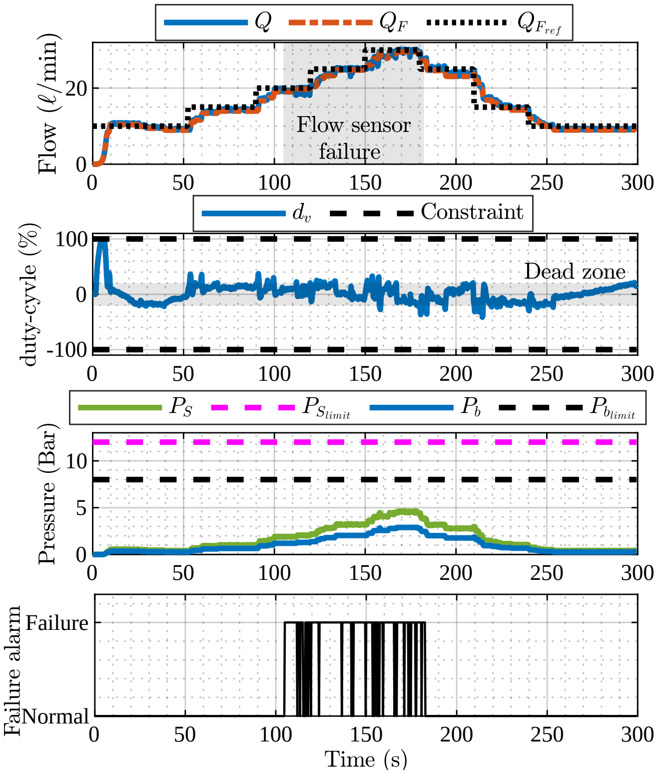

Figure 5. Simulation for gain failure in the flowmeter signal.

IV. EXPERIMENTAL RESULTS

The fuzzy GPC described in [11] and the fault analysis and reconfiguration system were embedded using a STM32F407-Discovery and the C# language.

To maintain plant safety, reference values were used to avoid pressure spikes above 8 and 12 bar, respectively int the spray tip bar and the spray bar (P_b and P_s). Two spray bars were used, each of then having 7 M063/1 CH06 nozzles spaced at a distance of 50 cm. Besides, it was used a working speed equal to 10 km/h and a constant spray pump flow rate equal to 40 l/min. Figure 6 presents the result of the control system when a total failure occurred in the flowmeter signal between 99s and 163s.

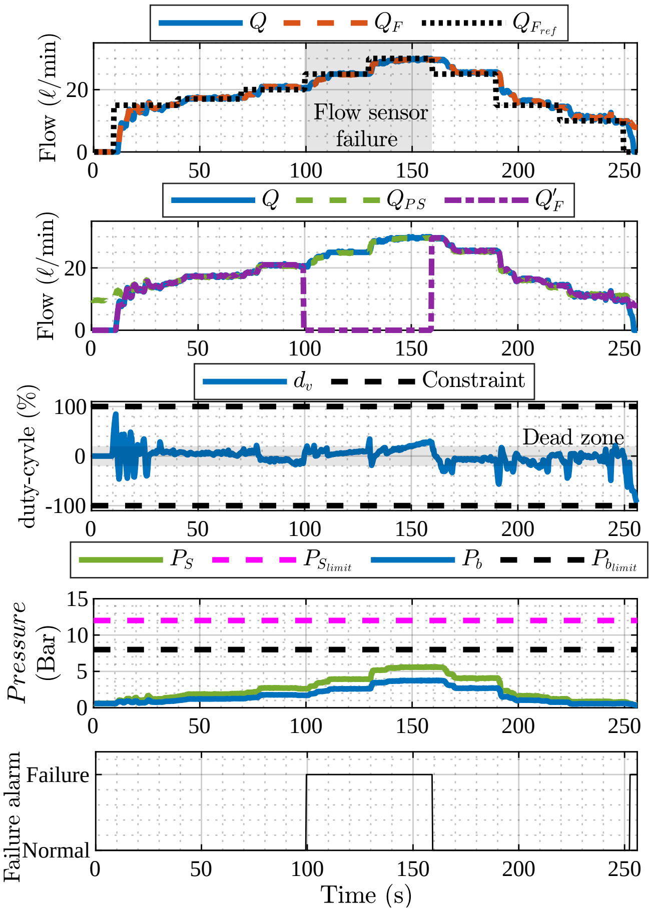

Figure 6. Flow responses of the sprayer operating with M063/1 CH06 nozzle for a stair reference.

The results confirm the opportunity to exchange the sensors during the operation, which improved reliability, as well as the practical and experimental effectiveness of using fuzzy GPC control in conjunction with the analysis and reconfiguration system for flow control. By understanding the fluid resistance at the average operating point of the proportional valve V_{P1}, it is feasible to identify the fault, communicate it to the operator and reconfigure the control loop using the pressure sensor.

It is noticeable in Figure 6 that at points where the flow reaches zero, corresponding to when the return of proportional valve is fully open, the estimated flow Q_{Ps} was great than zero, indicating a false positive fault. This occurs due to the fact that the pressure sensor model A-10 from Wika® presents a deviation in its signal when occurred absence of flow.

V. CONCLUSION

In this work, a sensors based-method was shown to aggregate value and robustness to agriculture sprayers. The opportunity to exchange sensors in agriculture sprayer during the operation showed reliability improvement. Results obtained by simulations were confirm using real data considering variations in flow and pressure in a sprayer bar.

The use of fluidic resistance has proven promising in the control loop reconfiguration strategy through pressure sensor, preventing interruptions in the spraying process caused by flowmeter failures. Additionally, the utilization of the STM32F407 Discovery has been found to be ideal for embedded implementation.

As a perspective for future work, it is being consider methods for obtaining fluidic resistance in real time, as well as the development a new sensor to evaluate the impact of residual error on the estimation of average fluidic resistance.

ACKNOWLEDGMENTS

This research was supported by the Brazilian Agricultural Research Corporation (Embrapa Instrumentação, under grant SEG, Process 11.14.09.001.05.06.001 Development of advanced automated models, tools and instruments for precision agricultural spraying), the National Counsel of Technological and Scientific Development (CNPq, under grant 88887.703189/2022-00) and São Paulo Research Foundation (FAPESP, under grant 2023/06759-0).

REFERENCES

[1] J. Campos, M. Gallart, J. Llop, P. Ortega, R. Salcedo, and E. Gil, "On-farm evaluation of prescription map-based variable rate application of pesticides in vineyards," *Agronomy*, vol. 10, no. 1, pp. 1–22, 2020.

[2] E.-C. Oerke, R. Gerhards, G. Menz, and R. A. Sikora, *Precision crop protection-the challenge and use of heterogeneity*. Boon: Springer, 2010, vol. 5.

[3] M. Grella et al., "Field assessment of a pulse width modulation (pwm) spray system applying different spray volumes: duty cycle and forward speed effects on vines spray coverage," *Precision Agriculture*, vol. 23, no. 1, pp. 219–252, 2022.

[4] E. A. Straw, E. Kelly, and D. A. Stanley, "Self-reported assessment of compliance with pesticide rules," *Ecotoxicology and Environmental Safety*, vol. 254, no. 114692, p. 15, 2023.

[5] G. Craessaerts, J. De Baerdemaeker, and W. Saeys, "Fault diagnostic systems for agricultural machinery," *Biosystems Engineering*, vol. 106, no. 1, pp. 26–36, 2010.

[6] Q. Zhong, E. Xu, Y. Shi, T. Jia, Y. Ren, H. Yang, and Y. Li, "Fault diagnosis of the hydraulic valve using a novel semi-supervised learning method based on multi-sensor information fusion," *Mechanical Systems and Signal Processing*, vol. 189, no. 110093, pp. 1–19, 2023.

[7] P. E. Cruvinel, H. V. Mercaldi, P. B. Andrade, and E. A. Penãloza, "Real-time evaluation of failure and reliability in agricultural sprayers using embedded sensors and controller area bus protocol," *International Journal on Advances in Systems and Measurements*, vol. 13, pp. 161–174, 2020.

[8] G. Mazaev, G. Crevecoeur, and S. Van Hoecke, "Bayesian convolutional neural networks for remaining useful life prognostics of solenoid valves with uncertainty estimations," *IEEE Transactions on Industrial Informatics*, vol. 17, no. 12, pp. 8418–8428, 2021.

[9] R. Ding, M. Cheng, S. Zheng, and B. Xu, “Sensor-fault-tolerant operation for the independent metering control system,” *IEEE/ASME Transactions on Mechatronics*, vol. 26, no. 5, pp. 2558–2569, 2020.

[10] H. Tao, P. Jia, X. Wang, and L. Wang, “Real-time fault diagnosis for hydraulic system based on multi-sensor convolutional neural network,” *Sensors*, vol. 24, no. 2, pp. 353–374, 2024.

[11] D. R. Schutz, H. V. Mercaldi, E. A. Peñaloza, L. J. Silva, V. A. Oliveira, and P. E. Cruvinel, “Advanced embedded generalized predictive controller based on fuzzy gain scheduling for agricultural sprayers with dead zone nonlinearities,” *Journal of Process Control*, vol. 135, no. 103164, pp. 1–11, 2024.

[12] D. R. Schutz, H. V. Mercaldi, E. A. Penaloza, V. A. Oliveira, and P. E. Cruvinel, “An intelligent fuzzy-GPC control for agricultural sprayers: comparison between GPC and PID fuzzy controllers,” In: 15th APCA International Conference on Automatic Control and Soft Computing, July 6-8, 2022, Caparica, Portugal. Springer, 2022, pp. 272–284.

[13] R. F. Magossi, E. A. Peñaloza, S. P. Battachharya, V. A. Oliveira, and P. E. Cruvinel, “Emulating a sensor for the measurements of the hydraulic resistances of nozzles in agricultural sprayers based on the use of the point-wise thévenin’s theorem,” *International Journal on Advances in Systems and Measurements*, vol. 10, no. 3-4, pp. 184–193, 2017.

[14] K. R. Felizardo, H. V. Mercaldi, P. E. Cruvinel, V. A. Oliveira, and B. L. Steward, “Modeling and model validation of a chemical injection sprayer system,” *Applied Engineering in Agriculture*, vol. 32, no. 3, pp. 285–297, 2016.

[15] D. R. Schutz, E. A. Penaloza, H. Mercaldi, V. A. Oliveira, and P. E. Cruvinel, “A model based intelligent sensor to control sprinklers in spray actions.” In: ALLSENSORS 2023: The Eighth International Conference on Advances in Sensors, Actuators, Metering and Sensing, 2023, pp. 16–20.

Development of Urine Monitoring Sensor Module with Wireless Transmission Function

Lan Zhang, Jian Lu, Sohei Matsumoto
Device Technology Research Institute
National Institute of Advanced Industrial Science and Technology (AIST)
Tsukuba, Japan
emails: {chou-ran, jian-lu, sohei.matsumoto}@aist.go.jp

Abstract— **In modern society, there is an increasing focus on health monitoring, particularly in terms of urine detection for newborns and the elderly. While some researchers have developed local urine testing systems, a comprehensive urine monitoring system is still lacking. We have developed an ultrathin urine sensor electrode with a smart measurement and transmission system for health monitoring. The urine monitoring sensor system is extremely compact and features a user-friendly interface, ensuring a positive user experience. The measurement results demonstrate that the sensor, which utilizes multi-channel electrodes, has the potential to measure urination time and pattern. We believe that the practical application of urine sensors will benefit a wide range of individuals.**

Keywords- Urine monitoring; multi-channel electrodes; health condition; user interface; wireless transmission.

I. INTRODUCTION

With the increasingly serious challenges presented by an aging society, highly effective and low-cost health detection technology for both the elderly and newborns has become a significant research focus [1][2]. As researchers in the development of smart sensors, it is imperative to contribute efforts to address the aforementioned societal issues positively. We have developed a rapid manufacturing platform for fabricating the sensing electrodes, allowing the production of flexible, thin urine monitoring sensors on uneven surfaces through non-contact injection technology [3]. However, the complexity and high cost of this fabrication method restrict its large-scale application.

The sensor electrode manufacturing process described in this study adopts the direct printed electrode method, which is highly suitable for relatively flat surfaces and significantly reduces costs, thereby expanding its potential usability. In this study, we aim to discuss the extension applications of the given sensor in health monitoring fields. The composition of the sensor measurement and transmission system is introduced. Preliminary evaluations of the sensor system with multi-channel electrodes are also presented. Figure 1 shows the schematic view of our proposed urine sensor measurement system and its potential applications. The sensor system integrates the sensing and wireless transmission system (see Figure 1(a)) with an electrode array (see Figure 1(b)). Additionally, the authors have developed a User-friendly Interface (UI) application on the terminal tablet. The proposed UI (see Figure 1(c)) can display a line graph for each sensor electrode output value in the array, and a matrix diagram can also be presented for easy observation. The potential applications of the provided urine sensor are introduced, where the compact sensing system unit can be affixed to a nappy or a diaper, enabling real-time monitoring of the health conditions of children or elderly individuals. The ultra-small, low-power wireless sensor node can also be placed on a mat to measure the urine condition of pets. In Section 2, we will outline the characteristics of the sensor electrodes and system. Section 3 will present some preliminary measurement results. Lastly, in Section 4, the conclusion will be provided.

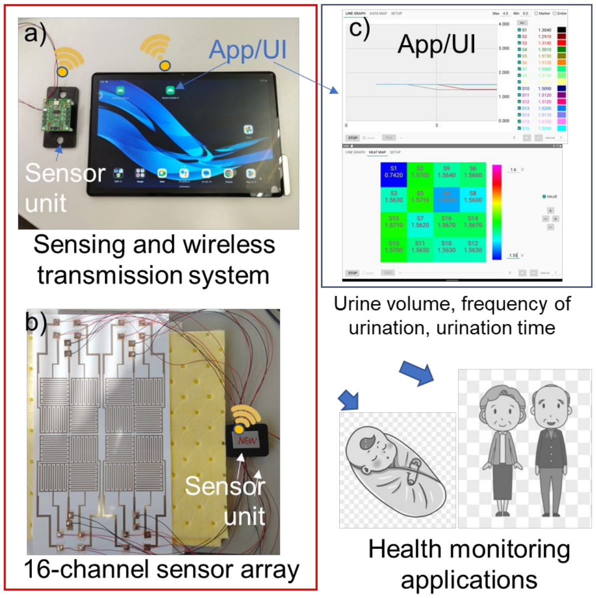

Figure 1. Wireless urine sensor system and its potential applications. (a and b) show the hardware of the sensor system, while (c) illustrates the software of the user interface.

II. SENSOR FABRICATION AND SPECIFICATION

We developed a rapid manufacturing platform for creating urine sensor electrodes [3]. This platform facilitated the production of flexible, thin urine detection sensors on uneven surfaces. However, the fabrication complexity and high cost of this process limited its large-scale application. In this study, we adopted a direct printing method on the substrate, offering the benefits of low-cost and high-efficiency fabrication. Using an inkjet printer (PX-S160T, Epson Ltd.), the conductive solution was directly printed on photo paper to form the sensor electrodes with the desired pattern. Once the sensor electrodes and extension circuits were generated, a laminate film was coated to protect the electrode surfaces, ensuring a long lifetime and resistance to scratches and other damages. Furthermore, we designed and manufactured testing circuits and a measurement board specifically for the fabricated sensor electrodes. Resulting the given sensor can detect urine time and pattern for the measured objects.

III. PRELIMINARY MEASUREMENT RESULTS

A. Functional evaluation and measurement of the fabricated sensor electrode

The urine volume change diffusion experiment was conducted on the urine sensor with a 2×2 electrodes array. A certain amount of solution was dropped in the middle or at the edge of the electrodes array, and the sensor array accurately detected the spread diffusion of urine volume changes. To assess the operational quality of the sensor, long-term stability is a crucial factor. The authors evaluated the long-term stability of the fabricated sensor electrodes over several weeks, and the results indicated that the sensor could work continuously for 5 weeks, maintaining a stable output baseline and responsivity.

B. Evaluation of sensor system with 16-channel electrodes and wireless transmission functions

A preliminary measurement for the performance evaluation of the proposed urine sensor system was conducted in a controlled environment. The experiment took place in a draft chamber with a temperature of 25°C and a relative humidity of 50%RH. The measurement system was placed in the chamber without any changes to the testing environment. Figure 2 shows the results of the evaluation of the sensor system with 16-channel electrodes and wireless transmission functions. As depicted in Figure 2(a), all channels consistently output voltage signals and maintain a stable baseline. Figure 2(b) shows the voltage output of the sensor electrodes under loading. In the first phase, 16 sensor electrodes were positioned under an absorbent mat, resulting in an output of approximately 1.30V. In the second phase, an equivalent solution was applied to the mat above each of the 16 electrodes. The results demonstrate that sensor electrodes from No. 1 to No. 16, respectively detect changes in solution volume, maintaining stable output voltage. The experiment verifies the detection performance and output stability of the fabricated sensor system.

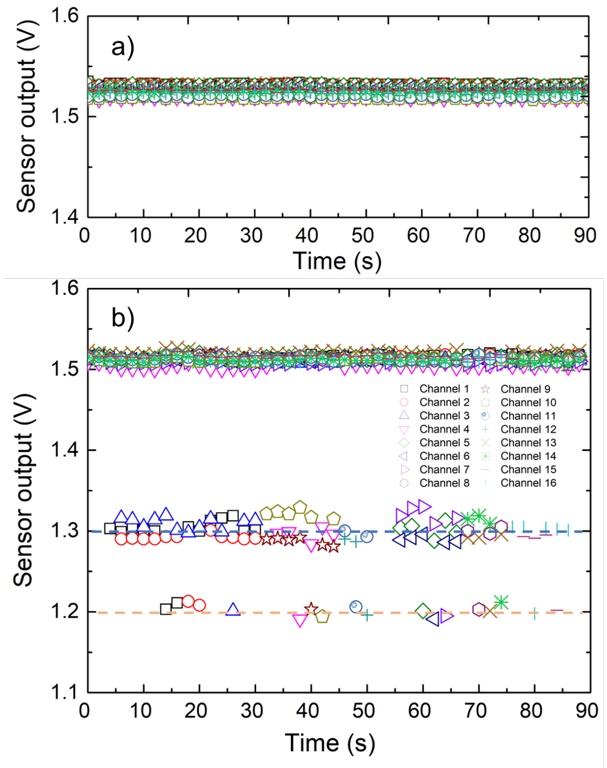

Figure 2. Sensor output of the measurement system with 16-channel electrodes and wireless transmission functions. (a) shows the output voltage with a stable baseline, while (b) shows the output of the sensor electrodes under loading.

IV. DISCUSSION AND CONCLUSION

We have developed an ultrathin urine sensor electrode with a smart measurement and transmission system for health monitoring. The urine monitoring sensor system is super compact in size, featuring a user-friendly interface to ensure a positive user experience. The measured results demonstrate that the urine sensor, equipped with multi-channel electrodes, can real-time monitoring the urination time and pattern properly.

ACKNOWLEDGMENT

This research work was supported by New Generation Medical Treatment and Diagnosis Research Laboratory, National Institute of Advanced Industrial Science and Technology (AIST).

REFERENCES

[1] E. Suganthi and L. Ashmiya, “Human Health Monitoring Using Wearable Sensor,” Sens. Rev., vol. 28, pp. 364-376, 2018.

[2] M. Cheng et al., “A Review of Flexible Force Sensors for Human Health Monitoring,” J. Adv. Res., vol. 26, pp. 53-68, 2020.

[3] L. Zhang, J. Lu, E. Takashi, and S. Matsumoto, “Rapid Manufacturing Approach of an Ultrathin Moisture Sensor for Health Monitoring,” Sensors, vol. 23, pp. e-1-12, 2023.

Investigation of Thermo-formed Piezoelectret Accelerometer under Different Electrodynamic Vibration Conditions

Igor Nazareno Soares
Department of Electrical and Computer Engineering
Engineering School of São Carlos, University of São Paulo
São Carlos, Brazil
igor.soares@usp.br

Ruy Alberto Corrêa Altafim
Department of Electrical and Computer Engineering
Engineering School of São Carlos, University of São Paulo
São Carlos, Brazil
altafim@usp.br

Ruy Alberto Pisani Altafim
Department of Computer Systems
Informatics Center, Federal University of Paraíba
João Pessoa, Brazil
ruy@ci.ufpb.br

Mario Masahiro Tokoro
Energy Infrastructure Laboratory
Institute of Technological Research
São Paulo, Brazil
tokoro@ipt.br

***Abstract*—Accelerometers are essential sensors utilized across various industry applications. They enable precise measurement of acceleration, tilt, and motion, facilitating advancements in fields, such as biomechanics, healthcare monitoring, automotive safety, and consumer electronics. With their versatile functionality, accelerometers play a crucial role in enhancing human safety, improving performance, and driving innovation in modern technology. The demand for new accelerometer technologies led to the use of piezoelectrets as the main sensing element. Piezoelectrets are advanced materials with unique structure and properties, similar to piezoelectric polymers but with enhanced performance due to their cellular microstructure. With promising applications in energy harvesting, sensing, biomedical devices, and acoustics, their remarkable efficiency and flexibility make them particularly appealing for compact and versatile transducers and actuators. Due to their abilities, piezoelectrets have been employed in the development of accelerometers for monitoring electrodynamic vibrations. Different designs have been proposed and, in this paper, the concept of an enclosed seismic mass superposing a sensing element is used together with an open tubular channel thermo-formed piezoelectret. The recently enhanced piezoelectret accelerometer, only analyzed in a custom-made workbench, is tested in this paper in a standard electrodynamic vibration setup at frequencies ranging from 50 Hz up to 1 kHz. The results from both custom-made and standard systems are presented for a much better understanding of this type of accelerometer.**

***Index Terms*—Accelerometers, piezoelectrets, functional materials, piezoelectricity, mechanical vibration.**

I. INTRODUCTION

In the realm of modern science and technology, the role of accelerometers has become increasingly significant across a diverse range of fields, owing to their exceptional capabilities in measuring and analyzing acceleration forces. Accelerometers, as electromechanical devices, are designed to detect and quantify changes in velocity, acceleration, and orientation in various contexts, thereby serving as pivotal instruments in scientific research, industrial applications, healthcare systems, consumer electronics, and beyond [1].

The relevance of accelerometers stems from their fundamental ability to capture and interpret motion dynamics with precision and accuracy. Originally developed for aerospace and military applications, accelerometers have undergone remarkable advancements, leading to their ubiquitous integration into everyday devices, such as smartphones, wearables, and automotive systems [2]. This widespread adoption underscores their indispensable role in enhancing human experiences and improving the efficiency and safety of numerous technologies [3].

One of the primary areas where accelerometers have revolutionized research and innovation is in the field of biomechanics and sports science. By capturing intricate movement patterns and biomechanical parameters during physical activities, accelerometers enable researchers and practitioners to gain profound insights into human performance, injury prevention, rehabilitation strategies, and sports equipment design. Moreover, accelerometers play a crucial role in the development of wearable health-monitoring devices, facilitating real-time tracking of physical activity levels, sleep patterns, and overall well-being, thereby empowering individuals to make informed decisions about their health and lifestyle choices [4].

Furthermore, accelerometers find extensive applications in automotive engineering and transportation systems, where they contribute to vehicle stability control, inertial navigation, crash detection, and driver assistance systems [2]. By precisely measuring acceleration and tilt angles, accelerometers enable the implementation of advanced safety features, such as airbag deployment algorithms, rollover detection mechanisms, and adaptive cruise control systems, thereby enhancing road safety and reducing the risk of accidents.

ISBN: 978-1-68558-164-0

In addition to their utility in conventional industries, accelerometers are also instrumental in emerging fields, such as robotics, Virtual Reality (VR), and Augmented Reality (AR). By providing real-time feedback on motion and orientation, accelerometers enable robots to navigate complex environments, manipulate objects with precision, and interact seamlessly with humans. Similarly, in VR and AR applications, accelerometers facilitate immersive user experiences by accurately tracking head movements and gestures, thereby enhancing the realism and interactivity of virtual environments [5].

In summary, accelerometers represent a cornerstone technology with profound implications for scientific research, industrial innovation, and consumer electronics. As the demand for enhanced motion sensing capabilities continues to grow across various domains, the ongoing advancements in accelerometer technology are poised to drive further progress and unlock new possibilities in the realms of science, engineering, and beyond. One of these technologies that pushes accelerometers to further possibilities is based on piezoelectrets.

Piezoelectrets are a class of advanced materials that have garnered significant attention in scientific research and technological innovation. These materials, akin to piezoelectric polymers, exhibit piezoelectric properties, yet are distinguished by their cellular microstructure and enhanced performance characteristics. Leveraging their unique structure-property relationships, piezoelectrets offer promising prospects for diverse applications ranging from energy harvesting and sensing to biomedical devices and acoustics [6]. The remarkable electromechanical coupling efficiency and flexibility inherent in piezoelectrets render them particularly appealing for developing compact, lightweight, and versatile transducers and actuators.

Because of these abilities, in this research, open-tubular channel thermo-formed piezoelectrets were employed as sensing elements for an accelerometer investigated in different electrodynamic vibration conditions, which range from 50 Hz up to 1 kHz. The accelerometer employed here is considered an improvement of a previous design and until now it has not been tested with standard equipment. In this paper, we demonstrate how the improvements can affect its performance and how it can be employed in further electrodynamic vibration experiments.

The rest of the paper is structured as follows. In Section II, we present a theoretical explanation of how accelerometers operate as well as their composition. In Section III, we present the state of the art related to the piezoelectret accelerometer. Section IV explains how the accelerometer presented in this work differs from previously presented open-tubular channel thermo-formed piezoelectrets and how the measurements were performed. In addition, a comparison between two electrodynamic vibration systems using this thermo-formed accelerometer is presented. In Section V, a comparison between two electrodynamic vibration systems using this thermo-formed accelerometer is presented. Further, a possible explanation for the observed effect is given. In Section VI, we conclude with a synthesis of this work, the major flaws, and the advantages of the proposed accelerometer, as well as how it performed in the two different systems.

II. ACCELEROMETERS

To comprehend the operational principles of the accelerometer made with a thermo-formed piezoelectret, it is essential to elucidate the construction process of accelerometers. Accelerometers operate based on the principles of inertial sensing, specifically by measuring changes in acceleration experienced by a mass within the device. The basic operation of an accelerometer involves the following components and processes:

Mass: At the core of an accelerometer is a mass, typically referred to as a proof mass, which is suspended within the device. This mass is designed to move in response to changes in acceleration.

Sensing Mechanism: Surrounding the proof mass, there are typically one or more sensing elements. These sensing elements can vary based on the type of accelerometer, but common types include piezoelectric, piezoresistive, capacitive, or electromagnetic sensors.

Reference Frame: Accelerometers are typically fixed within a reference frame, such as the Earth's gravitational field. When the accelerometer experiences acceleration in a different direction relative to this reference frame, the proof mass and sensing elements experience forces that cause them to move or deform.

Measurement of Displacement or Deformation: As the proof mass moves or deforms in response to acceleration, the sensing elements detect this motion. For example, in a capacitive accelerometer, the displacement of the proof mass alters the capacitance between electrodes, while in a piezoelectric accelerometer, the deformation generates an electric charge.

Conversion to Output Signal: The detected motion or deformation is converted into an electrical signal by the sensing elements. This signal typically corresponds to the magnitude and direction of the acceleration experienced by the accelerometer.

Signal Processing and Output: The electrical signal is processed by electronics within the accelerometer to filter noise, amplify the signal if necessary, and convert it into a usable output format. This output can be in the form of voltage, current, frequency, or digital data, depending on the specific design of the accelerometer.

By measuring the changes in acceleration, accelerometers can provide valuable information about the motion, orientation, and vibration of objects or systems in various applications, ranging from automotive safety systems and consumer electronics to industrial monitoring and aerospace engineering [3].

III. PIEZOELECTRET ACCELEROMETERS

Accelerometers made with piezoelectrets or ferroelectrets have been reported previously in the literature as a promising device for a growing demand [7], [8]. In the context of these investigations, seismic masses were positioned atop piezoelectret films and secured using springs affixed to the accelerometer frame. Nonetheless, according to [7], spring-based designs proved unwieldy, cumbersome, and lacking in hermetic sealing. An alternative methodology was introduced within this research, entailing the attachment of a seismic mass directly onto the piezoelectret surface, foregoing additional housing. This streamlined configuration was heralded as a more sophisticated solution; however, the authors underscored the utilization of supplementary static force to fortify the structural integrity of the accelerometer.

Drawing upon the aforementioned accelerometer concept, a hermetically sealed design, as depicted in Figure 1, was introduced in [9] using piezoelectrets with an open-tubular channel structure. The illustration additionally shows the frequency response of the device within the range of 1 Hz to 1 kHz. This accelerometer was fabricated with a freestanding mass above the sensor and the noise response observed in the frequency range is significant due to this design configuration.

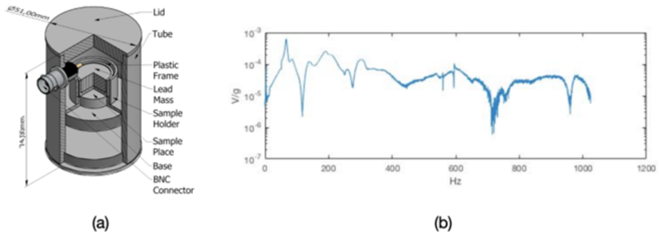

Fig. 1. (a) Schematic design of the piezoelectret accelerometer hermetically sealed. (b) Frequency response up to 1 kHz (as published [9]).

In pursuit of achieving a more consistent frequency response with this accelerometer configuration, enhancements have been implemented, based on a spring system [10]. The so-called evolution of the thermo-formed piezoelectret accelerometer, was tested in a custom-made electrodynamic vibration system, without any further standard characterization. Here, the performance of this accelerometer was verified on both systems, i.e. with a standard equipment setup and with the custom-made platform.

IV. EXPERIMENTAL DETAILS

This section outlines the thermo-formed piezoelectret accelerometer's construction, its difference from previous models, as well as the methodology and experimental setup employed to investigate and characterize it.

A. *Thermo-formed Piezoelectret Accelerometer (TFPA)*

The Thermo-Formed Piezoelectret Accelerometer (TFPA) presented in this study is shown in Figure 2, where (a) depicts a real photo of the device hermetic housing, (b) represents a schematic view of the accelerometer construction and (c) provides a front view of the thermo-formed piezoelectret prepared with open-tubular channels. The improved accelerometer design for a single detection axis is composed of a 30 g cylindrical lead seismic mass, with dimensions of 10 mm in height and 18 mm in diameter, enclosed within a polytetrafluoroethylene (PTFE) sheath placed over a thermo-formed piezoelectret (sensor). An elastic component made of polyurethane foam with a density of 12 kg/m^3 is placed on top of the mass to provide mechanical support and restitution, while an aluminum guide vertically guides the mass. The employment of the foam on the top of the mass is considered a major advance, since it differs from the previously presented springs and should provide a noise reduction in the analyzed frequency range. To ensure mechanical resistance and electrical shielding, the transducer is connected to an Bayonet Neill-Concelman (BNC) connector and is enclosed in a cylindrical aluminum case measuring 74 mm in height and 51 mm in diameter.

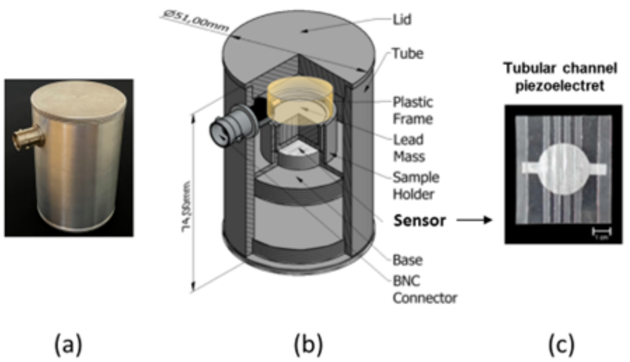

Fig. 2. (a) Photo of the TFPA prototype. (b) Exploded view of the TFPA internal structure. (c) Piezoelectret sensor, prepared with open tubular channels.

The thermo-formed piezoelectret was fabricated according to the lamination process described by Altafim et al. in [11], which provided a piezoelectret with four open-tubular channels with 1.5 mm width and an active area of 254.47 mm^2. The use of this particular piezoelectret was chosen due to the experience of the authors in fabricating such devices, the possibility to modulate its resonance frequencies with the variation of the geometric factors of the open-channels, the better temperature stability of the Teflon® fluoroethylenepropylene (FEP) in comparison with traditional employed polypropylene (PP), and previous understanding of the electromechanical behavior of this type of piezoelectret.

B. *Electrodynamic vibration setup*

The TFPA's frequency response, spanning from 50 Hz to 1 kHz, underwent meticulous characterization using the experimental setup delineated in Figure 3. This setup comprised an HP model 33120A function generator, calibrated to delineate the desired frequency spectrum. This generator interfaced with a robust Power Amplifier, from Brüel & Kjær (B&K) model 2707, tasked with a driving B&K shaker, model 4812, to induce controlled vibrations. Positioned atop this shaker, both a reference accelerometer (B&K model 8305) and the TFPA were affixed. The reference accelerometer's output was routed through a B&K conditioning amplifier Type 2635 while the TFPA was connected directly without further amplifications.

Simultaneously, the signals from both the accelerometer and the TFPA were captured using an oscilloscope (DSO-X 3024A model from Agilent Technologies), ensuring precise data synchronization and accuracy throughout the experimental procedure. It is important to mention that the shaker was calibrated with the reference accelerometer to drive a sinusoidal force of 9.81 N/mm^2.

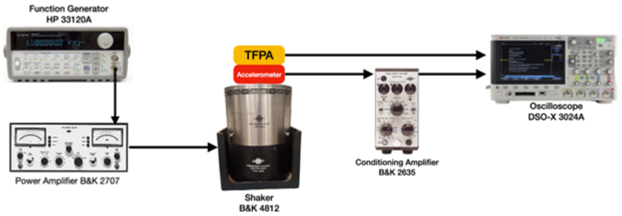

Fig. 3. Block diagram of the experimental setup set to monitor the frequency response of the TFPA.

The second electrodynamic vibration system consisted of a custom-made shaker constructed using a 15.24 cm (6 inch) diameter mid-bass speaker from Foxer Alto-falantes®, equipped with a ferrite magnet and an aluminum single coil, with 4 Ω impedance, 80 W power, frequency response ranging from 30 Hz to 30 kHz, and sensitivity of 90 dB/W. An acrylic holder with a PTFE guide was fabricated to support the TFPA. Calibration of this platform was performed with an ADXL327 accelerometer from Analog Devices, with an acceleration input range of ±2g, sensitivity of 420 mV/g and frequency response from 0.5 Hz to 1600 Hz, connected to an Arduino UNO® microcontroller board. A function generator from Tektronix (model AFG3022CA) was employed with driven signals and a Taramps TL-500 Class D Amplifier was used for the output signal amplification.

V. RESULTS AND DISCUSSIONS

The standard setup was previously calibrated with the reference accelerometer frequencies ranging from 50 Hz up to 3.2 kHz. The electrical signals captured by the oscilloscope are depicted in Figure 4, from which it is evident that the reference accelerometer exhibits a consistent linear sensitivity of approximately 314 mV/g across the entire frequency spectrum under evaluation. In contrast, the TFPA displays signals characterized by lower amplitudes and a distinct resonance peak at 100 Hz. Upon comparison with previously presented results from an accelerometer lacking polyurethane foam in Figure 1(b), it becomes apparent that the new configuration of the TFPA yields a significant reduction in the signal noise level. Additionally, the resonance phenomenon around 100 Hz is more pronounced. However, it is notable that the sensor's sensitivity experiences a strong decline at frequencies exceeding 300 Hz.

The output signal from the custom-made vibrating platform is presented in Figure 5 in comparison with the one obtained in the standard vibrating system. As can be seen, the clear resonance peak is also present in this setup, although a reduction in the accelerometer amplitude of approximately 44 mV/g is observed. It was also noticed that in this experiment, the sensitivity of the TFPA was kept reasonably constant around 30 mV/g, and the resonance peak was shifted to a higher frequency, i.e., 250 Hz.

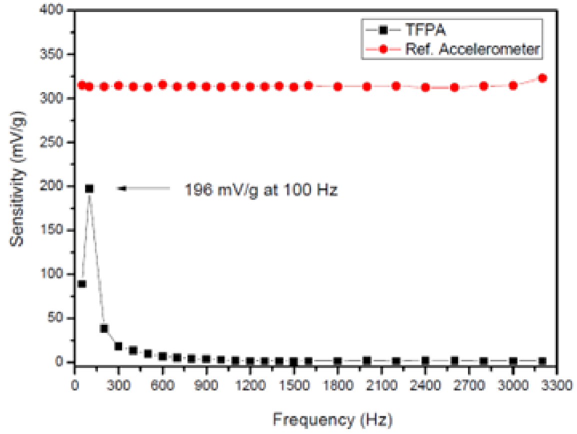

Fig. 4. Frequency response of the TFPA, with a resonance frequency at 100 Hz.

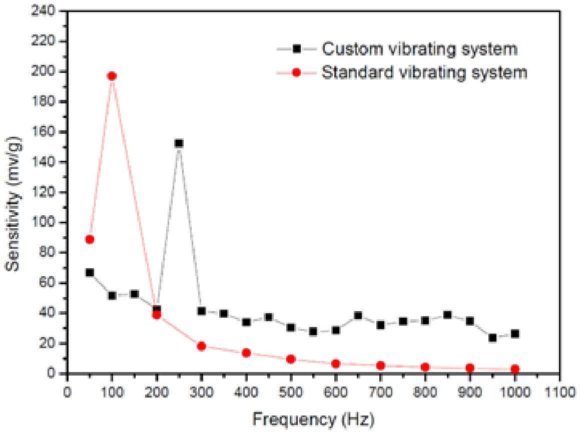

Fig. 5. Frequency response of the TFPA, investigated in the custom-made platform and with the standard setup, both results indicating a clear visible resonance.

Dynamic measurements performed on the same type of thermo-formed piezoelectrets for a frequency range from 2 Hz up to 60 Hz was reported in [12]. In such a study, a static force (16.9 kPa) was applied to the sensor superimposed with a sinusoidal stimulation of 5.6 kPa. From these, a linear response was observed over the entire frequency spectrum. The referenced work also investigated the sensor electrical response under different static forces, and it was demonstrated that with the increase of the static pressure, the piezoelectric response can be reduced by more than 80% (e.g. 30 kPa) compared to its value recorded at 10 kPa. In that work, this drastic reduction was attributed to the increase in the elastic modulus of the sample, therefore for higher effects a much lower static or dynamic force should be employed.

These reported experiments are similar in many ways to

ISBN: 978-1-68558-164-0

the TFPA characterization presented here. For instance, the previous static force was replaced here by a constant weight (lead mass) on the piezoelectret sensor while the previous superimposed sinusoidal force is pretty much the same regarding amplitude values. Now, considering that a 30 g weight was representing a static pressure of 1.157 kPa, it would be expected that the TFPA presented a high electrical response, however the superimposed dynamic pressure was calculated as being 38 kPa, which is higher than the 30 kPa, where the sensor loses more than 80% of it electromechanical response, thus explaining why the TFPA had such a low electrical response.

Nevertheless, in order to verify the relation between the inertial mass and the accelerometer sensitivity, masses with different weights, referenced here as M1, M2, were also employed in the electrodynamic vibration experiment. M1 with 6 g and M2 with 24 g, represented equivalent pressures of 0.231 kPa and 0.925 kPa, respectively. The results from this experiment, in the custom-made platform, are presented in Figure 6, where it can be noticed that the amplitude of the TFPA sensitivity varied according to inertial mass i.e. for M1, a sensitivity of approximately 11 mV/g was obtained, while with M2, this value was approximately 68 mV/g.

According to [13], depending on the piezoelectret design, an optimum sensitivity may be obtained when exposed to pressures below 1 kPa, meaning that the electromechanical response of these devices suffers an increasing effect with the increased pressure before it starts to drastically decrease. Thus, a similar behavior is observed here, where the accelerometer with M2 expected an optimum configuration.

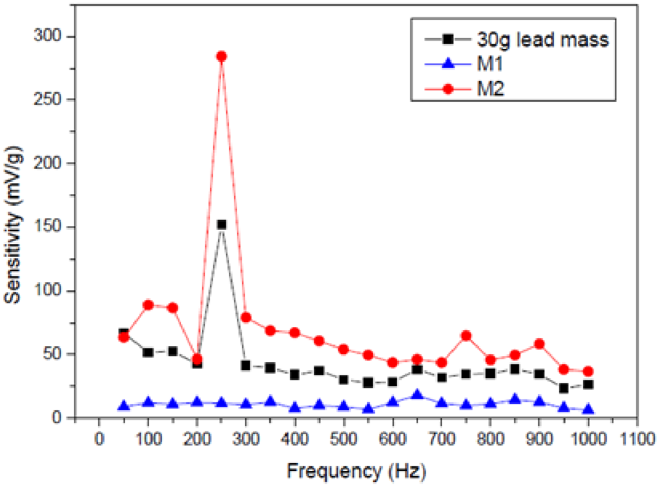

Fig. 6. Frequency response of the TFPA with different lead masses.

Regarding the resonance peaks, at 100 Hz and 250 Hz at the standard setup and the custom-made system, and the similarity of these experiments, one can understand that these resonances result from the electrodynamic vibration systems and not from the accelerometer. For reference, the resonance observed at 250 Hz was already reported during the characterization of the custom-made system in [10].

VI. CONCLUSION AND FUTURE WORK

In this study, an accelerometer utilizing thermo-formed piezoelectrets and implementing further enhancements was fabricated and subjected for testing under two different electrodynamic vibration conditions. The experimental setups, employed standard equipment, covered frequencies ranging from 50 Hz to 3.2 kHz and a custom-made system, which supported frequencies ranging from 50 Hz up to 1 kHz. Due to the last setup limitations, results were compared until 1 kHz. Our findings revealed a prominent resonance frequency at 100 Hz, with peak sensitivity reaching 196 mV/g, in the standard setup, and a resonance at 250 Hz with a peak sensitivity of 152 mV/g in the custom-made system. Beyond these resonances, the accelerometer maintained its signal response stable up to 1.0 kHz, albeit diminished amplitudes of 4.2 mV/g and 43 mV/g in the standard setup and the custom-made, respectively. The difference in sensitivity was attributed to a variation in the static load from both systems, which was further confirmed by changes in the lead mass of the accelerometer. The shift in the resonance peak was concluded to have originated from the mechanical vibrating systems. Further, the enhancements implemented in this accelerometer configuration mitigated the noise observed in prior iterations of similar piezoelectret accelerometers. This underscores the suitability of thermo-formed piezoelectret sensors for accelerometer applications, with the inclusion of a spring system proving advantageous in minimizing undesired mechanical vibrations. Building upon these results, a new design is currently being developed featuring reduced dimensions, addressing a concern echoed by other researchers in the field.

ACKNOWLEDGMENT

The authors thank the Brazilian funding agencies CAPES and CNPq, the University of São Paulo (Electrical and Computer Department at Engineering School of São Carlos), the Federal University of Paraíba, and the Institute of Technological Research of São Paulo (Energy Infrastructure Laboratory).

REFERENCES

[1] E. S. Barbin, T. G. Nesterenko, A. N. Koleda, E. V. Shesterikov, I. V. Kulinich and A. Kokolov, ”Concept for Manufacturing a Microoptoelectromechanical Micro-G Accelerometer,” in: IEEE International Siberian Conference on Control and Communications (SIBCON), Tomsk, Russian Federation, on November 17 – 19, pp. 1-5, 2022. https://doi.org/10.1109/SIBCON56144.2022.10002971

[2] W. Patrick, ”Review: Fifty Years Plus of Accelerometer History for Shock and Vibration (1940–1996),” Shock and Vibration, vol. 6, pp. 197-207, 1999. https://doi.org/10.1155/1999/281718.

[3] G. Krishnan, C. U. Kshirsagar, G. K. Ananthasuresh and B. Navakanta, ”Micromachined High-Resolution Accelerometers,” Journal of the Indian Institute of Science, vol. 87, no. 3, pp. 333-361, 2007.

[4] R. T. Li, S. R. Kling, M. J. Salata, S. A. Cupp, J. Sheehan, and J. E. Voos, ”Wearable Performance Devices in Sports Medicine,” Sports Health, vol. 8, no. 1, pp. 74-8, 2016. https://doi.org/10.1177/1941738115616917

[5] M. Skoczewski and H. Maekawa, ”Augmented Reality System for Accelerometer Equipped Mobile Devices,” in: 2010 IEEE/ACIS 9th International Conference on Computer and Information Science, Yamagata, Japan, pp. 209-214, 2010. https://doi.org/10.1109/ICIS.2010.140

[6] X. Qiu, Y. Bian, J. Liu, Y. Xiang, T. Ding, W. Zhu and F.-Z. Xuan, ”Ferroelectrets: Recent developments,” IET Nanodielectric, vol. 5, no. 3-4, pp. 113–124, 2022. https://doi.org/10.1049/nde2.12036
[7] J. Hillenbrand, M. Kodejska, Y. Garcin, H. V. Seggern and G. M. Sessler, ”High-sensitivity piezoelectret-film accelerometers,” IEEE Transactions on Dielectrics and Electrical Insulation, vol. 17, no. 4, pp. 1021-1027, 2010. https://doi.org/10.1109/TDEI.2010.5539670
[8] J. Hillenbrand, S. Haberzettl, T. Motz and G. M. Sessler, ”Electret accelerometers: Physics and dynamic characterization,” J. Acoust. Soc. Am., vol. 129, pp. 3682, 2011.
[9] J. F. Alves, F. S. I. Sousa, R. A. P. Altafim, L. P. R. De Oliveira, J. P. P. do Carmo and R. A. C. Altafim, ”An accelerometer based on thermoformed piezoelectrets with open-tubular channels,” in: Proc. Int. Conf. Dielectric Physics, pp. 524–526, 2020.
[10] I. N. Soares, R. A. C. Altafim, R. A. P. Altafim, J. P. P. do Carmo, C. Domingues and R. A. Flauzino, ”New Design for a Thermoformed Piezoelectret-based Accelerometer,” in: ALLSENSORS 2023, The Eighth International Conference on Advances in Sensors, Actuators, Metering and Sensing, pp. 21-24, 2023.
[11] R. A. P. Altafim et al., ”Template-based fluoroethylenepropylene piezoelectrets with tubular channels for transducer applications,” Journal of Applied Physics, vol. 106, no. 1, pp. 014106, 2009. https://doi.org/10.1063/1.3159039
[12] R. A. P. Altafim et al., ”Laminated tubular-channel ferroelectret systems from low-density polyethylene films and from fluoroethylene-propylene copolymer films - A comparison,” IEEE Transactions on Dielectrics and Electrical Insulation, vol. 19, no. 4, pp. 1116-1123, 2012. https://doi.org/10.1109/TDEI.2012.6259978
[13] X. Zhang, G. Cao, Z. Sun, and Z. Xia, ”Fabrication of fluoropolymer piezoelectrets by using rigid template: Structure and thermal stability,” Journal of Applied Physics, vol. 108, pp. 064113, 2010. https://doi.org/10.1063/1.3482011

Passive RFID Antenna Sensor Technology for Structural Behavior Monitoring

Dohyeong Kim, Sang-Hyeok Nam*, Mok Jeong Sim
Research Institute
ENGSOFT Co., Ltd.
Seoul, Republic of Korea
e-mail: dhkim.engsoft@gmail.com, shnam@engsoft.kr,
mjsim@engsoft.kr

Chunhee Cho
Civil and Environmental Engineering
University of Hawaii at Manoa
Honolulu, USA
e-mail: chunhee@hawaii.edu

Abstract— **This study introduces a novel approach for strain measurement by employing antenna sensors and Radio Frequency IDentification (RFID) readers. The functionality of passive antenna sensors is based on the alteration of resonant frequency due to structural deformation. Custom software was developed to manage RFID readers and collect data on the relationship between signal strength and frequency. The system was validated through experiments tensile strain of aluminum plates with antenna sensors and strain gauges. The antenna sensors showed an error of 5% compared to strain gauge measurements, which confirms the feasibility of using antenna sensors. Antenna sensor technology is anticipated to be utilized in various fields in the near future.**

Keywords-Antenna sensor; RFID; Resonant frequency; Strain Monitoring; Structural behavior.

I. INTRODUCTION

The construction industry is rapidly developing, and structural safety is a significant challenge in this field. Conventional wired measurement methods have limitations in sensor durability and require substantial installation and maintenance labor costs, making long-term and reliable monitoring difficult. This paper presents the result of our research on improving deformation measurement technology using passive Radio Frequency Identification (RFID) antenna sensors.

Recent advancements in Structural Health Monitoring (SHM) have led to the exploration of innovative sensing technologies, particularly passive RFID antenna sensors. These sensors offer real-time, wireless monitoring of structural behavior, providing engineers with valuable insights into infrastructure integrity. Wired methods for SHM are often hindered by sensor durability, complex installation, and high maintenance costs. Integrating the passive RFID antenna sensors into SHM systems represents a significant shift, overcoming many challenges of traditional sensor technologies. These sensors detect structural deformations via changes in resonant frequency, offering accurate measurements without direct physical contact. Additive manufacturing has improved sensor versatility by allowing for customizable shapes and materials to be used in various monitoring scenarios.

These systems offer the potential for real-time, wireless tracking and monitoring of physical, chemical, and mechanical properties, as well as environmental conditions [1]. Moreover, the advent of wireless and passive RFID technologies has ushered in a new era of intelligent strain monitoring systems for large-scale engineering structures [2].

However, despite the significant progress in this field, accurately detecting and characterizing defects based on passive antenna sensors in a remote distance poses special challenges due to the limited transmitting power and fading effect of Radio Frequency (RF) signals. Therefore, it is necessary to systematically study these challenges.

Passive RFID antenna sensors measure the deformation of structures by detecting the change of resonant frequency occurred by deformation [3][4]. Traditional antenna sensors are manufactured through chemical etching, which is time and cost ineffective. Therefore, we applied an additive manufacturing method through 3D printing and evaluated the performance by applying various materials to the elements of the antenna sensor [5]. Previous research on the measurement of structural deformation using passive RFID antenna sensors was addressed and validated at the laboratory scale. Therefore, there are still challenges to be overcome to commercialize the technology. In general, high-precision RFID testers have higher scanning resolution than commercial RFID readers. However, scanning with high-precision testers is time-consuming. In order to commercialize antenna sensor technology, measurement time must be reduced while measurement accuracy is increased.

The primary objective of our research is to commercialize strain measurement technology by using passive RFID sensors. In this paper, we introduce a developed methodology and software that derive accurate resonant frequencies from a smaller data set (signal strength versus frequency data) to achieve our main goal. Passive RFID antenna sensors were utilized in this research, which currently have maximum scanning distance of 2 meters and minimum measurement cycle time of 20 seconds.

Tensile testing of aluminum plates with antenna sensors and strain gauges attached was conducted, and the performance of the developed software and passive RFID antenna sensors was verified to determine accurate resonant frequencies. Further study is still required for improvement of passive RFID antenna sensor technology.

The paper is organized as follows. Section II provides a brief introduction to the components and operation of the passive RFID antenna sensor. Section III describes the

ISBN: 978-1-68558-164-0

additive manufacturing process for antenna sensors using 3D printers and various materials. Section IV explains the proper scan resolution to increase efficiency when measuring resonant frequencies using commercial RFID readers. Finally, Section V concludes our paper and proposes area of future work.

II. PASSIVE RFID ANTENNA SENSORS

A. *Methodology*

Passive RFID antenna sensors are organized with metallic ground plane (bottom), dielectric substrate (middle), microstrip patch antenna (top) and RFID chip. The antenna on the top surface is connected to the ground plane on the bottom surface through vias. The sensors are designed to operate using RFID in the Ultra High Frequency (UHF) range, specifically 868 ~ 956 MHz. The passive RFID antenna sensors are affixed to the structure (Figure 1(a)). As the structure deforms, the sensor deforms with it, causing a change in the sensor's resonant frequency that follows a negative linear relationship between strains and resonant frequencies. The relationship equation, (1), is obtained through linear regression. The first term coefficient, slope, represents the resonant frequency change characteristic of the sensor in response to deformation and is called the Sensor Factor (SF).

$$\varepsilon = \mathrm{SF}\cdot(f_r - f_{r,0}) \tag{1}$$

It is possible to calculate the strain, ε, of the structure at each stage of deformation by using the measured resonant frequency, f_r, at each stage, a known sensor factor and initial resonant frequency, $f_{r,0}$ (Figure 1(b)).

B. *Materials and Manufacturing*

Antenna sensors are typically produced using chemical etching. However, this method is inefficient to manufacture small quantities when developing sensors and testing different shapes. To overcome these limitations, we attempted additive manufacturing with 3D printers. The main components, including the antenna and dielectric, were manufactured using the following materials.

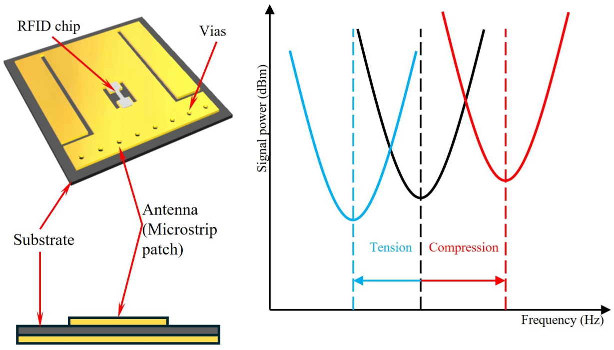

(a) (b)

Figure 1. Antenna sensor sensing: (a) Components of sensor; (b) Sensing mechanism.

1) *Materials for Components*

- Ground plane – aluminum foil, copper foil
- Substrate – PolyLactic Acid (PLA), Poly Carbonate (PC), PolyTetraFluoroEthylene (PTFE, Teflon)
- Antenna – silver nano ink, aluminum foil, copper foil, copper etching

2) *Manufacturing*

a) *3D printed substrates*

- Ground plane – glueing metallic (silver/copper) foil
- Substrate – 3D printing with PLA, PC
- Antenna – additive printing with silver nano ink or glueing metallic foils

b) *Nonprinted substrates*

- Ground plane – metallic (copper) coating
- Substrate –Teflon
- Antenna – additive printing with silver nano ink or copper etching

Figure 2 displays antenna sensors with substrates made of various materials and antennas created for performance testing. The various types of antenna sensors ware tested with the modified RFID reader for scanning antenna sensors based on commercial RFID reader (α213 from Apulsetech Inc.) using Impinj RFID chip, R2000, at a distance of 1 meter. The sensors with the 3D printed PLA substrate (Figure 2(a)-(d)) required high transmit power to respond to the RFID reader at a distance of 1 meter, making it difficult to determine their resonant frequency. This is likely due to the low melting point of the PLA substrate, which makes it challenging to solder the RFID chip during installation, resulting in incomplete adhesion between the RFID chip and antenna. However, sensors that used Teflon substrates showed satisfying performance and were compared to sensors with antennas made by silver nano ink and etching.

Figure 3 presents the test results of two antenna sensors Figure 2(e), (f). Those two sensors have a Teflon substrate and copper ground plane. However, the sensor in Figure 2(e)

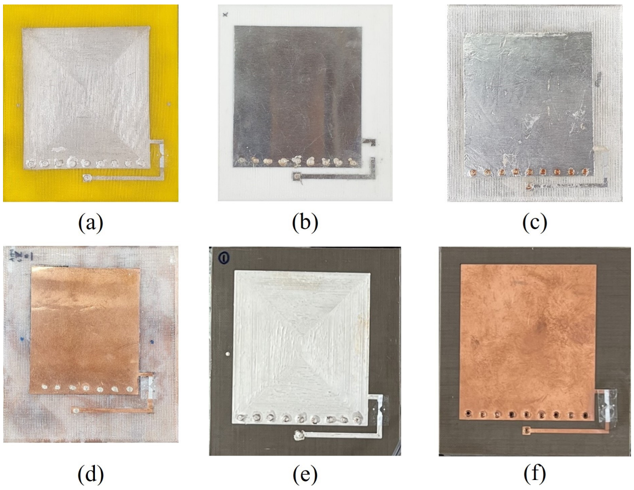

(a) (b) (c)

(d) (e) (f)

Figure 2. Different types of antenna sensors: (a) PLA+silver nano ink; (b) PLA+aluminum foil; (c) PC+aluminum foil; (d) PC+copper foil; (e) Teflon + silver nano ink; (f) Teflon +copper etching.

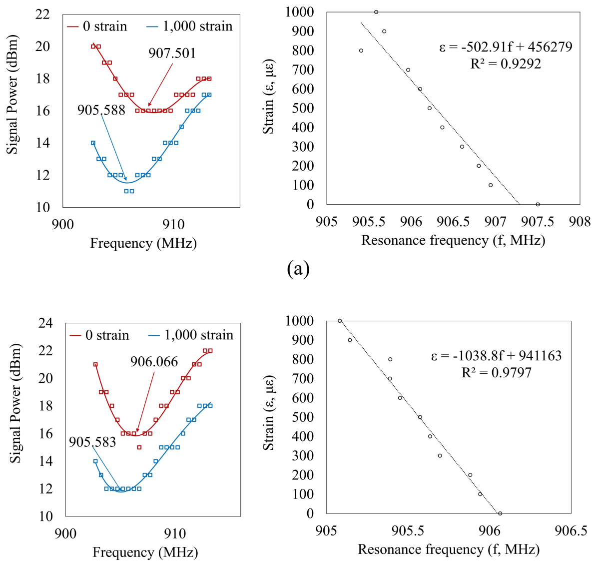

(a)

(b)

Figure 3. Antenna sensor : (a) Teflon+silver nano ink (printed); (b) Teflon+copper (etching).

had a printed silver ink antenna, while the sensor in Figure 2(f) had a chemically etched copper antenna. The two sensors were under tensile deformation from 0 to 1000 micro-strain (με), and their resonant frequencies were measured in each state. The left graph in Figure 3 displays the scanned data of frequency versus signal strength at strains of 0 and 1000 με and the resonant frequency. The right graph in Figure 3 shows the resonant frequency data for strains and the linear relationship with the equation. The resonant frequency-strain relationship equations were derived through linear regression of the measured data, resulting in coefficient of determination values, R^2, of 92.92% and 97.97%, respectively. These results indicate that sensors made by printing silver nano ink could be slightly inferior to those made by etching, but the measurement is accurate enough.

III. POWER-FREQUENCY SCANNING RESOLUTION

To enhance the accuracy of antenna sensors, it is crucial to determine the correct resonant frequency. By using a high-precision RFID tester (Tagformance Pro©), scanning could be performed by adjusting the signal strength and frequency to 0.1 dBm and 0.1 MHz, respectively. Based on a large specimen set, the resonant frequency could be predicted accurately. However, high-resolution scanning is unsuitable for field applications as it takes longer measurement time and is designed for laboratory use. A commercial RFID reader is more suitable for field applications, but the signal strength and frequency could not be precisely adjusted, as it is designed to scan the frequency band in use with a fixed (preset) signal strength and to search the corresponding RFID chip and exchange information. A commercial RFID reader has been modified to scan antenna sensors. However, there are limitations to the adjustable resolution of frequency and signal strength. To ensure efficient measurement, a trade-off between the accuracy of the resonant frequency and the resolution of the signal strength/frequency is necessary. We examined the measurement performance as a function of sample size (signal strength and frequency resolution).

Considering the performance of the modified RFID reader, the signal strength could be adjusted in 1.0 dBm increments, and the frequency could be adjusted in 0.1, 0.5, and 1.0 MHz increments. High-precision data of signal strength and frequency (raw data for strain rates 0, 100, 200, and 300) obtained from an RFID precision tester was prepared. The raw data was filtered to limit the number of specimens to simulate the situation of limited scanning resolution using the modified RFID reader (data set1: power step = 1.0 dBm, frequency step = 0.1 MHz; data set2: power step = 1.0 dBm, frequency step = 0.5 MHz; data set3: power step = 1.0 dBm, frequency step = 1.0 MHz). Figure 4 shows the results of deriving the signal strength-frequency curves and resonant frequency versus strain relationships for each data set. The coefficient of determination values, R^2, for the resonant frequency-strain relationship equations were 98.66% for the raw data, 96.17% for data set 1, 92.88% for

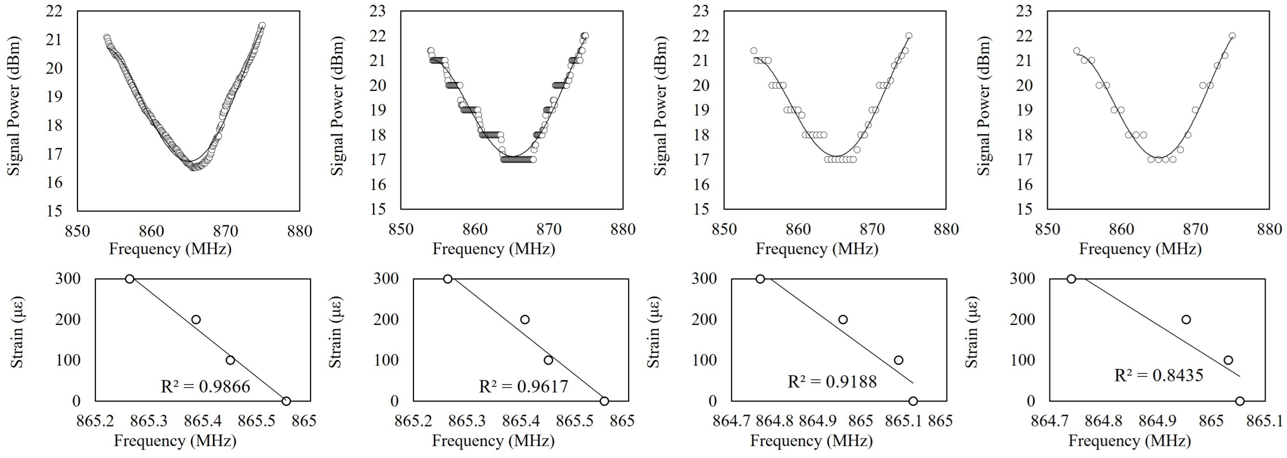

(a) (b) (c) (d)

Figure 4. Results based on scanning resolution: (a) raw data; (b) dataset 1; (c) dataset 2; (d) dataset 3.

data set 2, and 84.35% for data set 3. It could be concluded that a power step of 1dbm and a frequency resolution of at least 0.5MHz would result in an accuracy of over 90%. Additionally, scanning time can be reduced by decreasing the number of iterations for each scan.

The findings show the importance of balancing accuracy and operational efficiency. This insight is crucial for enhancing structural monitoring capabilities, thereby applying antenna sensors effectively in real structure.

IV. MEASURING AND MONITORING SOFTWARE

A. *Software Development*

To measure strain in a structure using an antenna sensor, these steps were followed: 1) After attaching antenna sensors to the structure, scan and save the initial resonant frequency; 2) When it is necessary to measure the strain of the structure, the antenna sensor is scanned to derive the resonance frequency value; 3) Calculate the structure's strain using the sensor factor and the rate of change of the resonant frequency considering the characteristics of the antenna sensor. The software was developed to measure strain through passive RFID antenna sensor and visualize behavior monitoring. The software has two main functions: 1) determining the sensor factor; and 2) measuring strain and monitoring time history. Figure 5 shows a screen that facilitates the two primary functions, and each function works as follows.

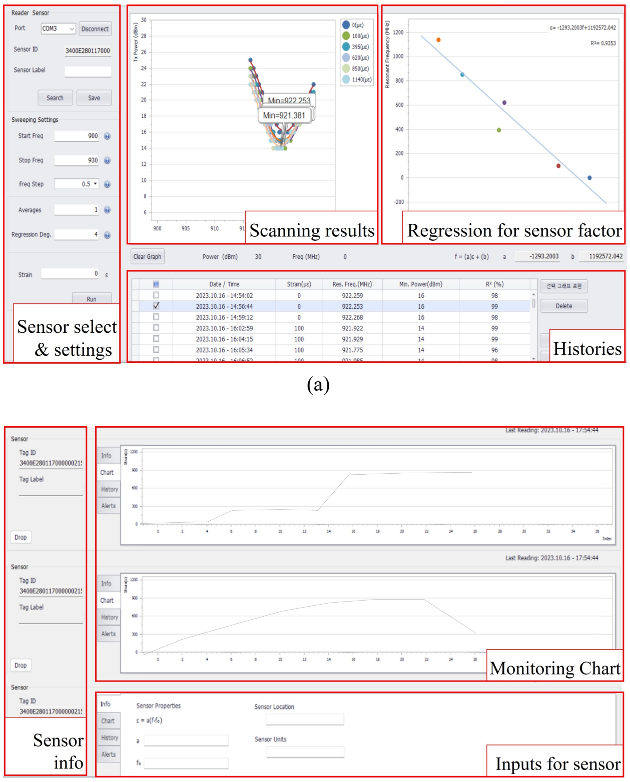

Port COM3

Sensor ID 3400E280117000

Sensor Label

Start Freq 900

Stop Freq 930

Freq Step 0.5

Averages 1

Regression Deg. 4

Strain 0 ε

Power (dBm) 30

Freq (MHz) 0

f = (a)ε + (b) a -1293.2003 b 1192572.042

☐	Date / Time	Strain(με)	Res. Freq.(MHz)	Min. Power(dBm)	R² (%)
☐	2023.10.16 - 14:54:02	0	922.259	16	98
☑	2023.10.16 - 14:56:44	0	922.253	16	99
☐	2023.10.16 - 14:59:12	0	922.268	16	98
☐	2023.10.16 - 16:02:59	100	921.922	14	99
☐	2023.10.16 - 16:04:15	100	921.929	14	99
☐	2023.10.16 - 16:05:34	100	921.775	14	96

(a)

Last Reading: 2023.10.16 - 17:54:44

Sensor

Tag ID 3400E28011700000021

Tag Label

Sensor Properties

$\varepsilon = a(f-f_0)$

a

f_0

Sensor Location

Sensor Units

(b)

Figure 5. Example screens of measuring and monitoring software: (a) Sensor factor determining, (b) Measuing and monitoring.

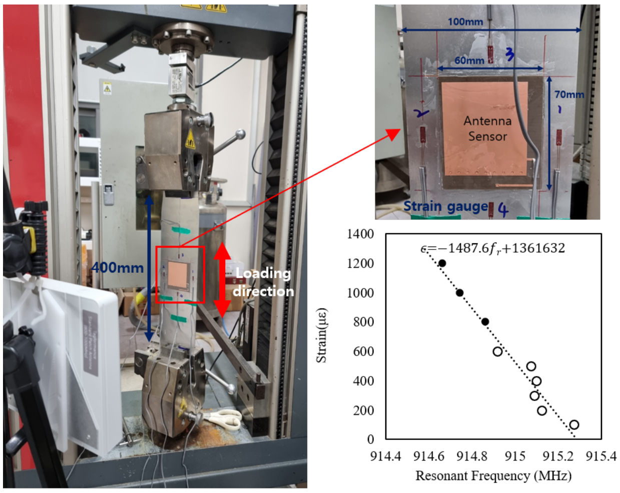

Figure 6. Tensile test setup and results.

1) *Determining Sensor Factor*

a) Install & Setup: Attach the passive RFID antenna sensor to the tensile specimen with a strain gauge.

b) Scan Each Stage: Scanning the sensor for each applied tensile strain to determine the corresponding resonant frequency.

c) Regression for Sensor Factor: Determine the sensor factor by liear regression analysis of the resonant frequency and strain dataset.

2) *Measuring and Monitoring*

a) Install: Attach the passive RFID antenna sensor to the required location of the structure.

b) Setup: Input the sensor factor to the software and scan to determine the initial resonant frequency, $f_{r,0}$.

c) Measure: Scan the sensor periodically or at any time to determine the resonant frequency, and calculate the strain.

d) Monitoring: Visualize historical strain in time series charts and send an alert when the strain exceeds the threshold.

The software enables efficient measurement and monitoring of deformations using the modified RFID readers in less time.

B. *Tensile Tests*

A specimen made of aluminum plate (100mmx400mm) was tested to evaluate the accuracy of passive antenna sensor strain measurement using the developed software.

The specimen attached with a passive RFID antenna sensor (60mmx70mm) and strain gauges was installed on the Universal Testing Machine (UTM) by gripping the top and bottom of the specimen. The antenna of the modified RFID reader is set up to scan the passive RFID antenna sensor at a distance of 1.5 meters. The modified RFID reader was controlled with monitoring software (Figure 6).

The passive RFID antenna sensor was used to scan and calculate the resonant frequency, and strain gauges were

ISBN: 978-1-68558-164-0

used to measure the strain in each state of the specimen under displacement-controlled tension.

The test was conducted in two phases. In phase 1, the sensor factor was obtained by measuring the strain from strain gauges and resonant frequency for each state of 0 to 600 με in increments of 100 με. In phase 2, a comparison was made between the strain measured from the antenna sensors and the strain gauge value of 800 με, 1,000 με, and 1,200 με. The results of the test are as follows: 1) The sensor factor is -1487.6, and 2) The average accuracy of strain was 97.85%. The results suggest that antenna sensors can be used for strain measurement, but their accuracy needs improvement before they can be applied in the field.

V. CONCLUSION AND FUTURE WORK

This study investigates the use of passive RFID antenna sensor technology for measuring deformation in structures. Antenna sensors were fabricated using additive manufacturing methods, such as 3D printing, from various materials, and it was concluded that the sensors printed with silver nano ink on the Teflon substrate were more cost-effective and efficient compared to traditional chemical-etched sensors.

Additionally, software was developed to measure strain rapidly using commercially available RFID readers. In tensile tests, comparisons with conventional strain gauges showed an error of less than 5%, validating its feasibility as a sensor. This development is expected to significantly reduce the time and effort required to monitor the health of structures. The study's findings would contribute to structural health monitoring not only in the construction industry but also in various fields.

Future research should focus on improving the measurement accuracy of antenna sensors, increasing the scanning distance, and deriving more effective structural health monitoring methods. This will require optimizing the materials and design of antenna sensors, validating their performance under different environmental conditions, and performing case studies on real structures. This will lay the foundation for the commercialization of the technology, ensuring the safety of structures, reducing maintenance costs, and contributing to a more sustainable development.

ACKNOWLEDGMENT

This work was supported by the ATC+(Advanced Technology Center Plus) Program (20014127, Development of a smart monitoring system integrating 3D printed battery-free antenna sensor technology with AI optimization) funded by the Ministry of Trade, Industry & Energy (MOTIE, Korea).

REFERENCES

[1] J. Zhang, G. Y. Tian, A. M. J. Marindra, A. I. Sunny, and A. B. Zhao, "A review of passive RFID tag antenna-based sensors and systems for structural health monitoring applications," Sensors, vol. 17, Jan. 2017, doi:10.3390/s17020265.

[2] G. Liu, Q. Wang, G. Jiao, P. Dang, G. Nie, Z. Liu, and J. Sun, "Review of wireless RFID strain sensing technology in structural health monitoring," Sensors, vol. 23, Jul. 2023, doi:10.3390/s23156925.

[3] C. Cho, X. Yi, D. Li, Y. Wang, and M. M. Tenstzeris, “Passive wireless frequency doubling antenna sensor for strain and crack sensing,” IEEE Sensors Journal, vol. 16, pp. 5725-5733, Jul. 2016, doi:10.1109/JSEN.2016.2567221.

[4] X. Yi, C. Cho, Y. Wang, and M. M. Tentzeris, “Battery-free slotted patch antenna sensor for wireless strain and crack monitoring,” Smart Structures and Systems, vol. 18, pp. 1217–1231, Dec. 2016, doi: 10.12989/SSS.2016.18.6.1217

[5] J. Dyogi, X. Song, S. Jang, S. Nam, and C. Cho, "3D Printing technique for passive wireless strain sensing," Engineering Proceedings, vol. 36, Aug. 2023, doi:10.3390/engproc2023036053.

Structural Behavior Monitoring System Using Scalable Carbon Nanotube Patch Sensors

Sang-Hyeok Nam, Dohyeong Kim, Giwan Jo
Research Institute
ENGSOFT Co., Ltd.
Seoul, Republic of Korea
e-mail: shnam@engsoft.kr, dhkim.engsoft@gmail.com,
gwjo@engsoft.kr

Seung-Hwan Jang
Department of Civil and Environmental Engineering
Hanyang University ERICA
Ansan, Gyeonggi-do, South Korea
e-mail: sj2527@hanyang.ac.kr

Abstract— **In this study, a scalable Carbon NanoTube (CNT) patch sensor-based system is introduced to monitor the abnormal behavior of bridge structures. The CNT sensor is a composite of carbon nanotubes and polyurethane, and it functions as a sensor that could detect the behavior of a structure using the electrical resistance change characteristics of the CNT. The size and shape of the scalable CNT patch sensor are adjustable depending on the type and surface condition of the structure, making the sensor attachable in locations where existing sensors, such as strain gauges, could not be installed. Therefore, the scalable CNT patch sensor could accurately detect abnormal behaviors occurring at any locations of the structure. The observed data is transmitted to the Internet of Things (IoT) based behavior detection and monitoring system for analysis, allowing us to proactively identify structural problems that may arise. The abnormal behavior monitoring system using scalable CNT patch sensors was field tested on a steel tied arch bridge in the United States. This confirms that the proposed system could effectively monitor the abnormal behavior of bridge structures and detect potential problems. It is expected that the structural abnormal behavior detection technology using scalable CNT patch sensors would be effectively utilized in various fields in the near future.**

Keywords- Carbon nanotube sensor; Scalable; Abnormal behavior detection; IoT sensing system; Monitoring system.

I. INTRODUCTION

Long-term monitoring of civil infrastructures, such as bridges, is essential for ensuring public safety and prolonging structural longevity. The conventional method of monitoring using strain gauges has limitations, such as small detecting area and low durability. Additionally, strain gauges could not be installed or attached to non-flat surfaces, such as layered or stepped surfaces. To overcome these limitations, sensors that use carbon nanomaterials, such as Carbon NanoTubes (CNTs), graphene and carbon fibers, are being continuously developed. The characteristics of carbon nanomaterial composites, such as electrical resistance and flexibility, depend on the type or concentration of carbon material and matrix used. These characteristics could be adjusted to meet specific measurement or installation requirements and were developed to overcome the limitations of strain gauges. The advancement of sensor technology, particularly utilizing carbon nanomaterials, not only addresses the limits of traditional strain gauges but also enhances structural monitoring capabilities in diverse environmental conditions and geometric complexities.

The strain sensor based on CNTs is designed for structural health monitoring applications. The sensor platform integrates carbon nanotubes that are known for their exceptional electrical properties to provide high sensitivity and reliability in detecting structural deformations [1].

In addition, scalable and multifunctional textile based on carbon nanotubes, which serves as distributed sensors for flow and cure monitoring not only demonstrates the versatility of carbon nanotube-based sensors but also highlights the potential applicability in various monitoring scenarios, including structural health monitoring [2].

The research for fabrication and characterization of CNT-based sensors for strain sensing applications provides valuable insights into the development of high-performance sensors capable of accurately detecting structural deformations, which are essential for ensuring the safety of civil infrastructure [3].

This research proposes a new approach to structural behavior monitoring using a composite of CNT as a patch sensor. The CNT patch sensor can be divided into small pieces from the original patch sensor, and this size-adjustable sensor is called scalable CNT patch sensor. Our methodology aims to overcome the limitations of conventional monitoring systems. Specifically, we have developed a scalable CNT patch sensor that could be adjusted to fit non-flat surfaces, including layered or stepped surfaces. We demonstrate the efficacy and practicality of our proposed monitoring system in real-world scenarios through empirical validation and field testing.

The paper is structured as follows: Section II presents the development and characteristics of CNT patch sensors. Section III outlines the implementation of a monitoring system utilizing Internet of Things (IoT) technologies. Section IV specifies the experimental procedures and findings regarding the performance evaluation of CNT patch sensors through tensile, bending, and field tests. Finally, in Section V, we present our conclusions and ideas for future work.

II. CARBON NANOTUBE-BASED SENSORS

This section introduces CNT patch and scalable CNT patch sensors utilized in structural monitoring technologies, which are both composites of CNTs and PolyUrethane (PU). The CNT patch sensors measure strain in a structure by detecting changes in resistance with deformation. The scalable CNT patch sensors aim to overcome the limitations of conventional strain gauges by providing flexibility and ease of installation. These sensors can be divided into small pieces and sized according to the attachment location and monitoring purpose.

A. CNT patch sensor

The CNT patch sensors are composed of a composite of CNTs and PU. The CNT/PU composite patch sensors are produced through a complex process, as illustrated in Figure 1. The most crucial process that affects the sensor quality is the dispersion of CNTs in the PU. Therefore, ultrasonication is used to disperse the CNTs in the PU [4][5]. The CNT patch sensor consists of the CNT/PU patch as a primary component and electrodes for wiring to the measurement device. The results of the resistance test of the CNT/PU patch indicate that the performance of the CNT patch is significantly improved with a 5 wt% CNT concentration (Figure 2). As such, using 5 wt% CNT patches is recommended for the CNT patch sensor.

The strain using a CNT patch sensor is measured by: 1) obtaining the sensitivity, S, of the specific type of CNT patch sensor through pretesting; 2) attaching the CNT patch sensors to the structure and measuring the initial resistance, R_0; 3) measuring the resistance at the required point in time to measure the deformation of the structure, R; 4) calculating the strain, ε, using (1).

$$\varepsilon = S\,(R - R_0)\,/\,R_0 = S\,\Delta R\,/\,R_0 \qquad (1)$$

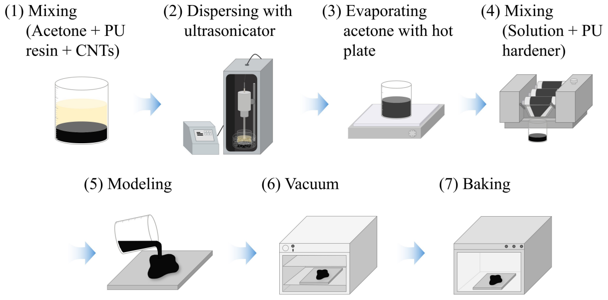

Figure 1. Fabrication of CNT patch sensors [5].

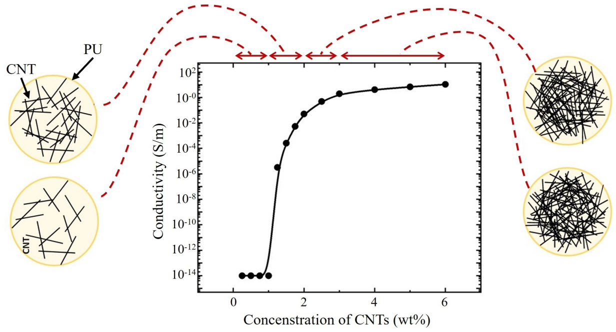

Figure 2. Degree of CNTs dispersion in polyurethane [5].

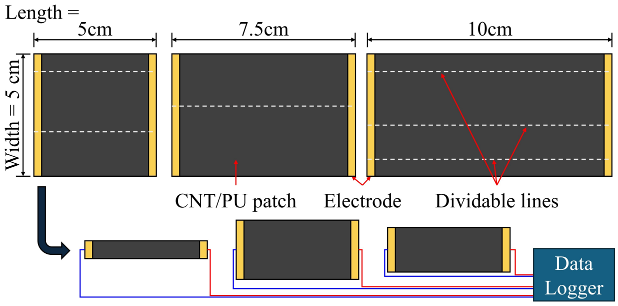

Figure 3. Shape and componants of CNT patch sensors.

B. Scalable CNT patch sensor

The aim of this research is to develop a flexible and scalable sensor that detects abnormal structural behavior, which makes it easier to install in places where conventional strain gauges are difficult to apply. Figure 3 shows examples of the geometries and components of a scalable CNT patch sensor. The sensor could be cut into multiple pieces lengthwise, with each piece having two electrodes on both ends depending on its installation location or purpose. Based on our previous study [5], the CNT patch sensor used 5 wt% CNT concentration.

The purpose of scalable CNT patch sensors is to detect any abnormal behavior in structures, such as the occurrence or development of cracks. To do so, the scalable CNT patch sensors are connected to a data logger to measure resistance. Abnormalities in the structure are detected through changes in electrical resistance trends, based on the collected time series of electrical resistance data.

III. MONITORING SYSTEM

Reliable and continuous measurement is necessary for long-term monitoring of a structure. IoT-based measurement technologies could increase maintenance and monitoring efficiency through wireless communication. The CNT patch sensor is incompatible with conventional data loggers due to its higher electrical resistance compared to typical strain gauges.

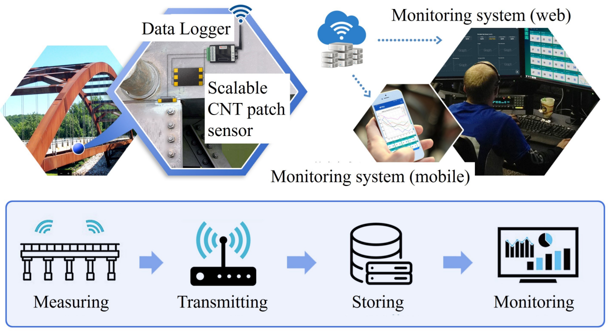

Figure 4. Overview of monitoring system using CNT patch sensors.

ISBN: 978-1-68558-164-0

(a) (b)

Figure 5. Data logger prototype: (a) Inside circuit, (b) External geometry.

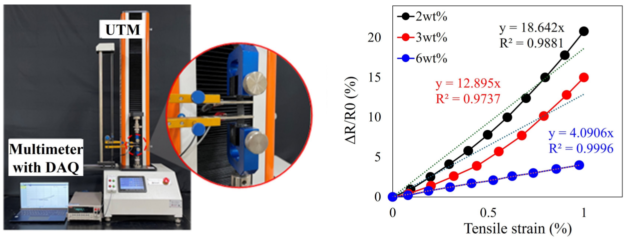

(a) (b)

Figure 7. Tensile test of CNT patch sensors: (a) Test settup, (b)strain vs. rate of resistance change ($\Delta R/R_0$).

A dedicated data logger has been developed to measure the resistance of CNT patch sensors, including a Wi-Fi module for data communication. Figure 4 shows an overview of monitoring system using CNT patch sensors.

A. Prototype Data Logger

The prototype data logger was designed to meet specific requirements, including measurable resistance up to 10 MΩ, up to 16 simultaneous channels, a sampling rate of 0.5 Hz for each channel, and the ability to transmit measured data to the server. It was able to receive commands from the server for control of the data logger and could be directly controlled by a touchscreen on the device. Figure 5 displays the data logger prototype. The data logger was created using a Printed Circuit Board (PCB) that includes a Wheatstone bridge to measure resistance for 16 channels. Additionally, an embedded MicroController Unit (MCU) was used for circuit control. The data logger also included a Raspberry Pi module for seamless wireless communication and connection to a touchscreen LCD display, as well as a 3.5 mm jack for sensor connectivity. Various features of the prototype were tested, and the results were evaluated using the LCD screen and jack. Despite the high-power consumption of the LCD screen and the susceptibility of the jack to noise generation, we chose them for their availability and ease of use.

The software on the device could measure the strains of 16 CNT patch sensors, including the input sensitivity of each sensor, and control the data logger to start and stop measurements.

B. Monitoring Software

Once the resistance of the CNT patch sensor is measured and the strain is calculated, the data is transmitted to the server and stored in the database. The monitoring software then visualizes the data stored on the server in various forms for the user and includes the function to remotely control the data logger. The monitoring software can display sensor data from 16 channels and can also be expanded. The measured resistance and the calculated strain for each channel are displayed, and strain data are also displayed as a time series graph. If the strain exceeds set value, an alarm notifying the event is triggered, and the data from 30 seconds before and after occurrence of the event are stored. Figure 6 shows the monitoring software display that visualizes the measurement results in data and graphs.

이벤트현황 05

CNT #01 14 07
CNT #02 22 13
CNT #03 28 11
CNT #04 05 21
CNT #05 37 11
CNT #06 03 06
CNT #07 19 45
CNT #08 40 12
CNT #09 23 14
CNT #10 10 21
CNT #11 02 06
CNT #12 52 34
CNT #13 27 33
CNT #14 36 14
CNT #15 18 05
CNT #16 40 11

Figure 6. Monitoring software prototype.

IV. EXPERIMENTAL SETUP AND RESULTS

A. Tensile Test of CNT Patch Sensor

The CNT patch sensors were mixed with 2, 3, and 6 wt% CNT concentration and dispersed in acetone using ultrasonic waves. The sensors were installed on a Universal Testing Machine (UTM), and both electrodes of a multimeter were connected (Figure 7(a)). The UTM applied displacement to the CNT patch sensor in tensile up to 1% strain, and the resistance of the sensor was measured at each stage of strain. The results are presented in Figure 7(b). The relationship between strain and resistance change rate became more linear as the CNT concentration increases. The sensor's sensitivity was determined by the slope of its linear regression curve. An excellent fit was indicated by the coefficient of determination, R^2, of the 6 wt% sensor, which was 99.96%. As the CNT concentration increased, the sensitivity decreased. However, the sensor with 6 wt% CNT has a higher sensitivity of 4.0 compared to the conventional strain gauge, which has a sensitivity of about 2.0.

B. Bending Test of CNT Patch Sensor

Tensile tests were conducted on the CNT patch to evaluate the stability and sensitivity of patch sensors containing 6 wt% CNTs. Subsequently, the sensors were attached to a scale model of a concrete bending test specimen to verify their sensitivity to cracks during bending tests. Figure 8(a) shows the results of a four-point bending test conducted until the test specimen cracked and failed. CNT patch sensors were attached to the lower part of the test specimen to monitor its response during cracking and evaluate the performance of abnormal behavior detection, as shown in Figure 8(b). The UTM data and test results of the CNT patch sensors are presented in Figures 8(d) and 8(e), respectively. The CNT patch sensors rapidly detected cracks by exhibiting a significant change in $\Delta R/R_0$ at approximately 550, 650, and 900 seconds after the test started. The CNT patch sensors, as shown in Figure 8(c), were able to detect cracks at 550 and 650 seconds that were not visible to the

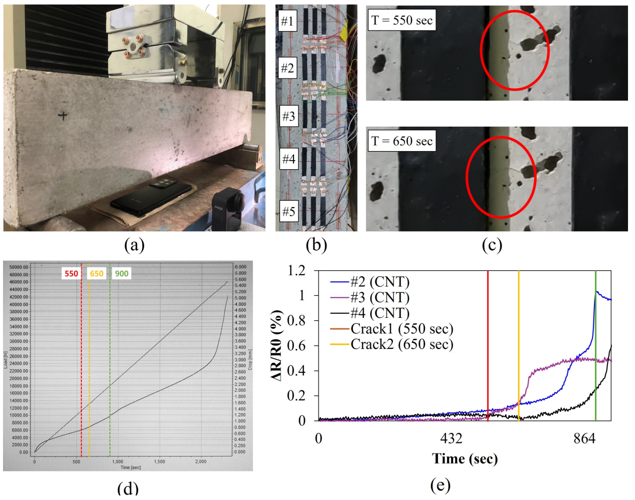

(a) (b) (c)

(d) (e)

Figure 8. Bending test for detecting cracks: (a) Test settup, (b) Bottom surface of test specimen, (c) Cracks detected time, (d) Time vs. load & disp.(UTM), (e) Time vs. $\Delta R/R_0$ (CNT patch sensors).

naked eye. Figure 8(d) presents the time-series data of load and displacement from UTM and each time of cracks, but it does not unambiguously indicate whether a crack has occurred. The test demonstrated that the CNT patch sensor developed is highly sensitive to strain, making it suitable for detecting cracks and structural abnormalities.

C. *Field Test on the Bridge*

The scalable CNT patch sensors were installed on a steel tied arch road bridge (main span 158m) in the US to assess their response during loading test. The scalable CNT patch sensors and strain gauges were installed on the joint of the floor beam and girder during the loading test for safety diagnosis of the bridge, as shown in Figure 9(a). The electrical response of the CNT patch sensor was monitored using the prototype data logger, and the electrical changes of the CNT patch sensor in response to load changes were used to detect abnormal behavior of the structure. Additionally, the response of the sensor on a mobile phone with LTE communication was also monitored, as shown in Figure 9(b).

The loading tests were performed using two 31,750 kgf (70,000 lbf) trucks travelling in one or two lanes at speeds of 16.1 km/h and 72.4 km/h (10 mph and 45 mph) to measure changes in bridge behavior. Table 1 shows the loading test schedule. The sampling rate of the data logger was set to 0.5 Hz.

Figure 10 displays the test results. The upper plot shows the change in resistance rate from the initial resistance, $\Delta R/R_0$, over time. The lower plot displays the change in resistance rate over time from the previous resistance. The CNT patch sensors detect changes in electrical resistance during the loading test. The test results indicate that scalable CNT patch sensors are versatile and can be used in narrow or wide areas, as well as on welds with height differences on both sides, due to their flexible and scalable characteristics. Tests #3 and #4 were expected to elicit greater $\Delta R/R_0$ since the trucks were travelling at 4.5 times the speed of tests #1 and #2. However, the responses of tests #3 and #4 were inaccurate, and this is assumed to be because the sampling rate of 0.5 Hz may not have been sufficient to capture resistance changes caused by a fast-moving truck. To monitor both short-term dynamics and long-term static behavior of the structure, the monitoring system should be updated to allow for sampling rate adjustments.

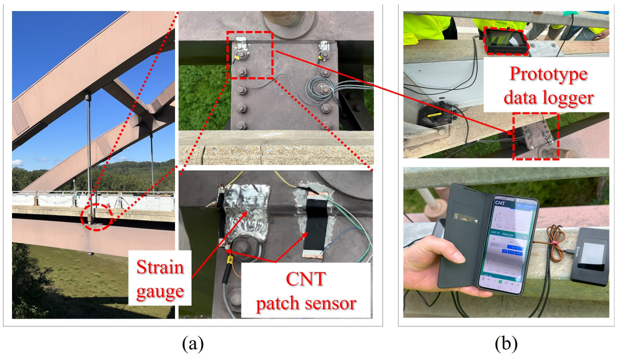

(a) (b)

Figure 9. Field test: (a) Installation of sensors, (b) Setup of data logger and monitoring software on mobile phone.

Table 1. Field Test Schedule

Test no.	**Test condition**		**Test no.**	**Test condition**	
	Lane	***Speed***		***Lane***	***Speed***
#1	Left	16.1 km/h (10 mph)	#3	Left	72.4 km/h (45 mph)
#2	Right		#4	Right	

V. CONCLUSION AND FUTURE WORK

This study presents a method for detecting abnormal behavior in structures using scalable CNT patch sensors. A review of prior research was conducted to understand the manufacturing and quality aspects of CNT/PU composite patch sensors. The authors found that the sensor with a 5 wt% CNT concentration exhibited the best performance and proposed a method for measuring the sensitivity of CNT patch sensors based on this finding.

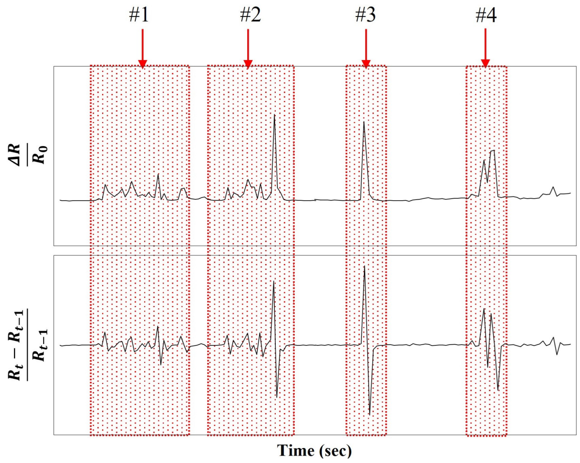

Figure 10. Field test results.

The study investigated the potential of scalable CNT patch sensors to detect abnormal behavior in structures, including superficial cracks and structural deformations. Experimental tests have demonstrated the effectiveness of these sensors in detecting such behaviors. The study demonstrates that the sensors are efficient in detecting abnormal behavior in structures. Additionally, field experimentation has confirmed the practicality of scalable CNT patch sensors. The CNT patch sensors installed on a road bridge accurately detected changes in load induced by vehicle movements.

The results of this study demonstrate the potential of CNT patch sensors as a useful tool for long-term structural health monitoring and maintenance. However, there are still challenges to be addressed before CNT patch sensors could be applied in the field, such as the development of mass production techniques for CNT patch sensors or the ability to adjust the system sampling rate for static and dynamic measurement purposes. We also plan to conduct research on sensors with integrated data loggers. Continued research is expected to address these challenges and contribute significantly to the development of safer and more efficient structural maintenance and monitoring systems in the future.

ACKNOWLEDGMENT

This work is supported by the Korea Agency for Infrastructure Technology Advancement (KAIA) grant funded by the Ministry of Land, Infrastructure and Transport (Grant RS-2023-00268377).

REFERENCES

[1] M. Han, J. Kim, Y. Choi, J. P. Yun, G. S. Lee, S. Kang, and D. Jung, “Carbon nanotube-based strain sensor for structural health monitoring.” Japanese Journal of Applied Physics, vol. 58, SDDJ07, 2019. doi:10.7567/1347-4065/ab12c2.

[2] H. Dai and E. T. Thostenson, “Scalable and multifunctional carbon nanotube-based textile as distributed sensors for flow and cure monitoring.” Carbon, vol. 164, 2020. doi:10.1016/j.carbon.2020.02.079.

[3] S. Ahmed, E. T. Thostenson, T. Schumacher, S. M. Doshi, and J. R. McConnell, “Integration of carbon nanotube sensing skins and carbon fiber composites for monitoring and structural repair of fatigue cracked metal structures.” Composite Structures, vol. 203, pp. 182-192, 2018. doi:10.1016/j.compstruct.2018.07.005.

[4] S. Jang, “Self-Sensing Carbon Nanotube Reinforced Composites for Smart Cities.” 5th International Conference on Smart Monitoring, Assessment and Rehabilitation of Civil Structures, August 2019.

[5] Y. Jung and S. Jang, “Crack detection of reinforced concrete structure using smart skin.” Nanomaterials, vol. 14, 632, April 2024. doi:10.3390/nano14070632.

CuBr@SiO₂ Mesoporous Composite for ppb Level Ammonia Detection in Humid Environment at Room Temperature

Weber Lisa, Martini Virginie, Bendahan Marc
Aix Marseille Univ.
CNRS, IM2NP, AMUTech
Marseille, France
e-mail: lisa.weber@im2np.fr
virginie.martini@im2np.fr
marc.bendahan@im2np.fr

Grosso David
Aix Marseille Univ.
CNRS, CINaM, AMUTech
Marseille, France
e-mail: david.grosso@univ-amu.fr

***Abstract*— The need for non-invasive methods to improve medical monitoring is growing and transdermal gas monitoring seems relevant. We aim to fabricate a gas sensor for ammonia transdermal detection as ammonia is a biomarker of chronic kidney disease. We previously showed that the synthesis of mesoporous SiO_2 thin film followed by CuBr impregnation led to a room-temperature selective ammonia sensor with very high sensitivity. Here, we show that the device detection limit and resolution are suitable for the detection of the very small quantities emitted from the skin. To evaluate the possibility of implementing this sensor in a skin-like environment, we also studied the effect of temperature and humidity on the sensing performances. Temperature has a small impact on the sensor baseline but a bigger impact on the sensor response. The humidity effect on the sensor response to ammonia is low below 30%. The effect is higher at 50% relative humidity and may be attributed to the film mesoporous structure. This paper shows that the sensing properties of the sensor make it a good candidate for transdermal ammonia detection.**

Keywords- mesoporous sensor; CuBr; ammonia.

I. INTRODUCTION

New devices for medical monitoring are being developed to improve both the medical monitoring of patients and our understanding of diseases. The detection of skin-emitted gas would allow both, by offering a non-invasive monitoring for the patient and access to new biomarkers for the medical practitioners. In this contribution we aim at developing an ammonia sensor to detect skin-emitted ammonia on patients suffering from chronic kidney disease as it is a potential biomarker of an acid load increase caused by this disease. Its use would complement the analyses carried out today, such as urine and blood tests that are invasive, costly, and are carried out too infrequently to provide proper monitoring of patients. To be used in this purpose, the developed sensor has to be extremely sensitive as the transdermal ammonia concentrations are estimated around 100 ppb [1], and selective to ammonia. In addition, the development of a room-temperature device would allow fabrication cost and energy consumption reduction.

Current technologies for ammonia detection include resistive gas sensors generally based on metal oxide sensitive layer [2]–[4]. Although the latter provide good sensitivity to ammonia, their lack of selectivity and their high working temperature make them unsuitable for our application. Room-temperature ammonia sensors exist in the literature and are generally made of composite materials using conductive polymers or graphene-based materials. However, very few studies report on the ammonia detection associating great selectivity, sensitivity and stability in a single sensor.

In a previous study, we showed that the fabrication of resistive sensor based on the impregnation of the ionic conductor CuBr in a mesoporous thin film led to a selective and very sensitive room-temperature ammonia sensor. The sensor has a basic structure composed of two layers on Si/SiO_2 substrate. The platinum interdigitated electrodes are deposited by rf sputtering. The sensitive layer is deposited by the simple and inexpensive dip-coating method, which is a significant advantage for the accessibility of the sensor. Here, we study the sensor performances in conditions closer to skin environment namely humidity and temperature variation. We evaluate the sensor detection limit and resolution as well as the effect of the temperature and humidity on the baseline and on the ammonia response. The paper is organized as follows. Section II describes the materials and methods used to fabricate and characterize the sensor. Section III presents the results obtained for the detection limit and the resolution in III. A, the effect of temperature in III. B and the effect of humidity in III. C. The acknowledgement and conclusion close the article.

II. MATERIALS AND METHODS

A. Sensitive layer

The sensor structure is made of a Si/SiO_2 substrate with 100 nm-thick interdigitated platinum electrodes. The mesoporous layer is deposited by dip-coating from a sol-gel solution with the following ratio: TEOS:F127:HCl:EtOH:H_2O 1:0.006:0.38:70:6. The ratio 0.06 between the silica precursor TEOS and the porous agent F127 is chosen to obtain a hexagonal porous network.

ISBN: 978-1-68558-164-0

The SiO_2 layer is cured at 450°C and impregnated in a 1wt% CuBr solution in acetonitrile and removed with the dip-coater at 1 mm/s. The thickness, porosity and homogeneity are evaluated with ellipsometry-porosimetry. The SiO_2 layer is 90nm thick and the whole mesoporous layer is impregnated homogeneously by CuBr.

To evaluate the contribution of SiO_2 and CuBr in the CuBr@SiO_2 sensitive layer, a mesoporous SiO_2 layer without CuBr impregnation is also used as a sensitive layer as well as a CuBr layer without SiO_2.

B. *Sensing performance evaluation*

The sensor performances are evaluated under ammonia in a microchamber connected to a gas generation system. The dilution system enables the generation of concentration down to 60 ppb of ammonia and humidity levels from 0% to 80%. The chamber outlet is connected to a Proceas-Indus analyzer to measure real-time ammonia concentration in the chamber. The test chamber is located in a thermoregulated chamber at 34°C (skin temperature). Sensor response R_g/R_a is calculated as the ratio between R_g the sensor resistance in ammonia and the R_a sensor resistance in air.

III. RESULTS AND DISCUSSION

A. *Limit of detection and resolution*

To evaluate the sensor limit of detection, we exposed two sensors fabricated in the same conditions to small NH_3 concentrations from 0 to 52 ppb. The ammonia concentration in the chamber is monitored by the gas analyzer and compared to the sensor resistances. The results related to the analyzer and to one of the sensors are reported in Figure 1.

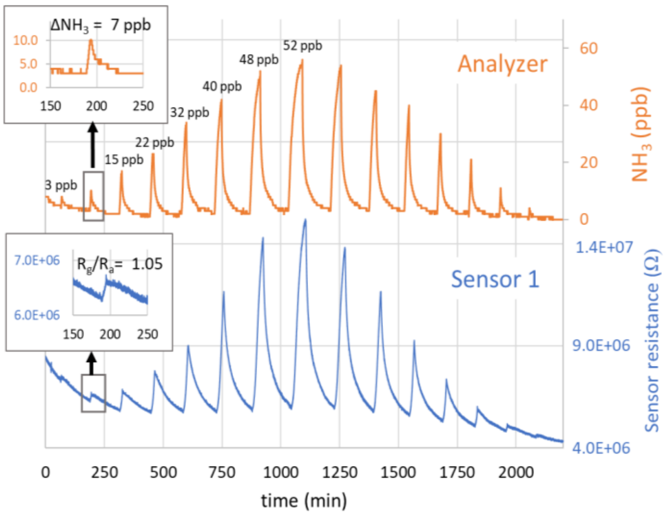

Figure 1. NH_3 concentration detected by the gas anayzer (orange) at 34°C with a flow rate of 500 sccm and the corresponding sensor resistance (blue). The inserts are magnification of the analyzer and sensor signals during the 7 ppb exposure.

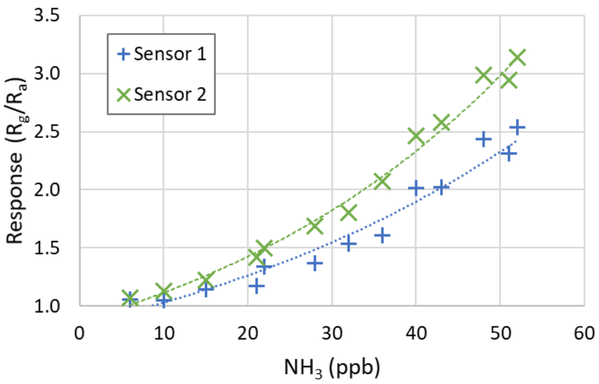

Figure 2. Calibration curves of CuBr@SiO_2 sensor exposed to NH_3 from 7 ppb to 53 ppb at 34°C.

The limit of detection is considered to be the smallest concentration to induce a sensor resistance variation superior to 3 times the background noise. In this case, such a variation is obtained for an ammonia variation of 7 ppb. The corresponding response is 1.05. As illustrated in Figure 2, where the sensor responses are reported, the two sensors show very similar behavior, proving the reliability of our results as well as the reproducibility of our process fabrication.

Resolution is assessed by exposing the sensor to 60 ppm NH_3 followed by 10 ppb steps up to 130 ppb. The analyzer and the sensor signal are overlaid in Figure 3. The resistance variation between two NH_3 concentration is calculated as the ratio between the maximum and the minimum resistances. The insets in Figure 3 show that a variation of 10 ppb NH_3 from 76 ppb to 86 ppb is detected by the sensor with a response of 1.1. This is in good accordance with the calibration curves presented above. The second sensor showed the same response to a variation of 10 ppb. Thus, we can affirm that CuBr@SiO_2 mesoporous sensors can detect small NH_3 concentrations as low as 7 ppb with a resolution of at least 10 ppb.

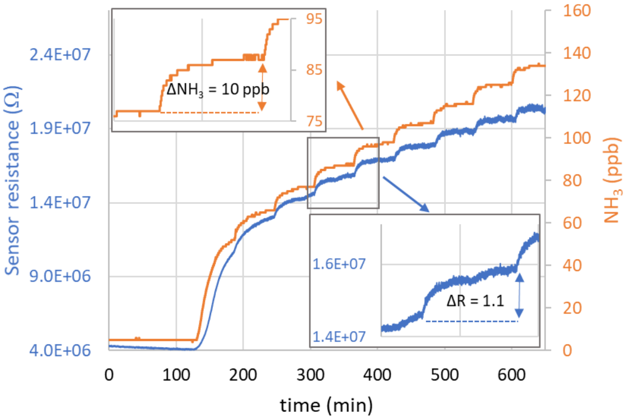

Figure 3. Gas analyzer signal (orange) and sensor resistance (blue) during CuBr@SiO_2 sensor exposure to increasing NH_3 concentration in 10 ppb steps for resolution evaluation.

ISBN: 978-1-68558-164-0

B. *Effect of temperature*

As the sensor operates without a heating system, the effect of environmental temperature on the sensing performances has to be studied. Here, we measured the baseline and the sensor response to short NH_3 exposures of 2 minutes at 20°C, 30°C and 40°C. The temperature, the ammonia concentration detected by the analyzer and the sensor resistance are reported in Figure 4. From these results, one can see that the baseline resistance decreases with temperature as well as the sensor response. For example, at 20°C the sensor response to the highest concentration tested is more than 10 times superior to the sensor response at 40°C.

The decrease of resistance under dry air with temperature is attributed to the mobility of charge increase favored by heat and it is in accordance with results reported in literature regarding the temperature dependence of CuBr conductivity from 30°C to 490°C [5]. The decrease of response with temperature is imputed to a temperature-induced shift in the adsorption/desorption equilibrium in favor of desorption. Although this temperature dependence could make it difficult to interpret the data in real-life conditions, it is necessary to assess its magnitude in order to take corrective action later on by adding a temperature sensor and artificial intelligence in the system.

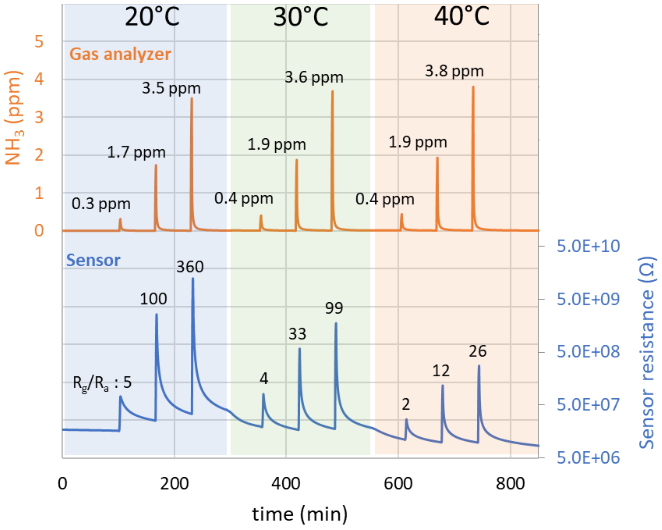

Figure 4. NH_3 concentration detected by the analyzer (orange) and corresponding CuBr@SiO_2 sensor resistance (blue) at 20°C, 30°C and 40°C.

C. *Effect of humidity*

The humidity effect on the sensing performances of CuBr@SiO_2 sensor is evaluated at 0%, 10%, 30% and 50% relative humidity. After baseline stabilization at each humidity, the sensor is exposed to 1 ppm ammonia. To evaluate the contribution of SiO_2 and CuBr, the sensors SiO_2 and CuBr are subjected to the same test conditions. The results are reported in Figure 5. Even though SiO_2 sensor presented an n-type response to NH_3, it is calculated as R_g/R_a to be consistent with the other sensors and to illustrate the SiO_2 contribution in a more visual way in Figure 5.

SiO_2 sensor is too resistive under dry air thus no baseline could be measured. The exposure to 1 ppm and 5 ppm NH_3 did not lead to a signal. Under humid condition SiO_2 resistance is measurable. The baseline decreases with humidity from 5.3×10^8 Ω at 10% to 1.5×10^8 Ω at 50%RH. The response of SiO_2 to ammonia is a characteristic to an n-type sensor as the resistance under ammonia decreases. This behavior is consistent with literature [6,7] and is attributed to the reaction between NH_3 and OH groups on the SiO_2 surface as SiO_2 is highly hydrophilic. However, SiO_2 sensor response to 1 ppm ammonia is low and constant for each humidity level.

CuBr sensor baseline increases with humidity. This increase is attributed to the adsorption of H_2O on CuBr as a reductive species, thus inducing a response similar to NH_3. The response of CuBr sensor to 1 ppm NH_3 increases with humidity. One could expect a decrease of the response due to a competition between H_2O and NH_3 acting both as reductive species. Here, the observed phenomenon is the opposite. Thus, we believe that the presence of H_2O on CuBr increases the NH_3 interactions on the layer.

CuBr@SiO_2 sensor behavior under humidity appears more complex. The baseline increases with humidity which is consistent with the affinity between H_2O and CuBr reported above.

The response is almost unaffected from 0 to 30%RH but undergoes a big drop at 50%RH. This sudden decrease might be related to the porous structure of the layer. While the pores are covered but not filled with water below 30%RH, the water pressure at 50%RH is high enough to fill completely the pores with water, thus preventing ammonia to interact with CuBr. This hypothesis is consistent with ellipsometry-porosimetry measurement where we observe a sudden increase of the adsorbed water at a certain water partial pressure, due to capillary condensation and in direct relation with pore size and geometry [8].

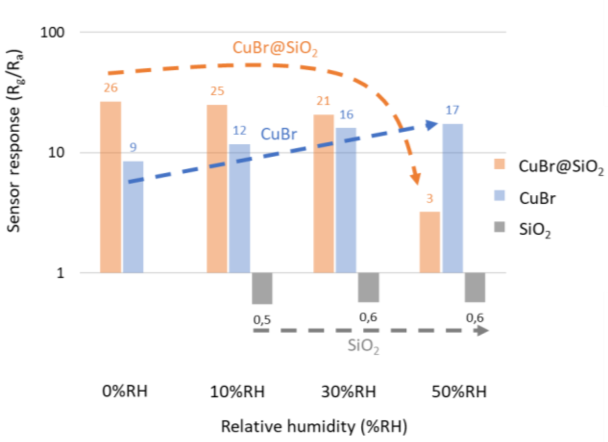

Figure 5. CuBr@SiO$_2$, CuBr and SiO$_2$ response to 1 ppm NH$_3$ under humid condition from 0 to 50% relative humidity.

The effect of humidity on SiO$_2$, CuBr and CuBr@SiO$_2$ showed that the SiO$_2$ contribution in ammonia detection is nil in dry conditions. Under humidity, its response to NH$_3$ is low and constant so its participation in NH$_3$ sensing is negligible. However, the mesoporous structure of SiO$_2$ can be responsible for a decrease of the sensor response at 50%RH. This effect of humidity could be addressed by adding a humidity filter when integrating the sensor into a device.

IV. CONCLUSION

Mesoporous CuBr@SiO$_2$ sensor exhibits sensing properties compatible with a potential use as transdermal ammonia sensor. The detection limit is experimentally determined at 7 ppb which is below the estimated ammonia concentration emitted from the skin. The sensor can detect minor fluctuations of NH$_3$ with a resolution of 10 ppb or less. The temperature increase leads to a sensitivity decrease attributed to the desorption of NH$_3$ favored by temperature. Humidity affects the baseline but the response to 1 ppm is only slightly affected up to 30%RH. The response decreases more significantly at 50%RH. This behavior might be the consequence of the mesoporous structure of SiO$_2$. The simple structure and ease of fabrication combined with good selectivity and very high sensitivity, make this sensor a good candidate for integration in a device for skin-emitted ammonia detection.

ACKNOWLEDGMENT

The authors are grateful to Soilihi Moindjie, for technical support.

REFERENCES

[1] S. Furukawa et al., “Simultaneous and multi-point measurement of ammonia emanating from human skin surface for the estimation of whole-body dermal emission rate”, Journal of Chromatography B, vol. 1053, pp. 60–64, 2017. doi.org/10.1016/j.jchromb.2017.03.034.

[2] Md. Shahabuddin et al., “Metal clusters activated SnO$_2$ thin film for low level detection of NH$_3$ gas”, Sensors and Actuators B: Chemical vol. 194, pp. 410–418, 2014. doi.org/10.1016/j.snb.2013.12.097.

[3] G. H. Mhlongo, D. E. Motaung, F. R. Cummings, H. C. Swart and S.S. Ray, “A highly responsive NH$_3$ sensor based on Pd-loaded ZnO nanoparticles prepared via a chemical precipitation approach”, Scientific Report 9, 2019. doi.org/10.1038/s41598-019-46247-z.

[4] C. M. Hung et al., “Facile synthesis of ultrafine rGO/WO$_3$ nanowire nanocomposites for highly sensitive toxic NH$_3$ gas sensors”, Materials Research Bulletin, vol. 125, 110810, 2020, doi.org/10.1016/j.materresbull.2020.110810.

[5] K. Singh, B. C. Yadav and V. K. Singh, “Electrical conductivity of cuprous bromide in the temperature range of 30-490 °C”, Indian J Chem, Vol. 51, pp. 1090-1094, 2012.

[6] S. Y. Wang et al., “Surface acoustic wave ammonia sensor based on ZnO/SiO$_2$ composite film”, Journal of Hazardous Materials, vol. 285, pp. 368-374, 2015.

[7] Y. Tang et al., “NH$_3$ sensing property and mechanisms of quartz surface acoustic wave sensors deposited with SiO$_2$, TiO$_2$, and SiO$_2$-TiO$_2$ composite films”, vol. 254, pp. 1165-1173, 2018, doi.org/10.1016/j.snb.2017.07.195.

[8] J. Loizillon, “Development of ellipsometry porosimetry for the characterization of nanoporous thin films applied to photovoltaics”, Doctoral thesis, Aix-Marseille, 2019, theses.fr/2019AIXM0308.